Charge Transport in Single Molecules

by

Yueqi Li

A Dissertation Presented in Partial Fulfillment
of the Requirements for the Degree
Doctor of Philosophy

Approved April 2017 by the
Graduate Supervisory Committee:

Nongjian Tao, Chair
Daniel Buttry
Vladimiro Mujica

ARIZONA STATE UNIVERSITY

May 2016

ABSTRACT

Studying charge transport through single molecules is of great importance for unravelling charge transport mechanisms, investigating fundamentals of chemistry, and developing functional building blocks in molecular electronics.

First, a study of the thermoelectric effect in single DNA molecules is reported. By varying the molecular length and sequence, the charge transport in DNA was tuned to either a hopping- or tunneling-dominated regimes. In the hopping regime, the thermoelectric effect is small and insensitive to the molecular length. Meanwhile, in the tunneling regime, the thermoelectric effect is large and sensitive to the length. These findings indicate that by varying its sequence and length, the thermoelectric effect in DNA can be controlled. The experimental results are then described in terms of hopping and tunneling charge transport models.

Then, I showed that the electron transfer reaction of a single ferrocene molecule can be controlled with a mechanical force. I monitor the redox state of the molecule from its characteristic conductance, detect the switching events of the molecule from reduced to oxidized states with the force, and determine a negative shift of ~34 mV in the redox potential under force. The theoretical modeling is in good agreement with the observations, and reveals the role of the coupling between the electronic states and structure of the molecule.

Finally, conclusions and perspectives were discussed to point out the implications of the above works and future studies that can be performed based on the findings.

ACKNOWLEDGMENTS

There have been many people who helped me greatly during my PhD study, and I would like to express my sincere gratitude to them. First, I would like to thank my advisor, Professor Nongjian Tao for his patience, support, motivation and immense knowledge. It was him who offered me the summer internship opportunity and encouraged me to do PhD in his lab. It was also him who continuously mentoring and inspiring me to solve research problems during the whole 5 year's journey. He is not only my advisor, but also a friend of mine. I would also like to express my thanks to the rest of my committee, Professor Daniel Buttry and Professor Vladimiro Mujica, for their valuable time and insightful comments.

I would like to thank Professor Erica Forzani for guiding me to have a first taste of doing research and then fall in love with it during my undergraduate summer internship. Also, I have learned a great deal from Dr Shaoyin Guo on thermoelectric measurement, circuit trouble shooting and labview coding, and from Dr Limin Xiang on DNA measurement and electrochemical measurement.

My thank also goes to my collaborators, Professor Yoshihiro Asai, Professor Michelle Coote, Professor David Beratan, Dr Simone Ciampi, Dr Naomi Haworth and Dr Chaoren Liu. This thesis wouldn't be possible without their great work.

I would also like to express my gratefulness to all my friends and colleagues in Dr Tao's lab for their informative discussions and feedbacks. I'd like to explicitly thank Dr

Ismael Diez-Perez, Dr Joshua Hihath, Dr Chris Bruot, Dr Thomas Hines, Dr Raphael Rosch, Dr Julio Palma, Mr Ali Rostamian, and Ms Yue Deng.

Last but not least, I would like to thank my family; my parents for their nurturing, love, and always being supportive on my education, my husband for his never-ending love, encouragement, and understanding, and my son for coming into my life and sharing this joyful journey with me.

TABLE OF CONTENTS

Page

LIST OF TABLES viii

LIST OF FIGURES ix

CHAPTER

1 INTRODUCTION 1

1.1 Introduction of Molecular Electronics 1

1.2 Charge Transport Theory of Single Molecule Junctions 3

1.2.1 Landauer Formula 3

1.2.2 Coherent Non-resonant Tunneling and Superexchange Model 7

1.2.3 Thermally Activated Incoherent Hopping 10

1.3 Scanning Tunneling Microscopy (STM) Break Junction Technique 12

1.4 Thermoelectric Effects in Molecular Junctions 15

1.5 Charge Transport/Transfer in DNA 21

1.6 Single Molecule Electrochemical Measurement 25

1.7 Molecular Mechanochemistry Done by STM Break Junction Measurements 28

2 THERMOELECTRIC EFFECT AND ITS DEPENDENCE ON MOLECULAR LENGTH AND SEQUENCE IN SINGLE DNA MOLECULES 32

2.1 Introduction 32

CHAPTER Page

2.2 Methods 33

2.2.1 Preparation of dsDNA SAM 33

2.2.2 STM Setup 34

2.2.3 Measurement of Thermoelectricity 34

2.3 Double Stranded DNA Sequences 35

2.4 Length Dependence of Conductance 38

2.5 Thermoelectric Effect in Single DNA Molecules 46

2.6 Theoretical Analysis 53

2.7 Other Supporting Data and Discussions 60

2.7.1 Gel Electrophoretic Characterization of dsDNA 60

2.7.2 Circular Dichroism (CD) Measurements 62

2.7.3 Melting Temperature 63

2.7.4 Conductance Histograms of dsDNA Measured in 20% Humidified Air 65

2.7.5 Conductance Histograms of ds DNA in 5 mM Phosphate Buffer 66

2.7.6 Molecular Length Dependence of DNA Resistance 66

2.7.7 Derivations of Eq. 2.4 and Discussion of Validity of the Assumption 69

2.7.8 Tight Binding Theory of DNA Thermoelectricity 71

2.8 Conclusions 74

CHAPTER Page

3. FORCE-INDUCED ELECTRON TRANSFER REACTIONS AND CONDUCTANCE SWITCHING IN SINGLE MOLECULES 76

3.1 Introduction 76

3.2 Methods 79

3.2.1 Preparation of Ferrocene SAM, Control Molecule SAM, and Ferrocene Dicarboxylic Acid SAM 79

3.2.2 Cyclic Voltammetry 80

3.2.3 STM Setup 82

3.2.4 STM Break Junction Measurement 82

3.2.5 Sweeps of STM Gate Voltage 83

3.3 Electrochemical Potential Sweep on Single Molecular Junctions 83

3.4 Mechanical Force-induced Redox Reactions 85

3.5 Theoretical Analysis 97

3.6 Other Supporting Data and Discussions 102

3.6.1 The Discrete Levels of Conductance at Different Gate Potential 102

3.6.2 Conductance Measurement of 1,1'-Ferrocenyl Diester Measured at -121 mV 103

3.6.3 Conductance at Different Stretching Distance for All Curves at Overpotential of +30 mV 104

CHAPTER Page

3.6.4 Relationship Between Conductance Peak Area and Surface Coverage of Redox Species. 105

3.6.5 Theoretical Description of the Stretching Process 106

3.7 Conclusions 109

CONCLUSIONS AND PERSPECTIVES 110

REFERENCES 113

LIST OF TABLES

Table Page

2.1 Sequences of dsDNA Studied in This Work..... 37

2.2 Conductance and Seebeck Coefficients of DNA With Different Sequences 45

2.3 The Resistance (R_t) and the Seebeck Coefficients (S_t) of the AT Blocks. 58

3.1 Measured Redox Potential and Applied Overpotential for Each Experiment 83

3.2 Spring Constants and Shifts in Gibbs Free Energy Calculated from the Vibrational Frequencies of Dimethyl Ferrocene Obtained by IR Spectroscopy and DFT Calculations, Using Reduced Mass Values Obtained from DFT Calculation…… 101

LIST OF FIGURES

Figure Page

1.1 Molecule Bridged in Between Two Metal Electrodes. 4

1.2 Energy Diagram Representation of Coherent Tunneling Charge Transport Mechanism. 9

1.3 Energy Diagram Representation of Thermally Activated Incoherent Hopping Charge Transport Mechanism. 12

1.4 Measurement of Single Molecule Conductance With STM Break Junction Technique. 14

1.5 Energy Diagram of Thermoelectric Effect in Molecular Junctions with (a) LOMO Transport and (b) HOMO Transport. 17

1.6 Illustrations of Different Methods of Thermoelectric Measurement 21

1.7 Illustrations of Different Methods of Charge Transfer/Transport through DNA 24

1.8 Illustration of the Electrochemical STM Measurement Set up. 26

1.9 Measurement of the Breakdown Force of Molecular Junction with AFM 31

2.1 Thermoelectric and Conductance Measurements of DNA. 39

2.2 Step-length Histograms of $A(CG)_3T$ Measured (a) in the Air and (b) in Solution. 41

2.3 DNA Resistance vs. Molecular Length for (a) $A(CG)_nT$ (n=3~7) (b) $ACGC(AT)_mGCGT$ (m=0~4) and $ACGC(AT)_{m-1}AGCGT$ (m=1~3) Sequences, and (c) the AT Blocks ($(AT)_m$ and $(AT)_{m-1}A$) in $ACGC(AT)_mGCGT$ and $ACGC(AT)_{m-1}AGCGT$ sequences. 44

Figure Page

2.4 Thermoelectric Measurement of DNA. 48

2.5 Thermal Voltage Histograms for Double Helical DNA Collected at Different Temperature Gradients..... 50

2.6 Linear Fitting of the Thermoelectric Voltage Data at Different Temperature Gradients for $A(CG)_nT$ (n=3~7), $ACGC(AT)_mGCGT$ (m=1~4), and $ACGC(AT)_{m-1}AGCGT$ (m=1~3) Sequences..... 51

2.7 Seebeck Coefficients of DNA with Different Molecular Lengths and Sequences.... 53

2.8 Thermoelectric Effect in DNA in Terms of Tunneling and Hopping Models..... 57

2.9 Gel Electrophoresis of DsDNA Samples after a Programed Annealing Process. 61

2.10 Circular Dichroism Data of (a) $A(CG)_nT$ (n=3~5), (b) $ACGC(AT)_mGCGT$ (m=1~3), (c) $A(CG)_nT$ (n=6,7), (d) $ACGC(AT)_{m-1}AGCGT$ (m=1~3) and $ACGC(AT)_mGCGT$ (m=4). 63

2.11 Melting Temperature Absorption Curve for $A(CG)_3T$ (Black Curve), and Two-State Thermodynamic Model Fitting (Red Curve). 64

2.12 Conductance Histograms of DsDNA Measured in Humidified Air. 65

2.13 Conductance Histograms of DsDNA Measured in Solution.. 66

2.14 Linear and Semi-Logarithmic Plots of Resistance vs. Length of Different DNA Sequences..... 68

2.15 The Su-Schrieffer-Heeger Model of DsDNA, Where ε_i and M_i are the Site Energy and Mass, Respectively, tij is the Transfer Integral, λij Describes the Electron-Phonon Coupling, and k_{ij} is Force Field Constant. 73

Figure Page

2.16 Seebeck Coefficient and Its Dependence on DNA Sequence and Length..... 74

3.1 Structure and Electrochemical Study of 1,1'-Ferrocenyl Diester. 78

3.2 Cyclic Voltammetry Study of 1,1'-Ferroceny Diester SAM on Au Substrate. 81

3.3 Stretching and Measurement of 1,1'-Ferrocenyl Diester under Different Gate Voltages. 88

3.4 Plateau Length Statistics of Conductance Decay Curves of Fc-Lip at Overpotential of (a) -122mV, (b) -7 mV and (c) +78 mV. 89

3.5 Structure and Electrochemical Calibration of 1,4-Phenylene bis(5-(1,2-dithiolan-3-yl)pentanoate) (Lip-ctr)..... 90

3.6 Conductance(Plateau Part) at Different Stretching Distance for Switched Curves at E-Eox/red = +30 mV.. 92

3.7 Logarithm Ratio of the Peak Area of Oxidized and Reduced Conductance Peaks Changing with Distance at Different Overpotential. 93

3.8 Logarithm Ratio of the Peak Area of Oxidized and Reduced Conductance Peaks at Different Potential When the Stretching Distance is 0 to 0.1 nm(Unstreched, Black Dots), and 0.3 to 0.4 nm(Stretched, Red Dots).. 96

3.9 Theoretical Model and Computational Results..... 100

3.10 Structure and Electrochemical Calibration of Ferrocene Dicarboxylic Acid. 103

3.11 Conductance Measurement of 1,1'-Ferrocenyl Diester Measured at Overpotential of -121 mV.. 103

Figure Page

3.12 Conductance at Different Stretching Distance for All Curves at Overpotential of +30 mV. (a) The Conductance V.S. Stretching Distance 2D Histograms of All Curves (Normalized at Each Distance). 104

3.13 Potential Energy Surfaces for Stretching between Atoms S1 and S2 in the Reduced(Blue) and Oxidised(Red) Species. 107

3.14 Changes in Significant Structural Parameters of the Reduced and Oxidized Species as the S1-S2 Distance is Increased..... 109

1 INTRODUCTION

1.1 Introduction of Molecular Electronics

Molecular electronics is an idea of building circuits using molecular functional blocks. This concept originated from a seminal paper published in 1974 by Aviram and Ratner, in which they proposed a single molecule rectifier-like device[1]. Since that time, the field has grown rapidly with the development of experimental techniques which allow investigation of charge transport properties through molecular junctions, such as mechanically controlled break junction (MCBJ)[2-4], cross-wire junction[5-7], mercury drop junction[8-10], scanning tunneling microscopy (STM) break junction[11-13], and conducting probe atomic force microscopy (CP-AFM)[14-16]. With the help of advanced organic synthesis skills, a number of linker groups have been approved to effectively form metal-molecule-metal junctions, including thiol[17], amine[18], carboxyl[18], pyridine[11], etc. Spanning solid state physics, organic chemistry, biophysical engineering and material science, molecular electronics rises as a highly interdisciplinary area.

Admittedly, molecular electronics is a burgeoning field that is far from well developed, since the agreement between theory and experiment for the conductance value of most systems hasn't been reached yet, the accurate conductance values of quite a number of molecules are still under debate, charge transport mechanisms in more complicated molecular systems are beyond our understanding. Clearly, a lot of work needs to be done to lead the techniques and measurements to its real practical

applications. However, apart from these short comings, molecular electronics is considered as one of the most promising alternatives to complementary metal-oxide-semiconductor (CMOS) technology to extend Moore's law beyond its foreseen limit. Extensive studies have been devoted into the invention of molecular building blocks analogous to conventional CMOS functional units, such as molecular diode[19-21], switches[22-24], transistor[25-27]. In addition, molecules can be designed to have novel functionalities other than those seen in conventional electronics, for example, thermoelectricity[28-30] and mechanically gated electronic properties[31, 32].

Meanwhile, the capability to determine the electronic properties of single molecules enables molecular electronics to be a powerful tool for exploring charge transport mechanisms in different aspects such as current-voltage (I-V) characteristics, length dependence, temperature dependence and electrochemical gate dependence of conductance. New charge transport mechanisms have been continuously discovered and understood in recent years. Besides fundamental investigations on how a single molecule behaves in a junction, molecular electronics can also help characterize charge transport properties in biological systems such as DNA[33-37], RNA[38, 39] and proteins[40, 41], making a significant impact on molecular biology and bioengineering. Moreover, it becomes possible to study different types of chemical reactions at single molecule level. An exciting example is force induced redox reaction observed in single Ferrocene molecules, which belongs to the realm of mechanochemistry.

This thesis will focus on how the charge transport through single molecular junctions responds with influences of temperature gradient and mechanical force. First, a brief

introduction of the important concepts of molecular electronics and the background of related measurements will be given. Next, an investigation into thermoelectric effect in single DNA molecules will be described. The following section will look into the force induced electron transfer reaction and conductance switching in single molecules. Finally, concluding remarks will be made about the work presented in this thesis, and limitations, prospective, and future directions will be discussed.

1.2 Charge Transport Theory of Single Molecule Junctions

As mentioned above, exploring charge transport mechanisms in single molecular junctions is one of the most fundamental goals of molecular electronics. In this section, we will start from introducing the very basic Landauer formula[42, 43], then proceed to two widely accepted charge transport models, coherent non-resonant tunneling[44-46] and incoherent hopping[47-49].

1.2.1 Landauer formula

The conventional Ohm's law can no longer hold for small dimension systems, where the quantum effect takes place. In turn, the charge transport process can be treated as a transmission process, and described by the Landauer formula[42, 43].

In an ideal one-dimensional situation where a molecule is bridged in between two electrodes (Fig. 1.1), the net current going from the left electrode to the right electrode is given by

$$I_{L\to R} = e\int v_g(k)\tau(k)\, f_L(E(k),\mu_L)\, n(k)dk \quad (1.2.1)$$

, where e is the electron charge, v_g is the group velocity of electrons in the leads, $\tau(k)$ is the transmission probability for the electrons through the barrier, f_L is the Fermi-Dirac distribution for electrode L with chemical potential μ_L, n(k)dk is the density of states.

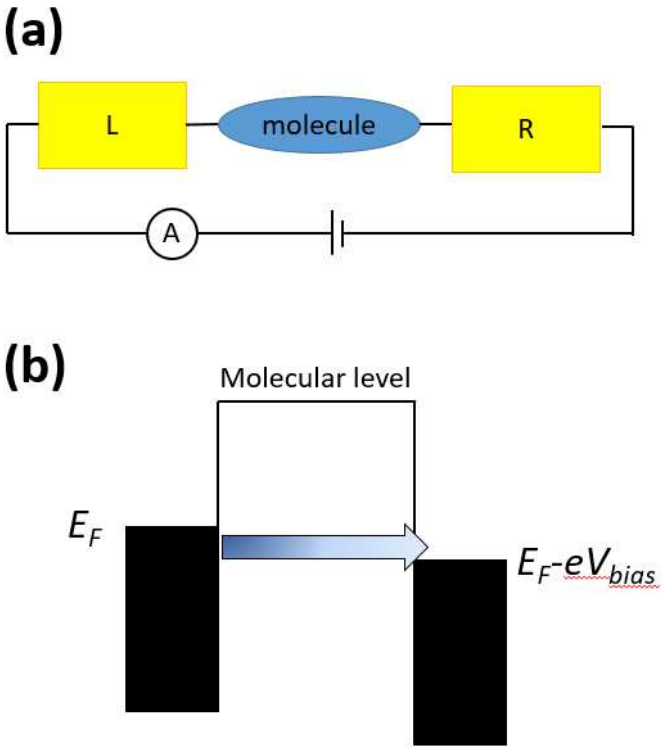


Figure 1.1 Molecule bridged in between two metal electrodes. (a) Schematic representation of a metal-molecule-metal junction. L and R stands for left and right

electrodes, a bias is applied across the junction and the current is monitored. (b) Energy diagram of the molecular junction as a square barrier.

The density of states between *k* and *k*+*dk* can be described in terms of the length of the junction L, as

$$n(k)dk = \frac{2}{L}\frac{L}{2\pi}dk \quad (1.2.2).$$

The electron group velocity is given by

$$v_g(k) = \frac{2\pi}{h}\frac{dE}{dk} \quad (1.2.3)$$

, where *h* is Plank constant and E is energy.

Thus, equation (1.2.1) can be written as

$$I_{L\to R} = \frac{2e}{h}\int \tau(E)\, f_L(E,\mu_L)\, dE \quad (1.2.4).$$

Similarly, the net current from the right to the left electrode is given by

$$I_{R\to L} = \frac{2e}{h}\int \tau(E)\, f_R(E,\mu_R)\, dE \quad (1.2.5).$$

Therefore, the total current through the above one-dimensional system can be described as

$$I_{total} = I_{L\to R} - I_{R\to L} = \frac{2e}{h}\int \tau(E)\, [f_L(E,\mu_L) - f_R(E,\mu_R)]\, dE \quad (1.2.6).$$

Assuming that Fermi energy is well above k_BT, so that the Fermi-Dirac distribution can be approximated as a step-function with 1 below E_F and 0 above. And assuming small bias voltage applied across the junction, one have

$$I_{total} = \frac{2e^2}{h}\tau(E)(\mu_L - \mu_R) \quad (1.2.7).$$

Finally, dividing by the bias voltage gives the Landauer formular describing the conductance

$$\mathrm{g} = \frac{2e^2}{h}\tau(E) \quad (1.2.8).$$

In equation (1.2.8), $\frac{2e^2}{h}$ is called the conductance quantum, and normally denoted as G_0, with a value of 77.4 nS or inversely 12.9kΩ. It is the conductance of a gold quantum point contact.

In real molecular junction systems, there are multiple modes resulting in multiple transmission channels, the transmission probability is the sum of all transmission channels through the junction, thus the complete representation of Landauer formula should be written as

$$\mathrm{g} = \frac{2e^2}{h}\sum_{i,j}\tau_{ij}(E) \quad (1.2.9)$$

, where $\tau_{ij}(E)$ is the transmission probability from mode *i* to mode *j*.

1.2.2 Coherent non-resonant tunneling and superexchange model

Landauer formula provides a convenient framework for describing charge transport in general mesoscopic systems. In many molecular junctions, however, calculating the transmission function is not as straightforward and requires more complicated methods. To deal with these larger systems, one of the most well accepted model is consist of two electron reservoirs denoted by the doner |D>, acceptor |A>, and the molecular bridge in between, denoted by a series of N single electron states, |1>, |2> …|N> with energy E_N. The charge carriers propagate from donner to acceptor and encounter with these molecular states. Generally, this model only considers interactions between neighboring states. Depending on the energy alignment and length of the bridge, the charge transport process can be either coherent non-resonant tunneling based on superexchange theory, or thermally activated incoherent hopping.

When the energy difference between Fermi level and molecular states is much larger than k_BT, the charge carriers tunnel through the bridge without physically residing on the molecule, named as tunneling transport (Fig. 1.2). For this situation, superexchange model and non-equilibrium Green's function formalism is typically used. In this method, the Hamiltonian of the molecular junction is described by

$$H = H_0 + V \quad (1.2.10)$$

, where H_0 is the isolated Hamiltonians of the molecule, and V is the coupling between the molecule and electrodes.

Assuming weak coupling between molecule and electrode, the transfer operator is given by

$$T = V + VG(E)V \quad (1.2.11)$$

, where $G(E)$ is the Green's function of the bridge given by

$$G = \frac{1}{E-H+i\gamma} \quad (1.2.12)$$

, with γ being the inverse lifetime matrix of bridge levels. Assuming the states only couples to their nearest neighbors, the transfer operator for the total coupling between donor and acceptor can simplified as

$$T_{DA} = V_{D1}G_{1N}V_{NA} \quad (1.2.13).$$

Assuming tight binding limit and weak coupling, G_{1N} can be expressed by

$$G_{1N} = \frac{1}{E-E_N}\prod_1^{N-1}\frac{V_{n,n+1}}{E-E_n} \quad (1.2.14).$$

In cases with identical bridge elements, for example alkane-chains, E_n and $V_{n,n+1}$ are reduced to constants E_B and V_B, therefore

$$G_{1N} = \frac{1}{V_B}\left(\frac{V_B}{E_B-E}\right)^N \quad (1.2.15).$$

Also, the transfer operator is related with the transmission function by

$$\sum_{i,j}\tau_{ij}(E) = 4\pi^2\sum_{D,A}|T_{DA}|^2\,\delta(E-E_D)\delta(E-E_A) \quad (1.2.16).$$

Therefore, we have

$$\sum_{i,j} \tau_{ij}(E) = |G_{1N}|^2 \, \Gamma_1 \, \Gamma_N \quad (1.2.17)$$

, where Γ_1 and Γ_N are coupling terms to the left and right electrodes.

Combining equation (1.2.17) and (1.2.15) gives us the following relationship for the conductance

$$g \propto |G_{1N}|^2 = \left(\frac{1}{V_B}\right)^2 \left(\frac{V_B}{E_B - E}\right)^{2N} \propto \left(\frac{E_B - E}{V_B}\right)^{-2N} = \exp\left[-\frac{2}{a} \ln\left(\frac{E_B - E}{V_B}\right) Na\right] = \exp(-\beta d) \quad (1.2.18)$$

, where d= Na is the length of the molecular bridge, and $\beta = -\frac{2}{a} \ln\left(\frac{E_B - E}{V_B}\right)$ is the decay constant. Thus in the superexchange model, the conductance is exponentially dependent on the length of molecular bridge as one would expect for tunneling through a square barrier.

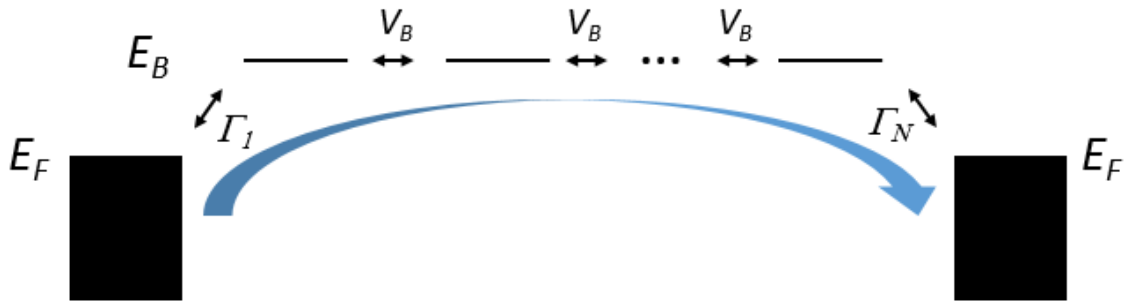


Figure 1.2 Energy diagram representation of coherent tunneling charge transport mechanism. The states are only coupled with their nearest neighbors, and the charge transfers directly from the one electrode to the other without residing on the molecular states.

1.2.3 Thermally activated incoherent hopping

In the coherent tunneling transport, the charge carrier tunnels through the junction without reside on any of the bridge states. In contrast, if the molecular length gets larger and the transport time scale get longer, the electron can occupy the bridge states and interact with the molecular vibration, thus losing its coherence. This is when sequential hopping transport mechanism comes into play[50] (Fig. 1.3).

If we consider a simple case with two scattering events, for which the transmission probability is T_1 and T_2. Since the electron loses its phase information, interference effect is neglected, so the total transmission probability T_{12} is given by

$$\frac{1}{T_{12}} = \frac{1}{T_1} + \frac{1}{T_2} \quad (1.2.19).$$

From which we know that the total resistance will be a linear combination of the two resistances

$$R_{12} = R_1 + R_2 \quad (1.2.20).$$

And if there are N scattering events, the resistance will be linearly dependent on N or the bridge length

$$R = R_c + \alpha N \quad (1.2.21)$$

, where R_c is the contact resistance, and α is the unit resistance. This linear length dependence of resistance has been observed for many long molecular wire systems, especially in biological and redox molecules.

To explain this linear length dependence, the N bridge system can be utilized again, where the charge transfer still only occurs between the nearest neighboring states. 0 state and N+1 state represent the left and right electrode. Making steady state assumption (all the states reach equilibrium), the master equations can be written as

$$\frac{dP_1}{dt} = -\left(k_{1,0} + k_{1,2}\right)P_1 + k_{0,1}P_0 + k_{2,1}P_2 = 0$$

$$\frac{dP_2}{dt} = -\left(k_{2,1} + k_{2,3}\right)P_2 + k_{1,2}P_1 + k_{3,2}P_3 = 0$$

… (1.2.22)

$$\frac{dP_{N-1}}{dt} = -\left(k_{N-1,N-2} + k_{N-1,N}\right)P_{N-1} + k_{N-2,N-1}P_{N-2} + k_{N,N-1}P_N = 0$$

$$\frac{dP_N}{dt} = -\left(k_{N,N-1} + k_{N,N+1}\right)P_N + k_{N-1,N}P_{N-1} = 0$$

, where $k_{i,j}$ is the charge transfer rate from i state to j state, and P_i is the charge density on the i state. Assuming the same rate k between all molecular state, and neglect $k_{N+1,N}$, the electron transfer rate through the whole system is given by

$$k_{0,N+1} = \frac{(k_{0,1}/k_{1,0})k}{\frac{k}{k_{N,N+1}} + \frac{k}{k_{1,0}} + N - 1} \quad (1.2.23)$$

Thus, the resistance of the whole system can be described by

$$R = \frac{k_{N,N+1}^{-1} + k_{1,0}^{-1}}{e^2\rho(E_f)} e^{E_a/k_BT} + \frac{N-1}{e^2\rho(E_f)} k^{-1} e^{E_a/k_BT} \quad (1.2.24)$$

, where E_a is the activation energy originated from $e^{E_a/k_BT} = \frac{k_{1,0}}{k_{0,1}}$, it represents the energy gap between the electrode's Fermi level and the hopping states, $\rho(E_f)$ is the density of states at Fermi level. Equation (1.2.24) explicitly shows that the resistance has a linear dependence on molecular length (N), and is also related with temperature, energy alignment, and also the coupling between the bridge and electrodes.

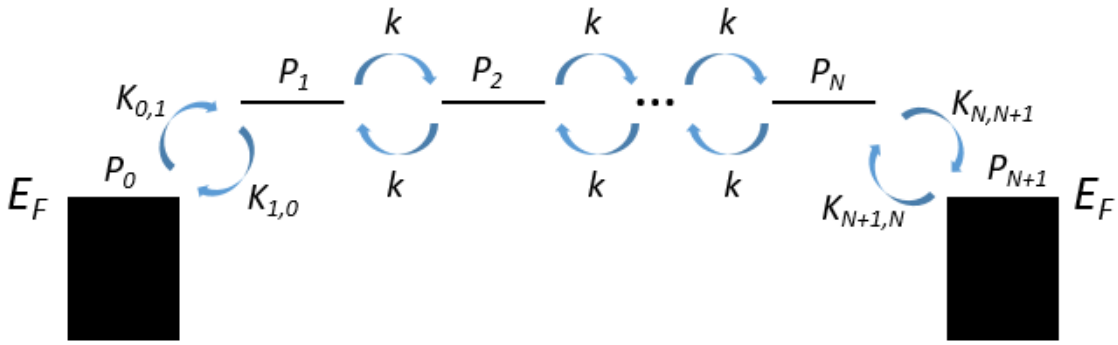


Figure 1.3 Energy diagram representation of thermally activated incoherent hopping charge transport mechanism. The charge carriers populate the states and migrate through a series of steps.

1.3 Scanning Tunneling Microscopy (STM) Break Junction Technique

Back to 1981 when scanning tunneling microscopy (STM) was first invented, it was used to image a conductive surface at scale as small as atomic level. The principle of scanning relies on the exponential dependence of tunneling current on distance, which can be described as

$$I=I_0 e^{-\beta L} \quad (1.3.1)$$

, where I_0 is the contacting current depending on the electron density at the Fermi level, β is the decay constant of the medium, L is the distance. Because STM system is capable of precisely controlling the distance and monitoring the electronic current at the same time, it seems to be very promising tool for measuring metal-molecule-metal junctions. In 2003, Tao and co-workers developed STM break junction technique[11] to conduct fast, repeated measurements and statistical analysis of single molecular junctions. Fig. 1.4 is a sketch of STM break junction technique. A self-assembled monolayer is formed by the target molecules with both ends reactive with metal electrodes (Fig. 1.4a). The STM tip is first brought into contact with the sample to form molecular junctions (Fig. 1.4b), then retracted at a constant speed, during which the conductance-distance traces are recorded (Fig. 1.4c-d). At the forming of molecular junctions, plateaus are observed on the conductance-distance trace, giving the conductance value of the junctions (Fig. 1.4e). When the tip is pulled far enough from the substrate, the molecular junctions are broken (Fig. 1.4d-e), causing a sharp drop in the conductance of the gap between the tip and substrate. Thousands of conductance-distance traces are combined into a histogram with peaks showing the most probable conductance values of molecules (Fig. 1.4f). Sometimes there are multiple peaks presented in the conductance histograms. Usually the peak corresponding to the lowest conductance is attributed to single molecular junction, while other peaks are from multiple molecules bridged in between.

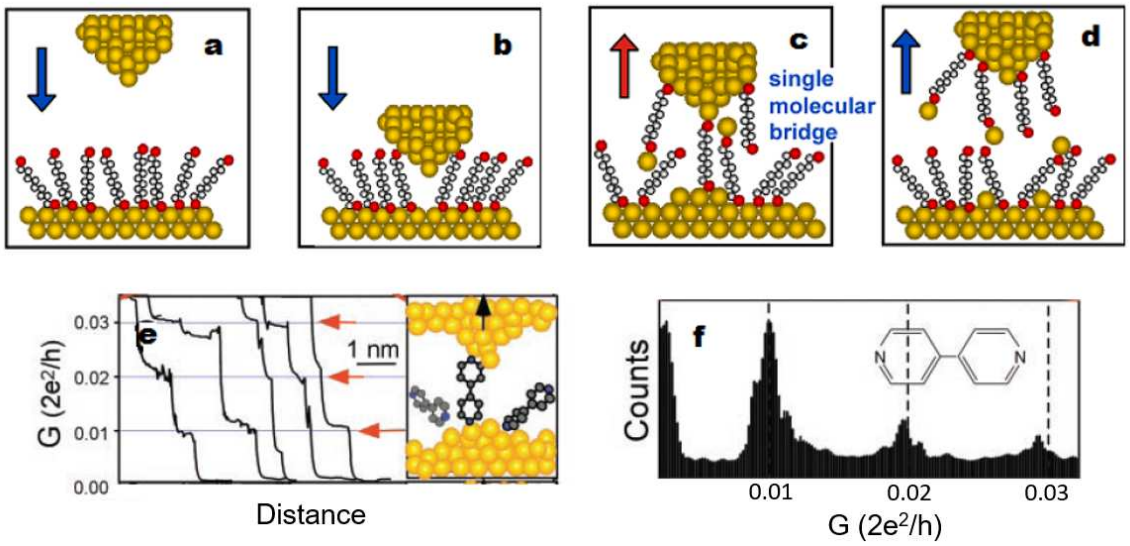


Figure 1.4 Measurement of single molecule conductance with STM break junction technique. (a) The STM tip approaches the substrate. (b) Molecular junctions are formed. (c) The STM tip is pulled away from the substrate. (d) Molecular junctions are broken. (e) Conductance-distance traces of 4, 4'- bipyridine. (f) Conductance histogram of 4, 4'- bipyridine. (Figures obtained from [11])

To date, STM break junction technique has been successfully utilized by several groups around the world and approved to be an effective and robust technique. The technique has also been adapted in various ways to obtain additional information or introduce other physical parameters. For example, the tip can be halted once the formation of molecular junction is detected, then by sweeping the bias, the current-voltage characteristics can be performed, from which one can resolve valuable information such as tunneling barrier height[41, 51, 52], differential conductance[53, 54], and inelastic tunneling spectroscopy[55, 56]. Moreover, by modifying the setup, researchers have

introduced many interesting physical parameters (electrochemical gate[57], temperature[28], force[31], etc) into their experiments, providing ways to look into the interplay between various physical influences and electronic properties. In addition, there's a wide range of environment that STM can perform in, including ultra-high vacuum, the air, some low-conductivity solvents, and conductive solvent like water and ionic liquid (with Apeizon wax coated tip). Above all, since STM break junction technique relies on statistical study, the experimental results have shown high reproducibility across labs. All these great features make the STM break junction technique a powerful tool in the study of molecular junctions.

1.4 Thermoelectric Effects in Molecular Junctions

Thermoelectric effect, also known as Seebeck effect is the direct conversion of temperature difference into electric voltage. The reverse effect is referred as Peltier effect, in which the effect of heating or cooling presents at the electrified junction of two different conductors. Based on these effects, many thermoelectric energy conversion devices were built, for example, thermocouple thermometer and semiconductor heater or cooler. To provide a measure of the temperature to voltage conversion efficiency, the Seebeck coefficient *S* is used and defined as in

$$\Delta V = V_2 - V_1 = \int_{T_1}^{T_2} -S(T)dT \quad (1.4.1)$$

, where *S* is dependent on absolute temperature. Normally, within small temperature difference, S is treated as a constant given by

$$S = -\frac{\Delta V}{\Delta T} \quad (1.4.2).$$

When several pieces of materials are connected linearly in the circuit, the voltage generated can be described as

$$V = \sum_i \int_{T_{i1}}^{T_{i2}} -S_i(T)dT \quad (1.4.3)$$

, where T_{i1} and T_{i2} are the temperatures applied to material i, and S_i is its Seebeck coefficient.

Basically, the Seebeck effect comes from the accumulation of charge carries moving from one side of the material to the other. The charge carriers move along the thermal gradient in both bulk materials via diffusion and molecular junctions via tunneling or hopping. Fig. 1.5 illustrates two examples of electron transfer through LUMO and hole transfer through HOMO. When the electrode's Fermi energy is closer to the LUMO of the bridged molecule, the charge transport will occur mainly through LUMO, and electrons has larger transmission probability comparing to holes. Therefore, more electrons will be transport from the hot side to the cold side, leading to a net negative thermoelectric current. Similarly, when the electrode's Fermi energy is closer to the HOMO, holes will be the main charge carriers and move from the hot side to the cold side, resulting in a net positive thermoelectric current.

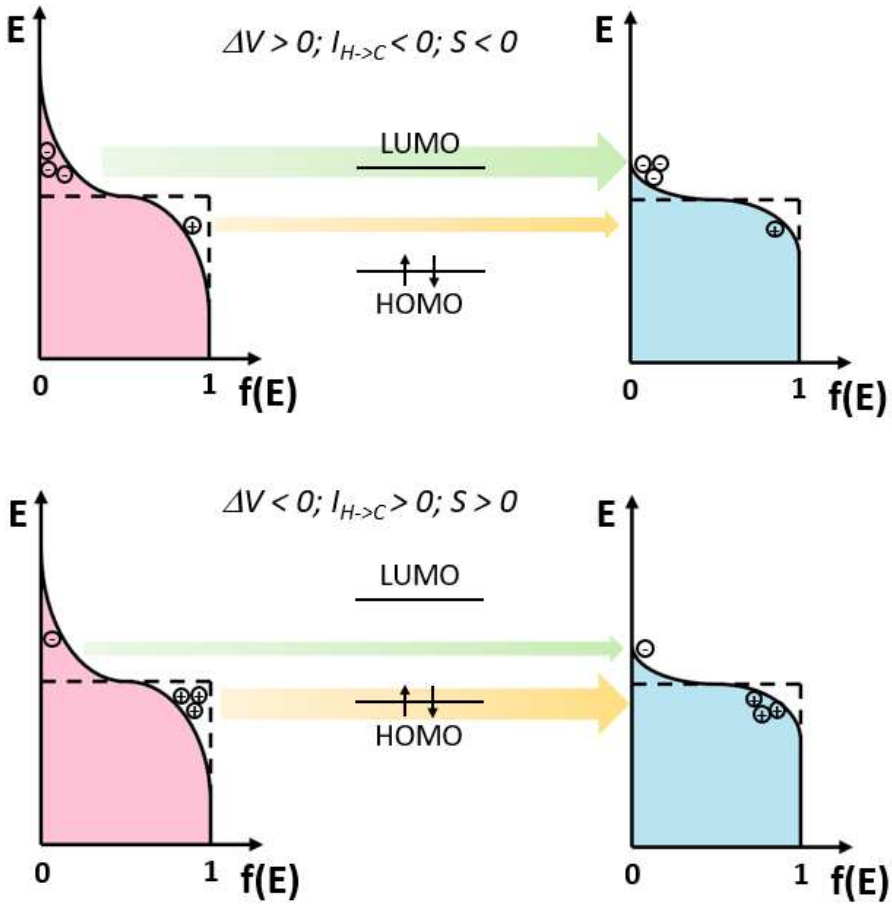


Figure 1.5 Energy diagram of thermoelectric effect in molecular junctions with (a) LOMO transport and (b) HOMO transport.

The thermoelectric effect can also be reflected from a simplified model within the Landauer framework. Take the scenario of LUMO transport for example, the current through a molecular junction is given by

$$I_{H\to C} = -\frac{2|e|}{h}\int \tau(E)\,[f_H(E,\mu_H,T_H) - f_C(E,\mu_C,T_c)]\,dE \quad (1.4.4)$$

, where e is the charge carried by an electron, h is Plank constant, $\tau(E)$ is transmission function, f_H and f_C are Fermi-Dirac functions for the hot and cold electrode, E is energy, μ_H and μ_C are chemical potentials of the hot and cold electrodes, T_H and T_c are the absolute temperatures of the hot and cold electrodes. For hole transport through HOMO, 1-f is used instead of f.

By applying the Sommerfield expansion (equation 1.4.5), equation (1.4.4) can be transformed into

$$\int \frac{H(E)}{e^{\beta(E-\mu)+1}} dE = \int_{-\infty}^{\mu} H(E)dE + \frac{\pi^2}{6}\left(\frac{1}{-\beta}\right)^2 H'(\mu) + O\left(\frac{1}{\beta\mu}\right)^4 \quad (1.4.5)$$

$$I_{H\to C} \approx -\frac{2|e|^2}{h}\tau(E_F)\Delta V - \frac{2|e|}{h}\frac{\pi^2 {k_B}^2 T}{3}\frac{\partial\, \tau(E)}{\partial E}\Big|_{E=E_F} \Delta T \quad (1.4.6)$$

, where $\Delta V = -\frac{(\mu_H-\mu_C)}{|e|}$, $\Delta T = T_H - T_C$, and $T = \frac{1}{2}(T_H + T_C)$.

Assuming small bias and temperature gradient, one have

$$\Delta V|_{I_{H\to C}=0} = \frac{\pi^2 {k_B}^2 T}{3|e|}\frac{\partial \ln[\tau(E)]}{\partial E}\Big|_{E=E_F} \Delta T \quad (1.4.7)$$

Therefore,

$$S_{junction} = -\frac{\Delta V}{\Delta T} = -\frac{\pi^2 {k_B}^2 T}{3|e|}\frac{\partial \ln[\tau(E)]}{\partial E}\Big|_{E=E_F} \quad (1.4.8)$$

Equation (1.4.8) indicates that Seebeck coefficient is associated with the slope of transmission function at the Fermi level, which is determined by the molecular level,

coupling and Fermi level of electrodes. Interestingly the expression of Seebeck coefficient for molecular junctions is similar to that for bulk materials given by,

$$S_{bulk} = -\frac{\Delta V}{\Delta T} = \frac{\pi^2 {k_B}^2 T}{3|e|} \frac{\partial \ln R}{\partial E}\Big|_{E=E_F} \quad (1.4.9)$$

, where R is the resistance of the bulk material. The similarity provides us another aspect to compare and understand the thermoelectric effect in different scales.

The measurement of thermoelectricity of molecular junctions was first carried out by Reddy et, al.[28] in 2007. There measurement was conducted by a room temperature STM break junction set up, which combines a DC current preamplifier and a voltage amplifier (Fig. 1.6a). Monitored by the current preamplifier, the cold tip was approached toward the heated substrate functionalized with molecules until the current reached a set point where the distance between the tip and substrate is short enough to form molecular junctions. Then the tip was retracted, the bias was turned off, and the circuit was switched to the voltage amplifier to measure the thermoelectric voltage. This approach provides a straightforward way to obtain the Seebeck coefficient from the direct measurement of thermoelectric voltage. However, the number of molecules bridged in between is not reflected, and the relationship between the conductance and Seebeck coefficient could not be observed.

In 2012, Widawsky et, al.[29] conducted the direct current measurement to measure the single molecule thermoelectric effect using a room temperature STM break junction set up. They also approach the cold tip to the heated substrate functionalized with molecules

until close enough to form molecular junctions, and then retract the tip by a predefined distance and hold it for a period of time, during which the bias is turned off and back on. An electrometer was used to monitor the current. The conductance of molecular junction was resolved from the current of the bias-on portion, while the thermoelectric current was the current of the bias-off portion (Fig. 1.6b). Before the thermoelectric measurement, they performed conventional conductance measurement to find out the reasonable range for single molecule. According to this range, they selected the data corresponding to single molecular junctions, and extract the Seebeck coefficient from the thermoelectric current. This method measured the conductance and thermoelectric effect within a very short time window, which enabled single molecule measurement, but still lacks direct evidence that the data corresponding to single molecular junctions.

To really simultaneously measure the conductance and thermoelectricity, Shaoyin et, al. used the rapid current-voltage (I-V) curve measurement method[30] with a STM break junction set up (Fig. 1.6c). The tip was repeatedly approach toward, making contact and retracted from the substrate functionalized with molecules. Once a molecular junction is formed and detected, a rapid bias sweep over a small range (10 mV) will be performed. From the statistic study of the I-V curves, they get the thermoelectric current at zero bias, and obtained the thermoelectric voltage at zero current. Similar method was employed for my measurement of the thermoelectric effect in single DNA molecules. More details can be found in Chapter 2.

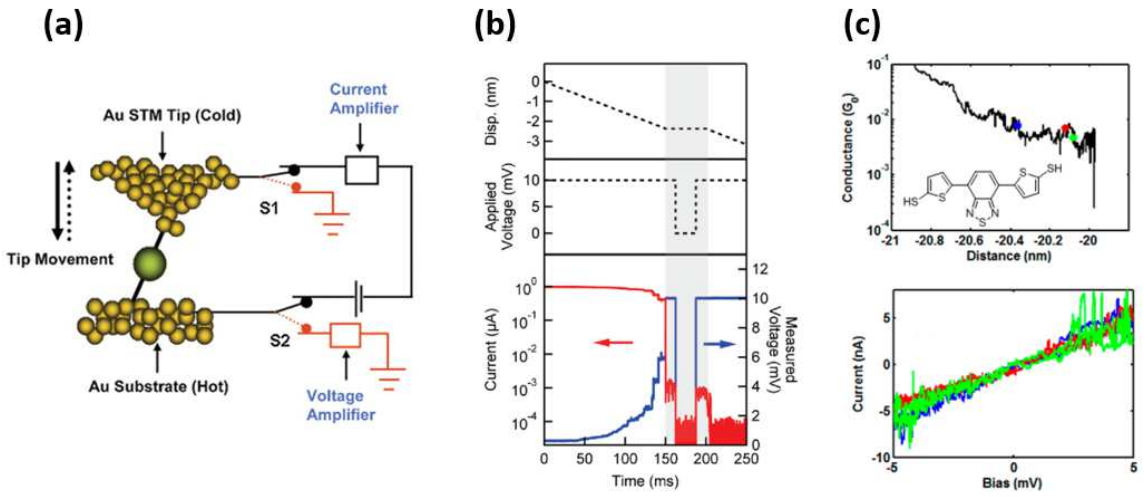


Figure 1.6 Illustrations of different methods of thermoelectric measurement. (a) Experimental set up of thermoelectric voltage measurement of molecular junctions. (Figure obtained from [28]) (b) Thermoelectric current measurement procedure. (Figure obtained from [29]) (c) Thermoelectric rapid I-V measurement procedure. (Figure obtained from [30])

1.5 Charge Transport/Transfer in DNA

Charge transport/transfer (CT) in DNA has been a hot topic for decades, and was investigate mainly by the method of photochemistry, electrochemistry or molecular electronics. Among the four bases, Guanine has the lowest ionization energy, followed by Adenine, so the CT mainly happens by the hole transport through the HOMO of Guanine and Adenine.

It is commonly agreed that CT through GC (Guanine Cytosine) base pairs occurs via sequential hopping, while for short AT (Adenine Thymine) base pairs, tunneling is responsible for the CT, then as the number of AT base pairs increase, hopping becomes dominant. The different pattern between CG and AT base pairs can be attributed to the lower activation energy of CT through G base, thus making thermally activated hopping to be the main pathway of CT. The transition from tunneling to hopping dependent on the number of AT base pairs has been observed by many groups using different methods. For example, Giese et, al.[58] used the photolysis of 4'-acylated nucleotide to generate a radical cation, which propagated through the bridge consists of repeating AT base pairs. By measuring the oxidized damaged product, they resolved the charge transfer efficiency, and noticed the CT mechanism changes from tunneling to hopping at the distance of 3 AT base pairs. Another method of photochemical measurement of CT in DNA was first developed by Lewis and Wasielewski in 1997 [59, 60]. They modified the double strand (ds) DNA with a hole donor group on one end and a hole acceptor group on the other, then used a time-resolved fluorescence spectroscopy to monitor the intensity at 575 nm and 525 nm, which correspond to the hole density at the donor and acceptor species, respectively (Fig. 1.7a). From the intensity v.s. time they were able to extract the charge transfer rate constant. And they also observed a transition from tunneling to hopping at the distance of 3 repeating AT base pairs[61] (Fig. 1.7b).

Another intensely utilized platform for analyzing CT through DNA is electrochemical methods developed by Barton et, al[62, 63]. ds DNA molecules were modified with a redox group (methylene blue, anthraquinone or nile blue) on one end and

thiol group on the other end to bind with Au surface[64] (Fig. 1.7c). By performing cyclic voltammetry under different scan rate and applying Laviron analysis[65], the charge transfer rate constant through the DNA molecule was measured. It worth noting that the charge transfer rate constant measured by electrochemical methods is different than that measured by photochemical methods by 1 orders of magnitude, probably because photochemical methods measures excited state, while electrochemical methods measures ground state.

In addition to the characterizations with chemical methods, direct measurement of charge transport in DNA is also possible by applying bias across a metal-molecule-metal junction. For instance, Porath et, al.[66] employed conducting AFM to measure the current-voltage (I-V) characteristics of ds DNA bridged in between Au surface and Au nanoparticle. More examples can be found in the STM break junction measurements, such as conductance measurements by Xu et, al[67]. on thiolated ds DNA molecules (Fig. 1.7d).

The theoretical framework of CT in DNA has also been intensely developed in recent years by theoretical models[68-70] and computational simulations[71-73]. The hopping transport mechanism through GC base pairs and transition from tunneling to hopping in AT base pairs were successfully confirmed and explained by theoretical calculations[71].

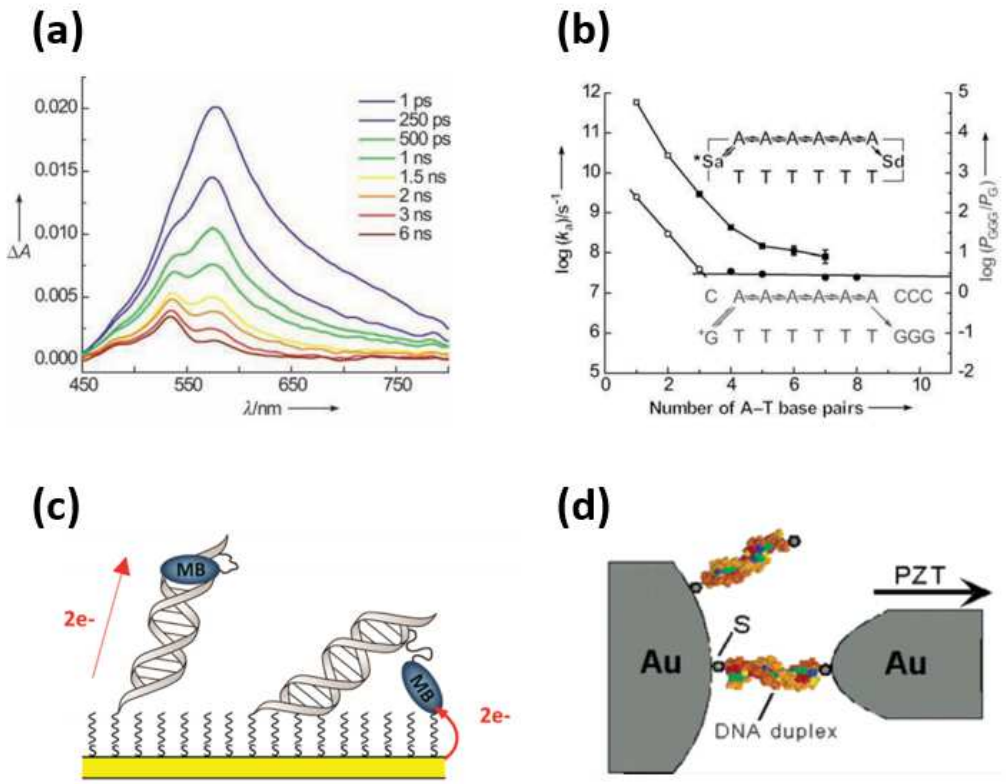


Figure 1.7 Illustrations of different methods of charge transfer/transport through DNA. (a) In the photochemistry measurement, transition absorption spectroscopy from 1 ps to 6 ps shows a changing ratio of the two peaks at 575 nm and 525 nm. (b) Charge transfer rate constant changing with the number of AT base pairs. (Figures a and b obtained from [61]). (c) In the electrochemistry study of DNA charge transport, DNA molecules intercalated with methylene blue (MB) are immobilized on Au surface by thiol groups. (Figures a and b obtained from [64]) (d) In STM break junction measurement of DNA charge transport, single DNA molecule bridge in between two electrodes biased with a small voltage. (Figures a and b obtained from [67])

1.6 Single Molecule Electrochemical Measurement

The conventional CMOS technology relies heavily on three terminal devices, thus making it encouraging for molecular electronics to add a third terminal to the metal-molecule-metal system to realize a more profound control. Different types of gating method have been developed (back gate[74], chemical gate[75] and electrochemical gate[13]), among which electrochemical gate is the most readily built, and can be most straightforwardly controlled and understood. By adding a reference electrode in touch with the electrolyte and insulating the STM tip with Apeizon wax, electrochemical potential can be applied to the molecule to shift the relative alignment between molecular levels and electrode Fermi levels during the STM break junction measurements (Fig. 1.8). In this way, one can measure the electrochemical gate dependency of the interested electronic properties, or conversely control the electronic properties with gating. For example, Diez-Perez et, al.[26] reported an enhancement of 2 orders of magnitude in the conductance of coronene molecule under a negative gate potential, because the Fermi level of electrodes is shifted closer to the LUMO level.

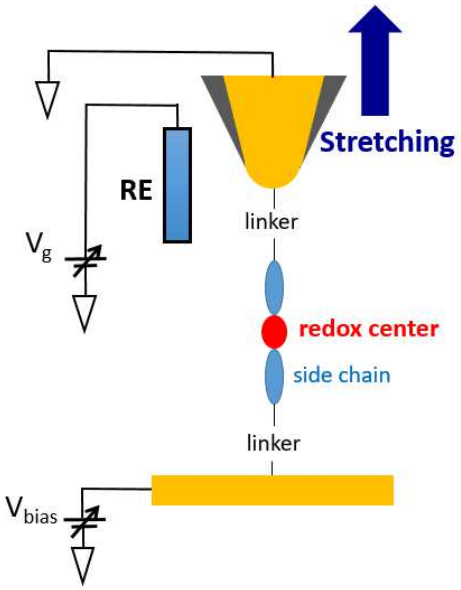


Figure 1.8 Illustration of the electrochemical STM measurement set up. The source and drain electrodes are the STM tip and substrate, and EC gate is a silver electrode. The source-drain bias (V_{bias}), and the EC gate voltage (V_g) are controlled independently.

It is especially of great interest that electrochemical gate can be employed to control the redox state of a redox active molecule bridged between electrodes. Conductance switching between two states at different potentials was reported in many studies[76, 77]. When the redox state of molecule can be reflected by the level of conductance, by doing statistical study of conductance and plateau length, one can then determine the relative popularity of reduced and oxidized species under certain electrochemical gate potential. Because in a conductance histogram, *S*, the area of the conductance peak for single molecular junction can be expressed by[78],

$$S = n_j \cdot \frac{Lf}{vU}, \qquad (1.6.1)$$

where n_j is the number of molecular junctions (traces with plateau), L is the plateau length of the plateau, f is the sampling frequency, v is the pulling rate in nm/s and U is the number of bins in the conductance histogram. When f, v, and U are kept the same for each experiment, the peak area S is proportional to the product of n_j and L. Because the oxidized state and reduced state are measured under exactly the same circumstances, and their structures are only differed by the redox moiety, we believe that their yield of forming molecular junctions are proportional to the surface coverage of the species. Therefore, ideally the peak area, S is proportional to the product of surface coverage of species and plateau length.

Apart from discrete levels of conductance under different gate voltages, different patterns of gate dependency of conductance were also discovered for redox molecules. For example, Xiao et. al.[79] reported a gradual increase of conductance for Ferrocene derivatives as the gate voltage increases. And Osorio et, al. observed a conductance maximum at redox potential of bipyridinium molecule[27], which can be explained by the two step model[80].

1.7 Molecular Mechanochemistry Done by STM Break Junction Measurements

Mechanical energy has been known to induce chemical reactions since time immemorial, for example making fire. Mechanochemistry[81], as a field of research, arises from the interface between chemistry and mechanical engineering. In the long history of mechanochemistry, extensive studies have been devoted to mechanical activation of reactions in bulk systems[82, 83], where shear, friction and compressive force play the key roles. The landscape of mechanochemistry was substantially expanded when the skill of force control evolves from conventional tools (grinding or milling) to advanced techniques (atomic force microscopy[84], optical tweesers[85], molecular force probes[86], etc). By applying forces or stresses at molecular length scales on part of the molecule, the chemical bonds are mechanically activated, yielding products of interest, which defines the realm of molecular mechanochemistry[87]. A wide range of processes at single-molecule scale were studied. The effect of mechanical tension on polymers, for instance, were found to cause structural change varying from simple conformational changes to bond stretching and deformation[87]. Another important example is the study of force-induced rupture of the sulfur-sulfur bond in biopolymers[88-90]. It has also been shown that forces or stresses can trigger physiological processes such as unfolding of proteins[91] and DNA[92].

The physical basis for mechanically activated reaction first proposed by Erying and Kauzmann[93] attributes the change in reactivity to a decreased activation energy. Specifically, the force alters molecular structures to lower the barrier, meanwhile the

work performed by the force supplies energy to promote reactions[94]. As a result, the energy landscape was tilted by the force. The simplest model describes the activation energy to be proportional to the magnitude of the applied force, and to the conformational change aligned with the force[93, 95]. The approach of mechanochemistry is distinct from thermochemical, photochemical and electrochemical methods because of the directional nature of force and high spatial resolution of fine management over nuclear degrees of freedom, leading to its outstanding convenience in controlling reaction rates and equilibriums, steering reaction to follow specific pathways, and maintaining mild reaction conditions.

To adopt the method of mechanochemistry in STM break junction measurements, we need to first understand the force within the molecular junctions. Obviously, we are applying a stretching force during the retracting phase in the break junction process. From a bond elasticity of view, the magnitude of the force at breakdown should be determined by the softest bond along the junction. To understand the break down mechanism, Xu et, al.[96] employed a conducting AFM set up to perform break junction measurements for octanedithiol, which bind to the electrodes via Au-S bond, and bipyridine, which bind to the electrodes via Au-N bond (Fig. 1.9). The breakdown force of octanedithiol was measured to be 1.5 ± 0.2 nN, which is similar to the breakdown force of gold atomic wire (1.5 nN). And the smallest spring constant of Au-Au bond among all the bonds involved in an octanedithiol molecular junction verifies the assumption that the breakdown happens at the Au-Au bond. In contrast, the breakdown force of bipyridine was found to be 0.8 ± 0.2 nN. This is because the Au-N bond is the

weakest point in a bipyridine junction, and the breakdown force is defined by the spring constant of Au-N bond. Since then, the breakdown force of molecules with a variety of linkers have been studied by many works using conducting AFM[97-99]. These studies all agree that the largest possible breakdown force in a molecular junction formed in between gold electrodes is 1.5 nN, which is the breakdown force of Au atomic wire. Informed by the magnitude of breakdown force, it becomes possible for us to characterize the force effect in electromechanical measurements and in force induced electron transfer process. Bruot et, al. measured the force dependence of conductance for 1,4'-Benzenedithiol with STM break junction technique. They observed a positive relationship between the stretching force and conductance, and attributed the dependence to the force-induced change in the molecule-electrode coupling. In the third chapter of this thesis, we will look into the mechanochemistry done by STM break junction, in which a redox reaction of Ferrocene is induced by mechanical force.

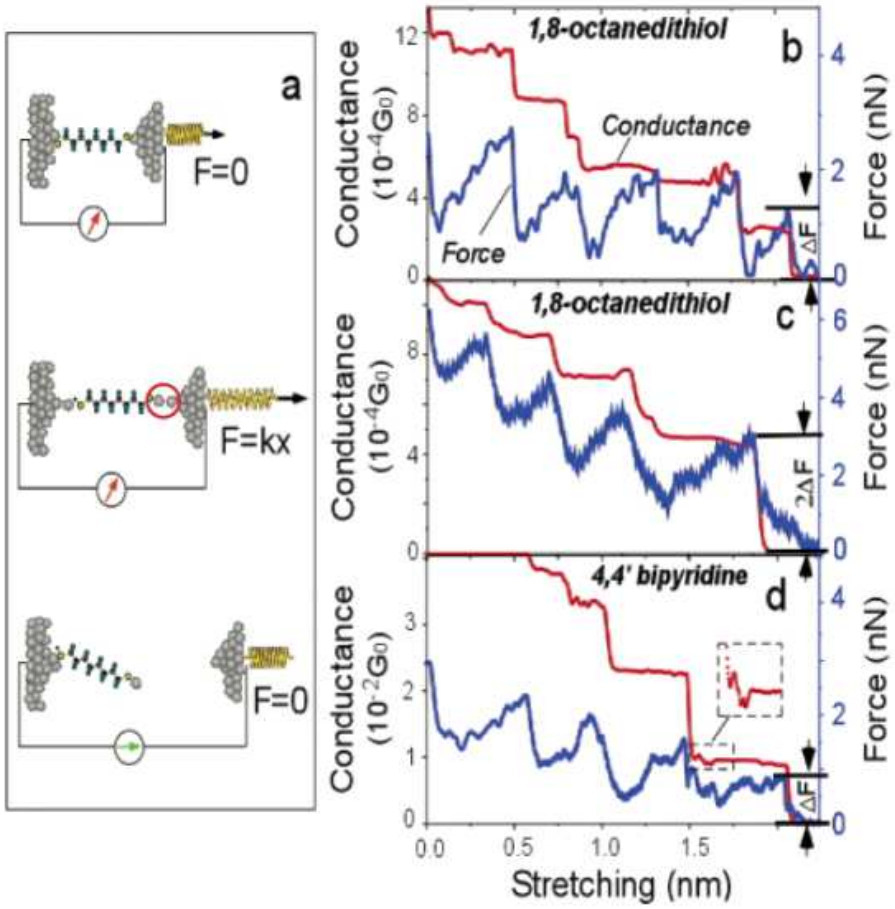


Figure 1.9 Measurement of the breakdown force of molecular junction with AFM. (a) Schematic illustration of the breakdown process of a molecular junction, during which both the conductance and the force are monitored. (b-d) Conductance and force vs. distance plotted for 1,8-octanedithiol (1 molecule in b and 2 molecules in c) and 4,4`-bipyridine (d). (Figures obtained from [96])

2 THERMOELECTRIC EFFECT AND ITS DEPENDENCE ON MOLECULAR LENGTH AND SEQUENCE IN SINGLE DNA MOLECULES

2.1 Introduction

The thermoelectric effect is a basic property of materials and has been employed in energy conversion, temperature sensing and regulation. This important effect in single molecules is expected to differ from that in bulk materials.[100] In addition to potential applications, investigating the thermoelectric effect in single molecules helps analysis the molecular orbital level alignment, understand the energy conversion mechanism associated with charge transport, and find out whether electrons or holes are responsible for the charge transport. The work by Reddy et al.[28] has stimulated many works focusing on the thermoelectric effect in molecules.[101-104] However, to date, research has been limited to the coherent tunneling regime, which is a quantum mechanical process with a characteristic exponential dependence of the molecular resistance with length.

Here I demonstrate a study of the thermoelectric effect in double-stranded DNA molecules. By selecting different DNA sequences, I study the thermoelectric effect not only in the tunneling regime, but also in the hopping regime, which has a linear dependence of the molecular resistance with length. The work shows that DNA thermoelectricity can be tuned by its sequences and length, which provides new insights into the thermoelectric effect in single molecules, and basic knowledge for potential applications with programmable DNA nanostructures[105].

2.2 Methods

2.2.1 Preparation of dsDNA SAM

All DNA molecules were purchased from Bio-Synthesis Inc. The T terminal of each DNA molecule was modified with an amine group[106], allowing covalent binding to gold electrodes for electrical measurement. The name and structure of all the sequences are listed in Table 2.1. The DNA molecules were annealed by a thermal cycler (TC-050-18, Labnet Inc) to form the B-form double helical structure in phosphate buffer. The B-form structure was verified by gel electrophoresis, circular dichroism and melting curve (See section 2.7.1~2.7.3). The phosphate buffer was prepared with $Na_2HPO_4{\cdot}2H_2O$ (for HPLC, ≥ 98.5%) and NaH_2PO_4 (for HPLC, ≥ 99%) purchased from Fluka. The DNA molecules were immobilized on a gold substrate (gold with thickness of ~160 nm on mica) prepared in a vapor deposition system under ultra-high vacuum. Before each experiment, a new gold substrate was annealed with hydrogen flame briefly, and immediately immersed into phosphate buffer (5 mM, pH=7) containing 5 μM double helical DNA, incubated overnight. The substrate electrode was then rinsed with phosphate buffer and dried by nitrogen flow. The DNA-coated gold substrate was attached to the sample holder of the STM, which was placed in a glove box under nitrogen atmosphere with relative humidity of about 20%.

2.2.2 STM setup

The charge transport and thermoelectric measurements were performed with the STM consisting of a controller (Nanoscope IIIA, Digital Instruments Inc.) and a STM scanner (Molecular Imaging). The STM tip was freshly cut from a gold wire (0.25 mm diameter, 99.95%, Alfa Aesar). As a thermal reservoir, a piece of electrically shielded copper strip (0.7 cm×0.4 cm×2 cm) was thermally connected to the STM tip holder. The STM sample holder was attached with a semiconductor cooler with a thermistor to measure the temperature (controlled by Lake Shore 331 temperature controller).

2.2.3 Measurement of thermoelectricity

The STM break junction technique was utilized to measure the conductance of DNA with a procedure described in detail elsewhere [11] (Fig. 2.1a). Briefly, the STM tip was first brought into contact with the DNA molecules on the gold substrate, allowing the amine-terminated DNA to bind with the gold electrodes. Then the tip was retracted at a constant speed from the substrate, during which a conductance-distance trace was recorded. The last plateau in the conductance trace corresponds to a single DNA molecular junction. The process was repeated thousands of times. A conductance histogram was constructed from the individual conductance traces, and the peak position in the conductance histogram gave the average conductance of the DNA molecule.

To measure the thermoelectric effect of DNA molecules, I introduced a temperature gradient across the molecule by cooling the sample holder while maintaining the STM tip at the room temperature[30]. During the experiment, the temperature of the sample was monitored with thermistors. When a molecular junction was formed as indicated by the formation of a plateau feature in the conductance-distance trace, the tip was held in position and a I-V curve was recorded. Then the tip was retracted further away from the substrate by an additional distance. If the current did not drop abruptly, suggesting that the molecular junction was still intact, another I-V curve was recorded. Otherwise, the measurement was started over again.

More than two thousands of I-V curves were recorded for each temperature gradient. These I-V curves were normalized by conductance (G) and combined into a two dimensional I/G vs. V histogram. The voltage offsets in the I/G vs. V histogram were used to construct a histogram of thermoelectric voltage, and Gaussian fitting of the thermoelectric voltage histogram at different temperatures provided the Seebeck coefficient of DNA. Controlling the STM tip movement, recording and processing the experimental data described above were achieved with Labview 8.5 and data acquisition card.

2.3 Double Stranded DNA Sequences

To investigate the thermoelectric effect in the hopping regime, I chose DNA molecules with sequences of 5'-A$(CG)_n$T-3' (n=3, 4, 5, 6, and 7) (Fig. 2.1b), where A, C, G and T denote the four DNA bases, adenine, cytosine, guanine and thymine,

respectively. Note that this sequence notation shows only one strand of the double stranded DNA (dsDNA), and the second strand has the complementary sequence. The complete sequences of all the dsDNA measured in this work are listed in Table 2.1. Previous studies have shown that charge transport in GC sequences is dominated by hopping of holes along the molecule with each G base as hopping site[59, 107-111]. To investigate the thermoelectric effect in the tunneling regime, I looked into DNA sequences, 5'-ACGC$(AT)_m$GCGT-3', where m=1, 2, 3 and 4, and 5'-ACGC$(AT)_{m-1}$AGCGT-3', where m=1, 2, and 3 (Fig. 2.1b and Table 2.1). The insertion of a block of AT bases in the middle of the GC sequences introduces a tunneling barrier in between the hopping bridges, as shown in literature,[112-117] allowing us to study the thermoelectric effect in the tunneling regime. To measure the DNA with STM electrodes, we modified T base at the 3' end with an amino group, which binds to gold electrodes to establish electrical contact between the electrodes and the molecule[106].

Table 2.1 Sequences of dsDNA Studied in This Work

Name	Duplex	Abbreviation
$A(CG)_3T$	5’-ACGCGCGT-3’ 3’-TGCGCGCA-5’	$A(CG)_nT$
$A(CG)_4T$	5’-ACGCGCGCGT-3’ 3’-TGCGCGCGCA-5’	$A(CG)_nT$
$A(CG)_5T$	5’-ACGCGCGCGCGT-3’ 3’-TGCGCGCGCGCA-5’	$A(CG)_nT$
$A(CG)_6T$	5’-ACGCGCGCGCGCGT-3’ 3’-TGCGCGCGCGCGCA-5’	$A(CG)_nT$
$A(CG)_7T$	5’-ACGCGCGCGCGCGCGT-3’ 3’-TCGGCGCGCGCGCGCA-5’	$A(CG)_nT$
ACGCAGCGT	5’-ACGCAGCGT-3’ 3’-TGCGTCGCA-5’	$ACGC(AT)_{m-1}AGCGT$
ACGCATGCGT	5’-ACGCATGCGT-3’ 3’-TGCGTACGCA-5’	$ACGC(AT)_mGCGT$
ACGCATAGCGT	5’-ACGCATAGCGT-3’ 3’-TGCGTATCGCA-5’	$ACGC(AT)_{m-1}AGCGT$
$ACGC(AT)_2GCGT$	5’-ACGCATATGCGT-3’ 3’-TGCGTATACGCA-5’	$ACGC(AT)_mGCGT$
$ACGC(AT)_2AGCGT$	5’-ACGCATATAGCGT-3’ 3’-TGCGTATATCGCA-5’	$ACGC(AT)_{m-1}AGCGT$
$ACGC(AT)_3GCGT$	5’-ACGCATATATGCGT-3’ 3’-TGCGTATATACGCA-5’	$ACGC(AT)_mGCGT$
$ACGC(AT)_4GCGT$	5’-ACGCATATATATGCGT-3’ 3’-TGCGTATATATACGCA-5’	$ACGC(AT)_mGCGT$

2.4 Length Dependence of Conductance

I measured the DNA conductance and thermoelectric effect with a temperature controlled Scanning Tunneling Microscopy (STM) setup shown in Fig. 2.1a, following a procedure described in detail elsewhere[11] (see also methods section). The conductance vs. STM tip-substrate distance traces show plateaus associated with the formation and breakdown of single molecule junctions (marked with arrows in the red traces in Fig. 2.1c). I also performed the experiment without DNA as a control, and observed no characteristic plateaus in the conductance traces (black traces). By collecting thousands of conductance traces, I constructed a conductance histogram (Fig. 2.1d), which shows a broad peak, where the peak position measures the average conductance of a single dsDNA molecule. The width of the histogram peak reflects the intrinsic variability and distribution in the molecule-electrode binding geometry.[118] To determine the experimental error, I repeated the above experiment more than three times, each of which using a new sample to generate thousands of conductance traces, for every DNA sequence, and used the standard deviation in the conductance values as the error bar.

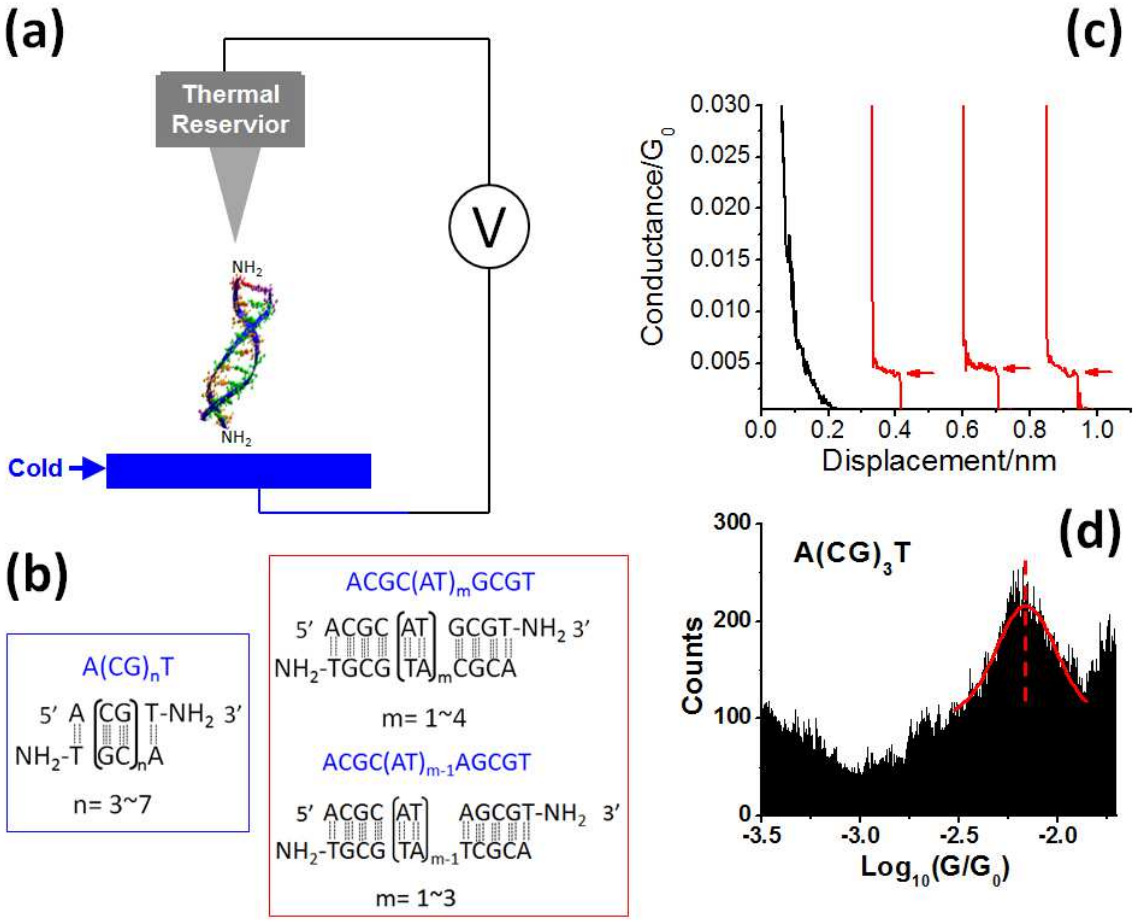


Figure 2.1 Thermoelectric and conductance measurements of DNA. (a) Conductance and thermoelectric effect of a DNA molecule bridged between STM tip (kept at 295K) and substrate (cold). (b) Two families of DNA sequences are studied in this work, denoted as (1) $A(CG)_nT$, (2) $ACGC(AT)_mGCGT$ and $ACGC(AT)_{m-1}AGCGT$ (see Table 2.1 for a full list). (c) Conductance traces without (black) and with dsDNA $A(CG)_3T$ (Red), where plateaus are marked with red arrows. (d) Conductance histogram of $A(CG)_3T$, where the solid red curve is Gaussian fit to the conductance peak. Note: $G_0 = 2e^2/h = 77.48$ μS.

I characterized the DNA samples by performing non-denaturing polyacrylamide gel electrophoresis, circular dichroism spectroscopy and melting temperature experiments in phosphate buffer (See section 2.7.1~2.7.3). These experiments demonstrated that each DNA sequence studied here was in B-form double helical structure in phosphate buffer. To ensure the DNA molecule still retained its double helical structure in the experiments (~20% relative humidity), I compared the conductance of DNA measured in humidified air with that measured in phosphate buffer, and found similar values within the experimental uncertainty (Section 2.7.4 and 2.7.5). Another parameter that characterizes molecular junction stability is the plateau length, which is the average distance that one can stretch the junction before it breaks. The stretching length reflects the breakdown of the hydrogen bonds at the very end of the dsDNA. Fig. 2.2 shows the stretching length histograms of A(CG)3T in the air and in solution, and Gaussian fittings to the histograms. From the fittings, the average stretching lengths were found to be 0.11 nm and 0.12 nm, respectively. The similarity in the stretching length measured in air and in solution confirms that the dsDNA retained its native structure in humidified air. These facts led me to conclude that the DNA molecules in humidified air retained its double helical structure, possibly due to a thin absorbed water layer on the substrate surface. This conclusion is also supported by AFM[119], STM[120], mechanical break junction[121], and polarization modulation IR[122] measurements of dsDNA on a surface in the air.

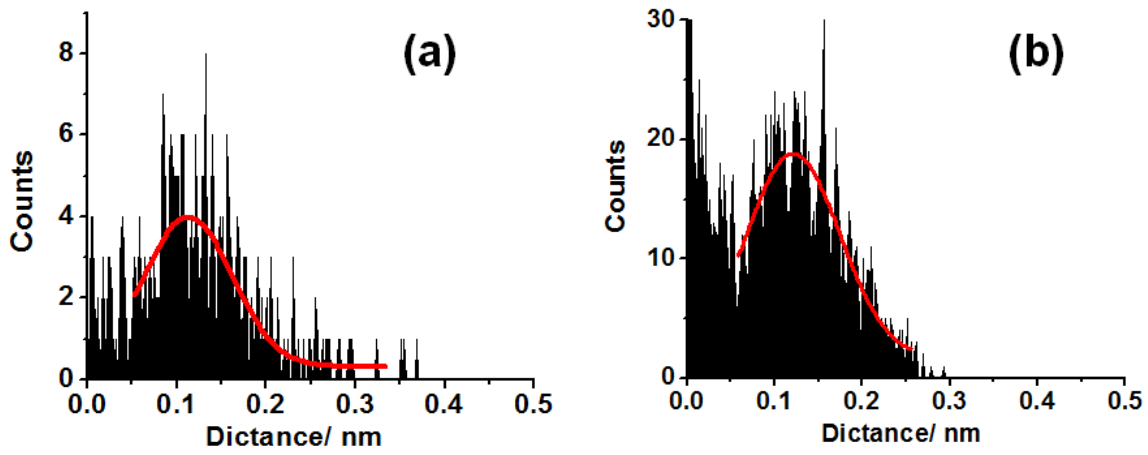


Figure 2.2 Step-length histograms of $A(CG)_3T$ measured (a) in the air and (b) in solution. The red curves show Gaussian fittings of the histogram peaks.

The conductance (or resistance) of DNA is related with both the molecular length and sequence. For $A(CG)_nT$ (n=3~7), the resistance increases linearly with the molecular length (Fig. 2.3a), which is expected for hopping transport.[106, 123, 124] According to the thermally activated sequential hopping model[125, 126], holes hop along a DNA molecule from one end to another, where the individual G bases act as hopping sites like stepping stones. As a result, the total resistance is proportional to the number of hopping sites (G bases), and thus the length of the molecule (see more discussions in section 2.7.6). When DNA is connected to two electrodes (tip and substrate), an additional contribution to the resistance arises from the two contacting part. The total resistance of the DNA is given by[125, 126]

$$R = R_c + R_h = R_c + (\mathrm{N}-1)R_{G\text{-}G}, \quad (2.1)$$

where R_c is contact resistance, R_h is intrinsic DNA resistance, N is number of base pairs and $R_{G\text{-}G}$ is resistance of a hopping step (one GC base pair). Table 2.2 summarizes the R_c and R_h of all the $A(CG)_nT$ sequences. By fitting the experimental data with Eq. 2.1, we resolved the contact resistance, R_c=0.48±0.16 MΩ, and the resistance of one step hopping, $R_{G\text{-}G}$=0.28±0.02 MΩ per GC base pair. Note that the contact resistance is small compared to the total resistance for $A(CG)_nT$ (See Table 2.2), suggesting efficient electronic coupling between the electrodes and the molecule, and the DNA resistance is dominated by the molecule itself, rather by the contact.

In contrast to the trend of $A(CG)_nT$ resistance described above, the length-dependence of $ACGC(AT)_mGCGT$ and $ACGC(AT)_{m-1}AGCGT$ resistance is significantly different (Fig. 2.3b). For m=0, 1 and 2, the resistance increases more sharply with length (L), and would be best fitted with an exponential function, rather than with a shallow linear dependence found for $A(CG)_nT$. For m>2, however, the resistance shows weaker length dependence, indicating a transition in the charge transport mechanism at m=2 (or 4 A-T base pairs). This observation agrees with previous photochemical and direct conductance measurements of DNA, which have demonstrated that inserting a short AT block in the middle of a GC sequence introduces a tunneling barrier, leading to an exponential increase in the DNA resistance with the AT block length[112-117], and inserting a longer AT block results in the transition in the charge transport mechanism from tunneling to hopping[112, 114]. The tunneling-hopping transition has also been predicted and analyzed by theoretical calculations[112-117]. See section 2.7.6 for further discussion.

Based on the above results, I modeled the $ACGC(AT)_mGCGT$ and $ACGC(AT)_{m-1}AGCGT$ resistance as a sum of three contribution parts, electrode-DNA contact, hopping via GC sequences, and tunneling via the AT block, given by $R=R_c+R_h+R_t$, where R_c is the contact resistance, R_h is the GC hopping resistance, and R_t is the AT tunneling resistance. Because both R_c and R_h are known from the $A(CG)_nT$ measurement, I'm able to determine the resistance of the inserted AT block, which is listed in Table 2.2. Semi-logarithmic plot of the AT block resistance (R_t) vs. the AT block length shows an exponential dependence, following $R_t=R_0\exp(\beta L)$, where R_0 is the contact resistance between the GC and AT block, and, β is decay constant and L is the AT block length (Fig. 2.3c). Fitting the experimental data with the above exponential relation leads to a β of 2.03 ± 0.12 nm^{-1} (Fig. 2.3c). This decay constant is smaller than ~4 nm^{-1} reported by Xu et al.[113] for thiolated DNA molecules, but is within the range reported by various other works[59, 107-111] and consistent with the calculations by Torisi et al.[117] and Voityuk et al.[127] for dsDNA with alternating AT sequences.

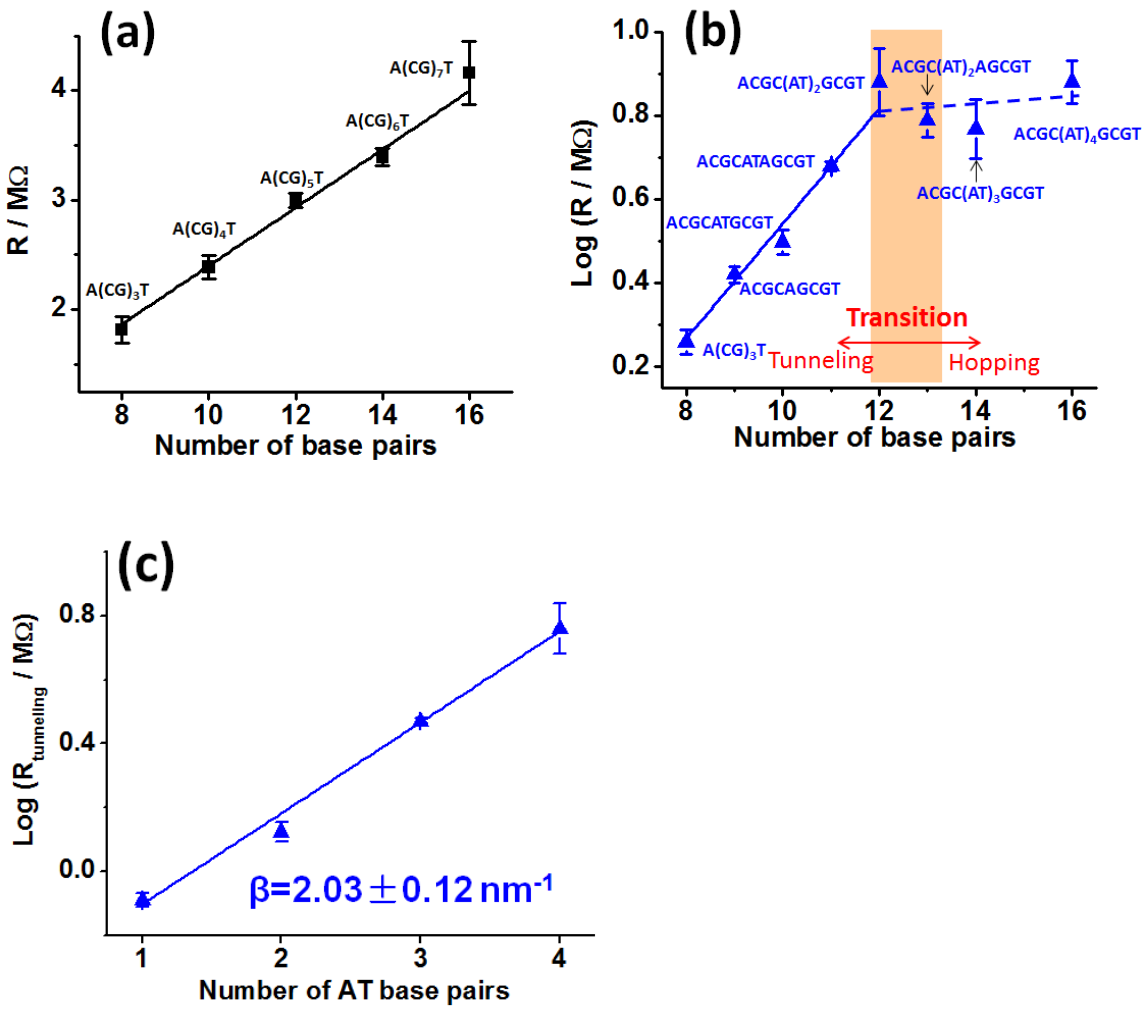


Figure 2.3 DNA Resistance vs. molecular length for (a) $A(CG)_nT$ (n=3~7) (b) $ACGC(AT)_mGCGT$ (m=0~4) and $ACGC(AT)_{m-1}AGCGT$ (m=1~3) sequences, and (c) the AT blocks ($(AT)_m$ and $(AT)_{m-1}A$) in $ACGC(AT)_mGCGT$ and $ACGC(AT)_{m-1}AGCGT$ sequences. The solid lines in (a), (b) and (c) are linear fits to the data, and the dashed line in (b) is a guide to eye. The transition from tunneling to hopping occurs the AT block is longer than 4 base pairs, which is markers with a shaded orange region.

Table 2.2 Conductance and Seebeck Coefficients of DNA With Different Sequences

Sequence	Conductance peak position ($\log(G/G_0)$) *	Conductance peak width	Resistance (MΩ)	R_c (MΩ)#	R_h (MΩ)#	R_t (MΩ)#	Seebeck coefficient ($\mu V\ K^{-1}$)
A(CG)$_3$T	-2.17±0.03	0.20	1.9±0.1	0.48	1.40	NA	1.4±0.2
A(CG)$_4$T	-2.27±0.02	0.18	2.4±0.1	0.48	1.96	NA	0.8±0.2
A(CG)$_5$T	-2.37±0.01	0.17	3.0±0.1	0.48	2.52	NA	1.0±0.2
A(CG)$_6$T	-2.42±0.01	0.18	3.4±0.1	0.48	3.08	NA	0.6±0.2
A(CG)$_7$T	-2.51±0.03	0.20	4.2±0.3	0.48	3.64	NA	0.8±0.2
ACGCAGCGT	-2.31±0.02	0.25	2.6±0.1	0.48	1.12	1.0	5.0±0.3
ACGCATGCGT	-2.36±0.03	0.35	3.0±0.2	0.48	1.12	1.4	5.9±0.4
ACGCATAGCGT	-2.57±0.01	0.30	4.8±0.1	0.48	1.12	3.2	6.5±0.8
ACGC(AT)$_2$GCGT	-2.76±0.08	0.30	7.4±1.4	0.48	1.12	5.8	7.9±0.5
ACGC(AT)$_2$AGCGT	-2.68±0.04	0.50	6.1±0.6	0.48	1.12	4.5	4.9±0.2
ACGC(AT)$_3$GCGT	-2.65±0.07	0.52	5.8±0.9	0.48	1.12	4.2	2.0±0.2
ACGC(AT)$_4$GCGT	-2.77±0.05	0.40	7.6±0.9	0.48	1.12	6.0	2.0±0.3

*: G_0 ($=2e^2/h=$ 77.48 μS) is the conductance quantum.

#: R_c, R_h and R_t are the contact resistance, hopping part resistance (CG sequences) and tunneling part (AT sequences) resistance, respectively.

2.5 Thermoelectric Effect in Single DNA Molecules

The thermoelectric effect of a single DNA-electrode junction can be described by

$$S_{junction} = S_{Au} - \frac{\Delta U_{TE,m}}{\Delta T} = S_{Au} - \frac{-\Delta(I_{TE,m} / G_m)}{\Delta T}, \qquad (2.2)$$

where S_{Au} is the Seebeck coefficient of gold (~2 μV K^{-1} [128]), $U_{TE,m}$ is the open circuit voltage, $I_{TE,m}$ is the short circuit current, G_m is the conductance of the molecular junction, and ΔT is the temperature difference between the STM tip and substrate electrodes. I measured the thermoelectric effect by keeping the tip at 295 K while cooling the substrate from 295 to 275 K.[30] This temperature range is selected to ensure that all the dsDNA sequences are structurally stable, and their resistance does not change significantly with temperature[129].

I started the thermoelectric effect measurement by detecting plateaus in the conductance traces during the retraction of the STM tip from the substrate (Fig. 2.4a). Once a plateau was detected, I halted the tip retraction and swept the bias voltage between the tip and substrate electrodes over ±10 mV to obtain a current (I)-voltage (V) characteristic curve. After recording an I-V curve, I further retracted the tip to a new position, and repeated the I-V measurement until the molecular junction broke down. Fig. 2.4b shows several I-V curves for $ACGC(AT)_2GCGT$ measured at different locations of a

conductance plateau, where the colors of curves match the colors of the dots marked on the conductance plateau shown in Fig. 2.4a. These I-V curves are linear within the bias range.

From the I-V characteristics I obtained the average Seebeck coefficient of a DNA molecule with the following procedure. First, I fitted each I-V curve with a linear function to obtain G, and then obtained a corresponding I/G-V curve by dividing I by G. From thousands of I/G-V curves, I constructed a 2-dimensional I/G-V histogram for each temperature difference (Figs. 2.4c and 2.4d). When the substrate is held at the same temperature as the tip ($\Delta T=0$), the center of the histogram passes through the origin of I/G-V plot (Fig. 2.4c). In contrast, when the substrate is cooled below the tip temperature, there is an offset in the histogram in the I/G-V plot, due to the thermoelectric effect (Fig. 2.4d). By extracting the voltage offsets (at zero current) from the I/G-V histograms, I constructed the thermoelectric voltage histograms at different tip-substrate temperature differences (Fig. 2.4e, Fig 2.5 and Fig 2.6). The peak in each thermoelectric voltage histogram was fitted with a Gaussian distribution, from which $U_{TE,m}$ was determined. Fig. 2.4f shows that $U_{TE,m}$ depends linearly on ΔT, and $S_{junction}$ can be determined by the slope according to Eq. 2.2.

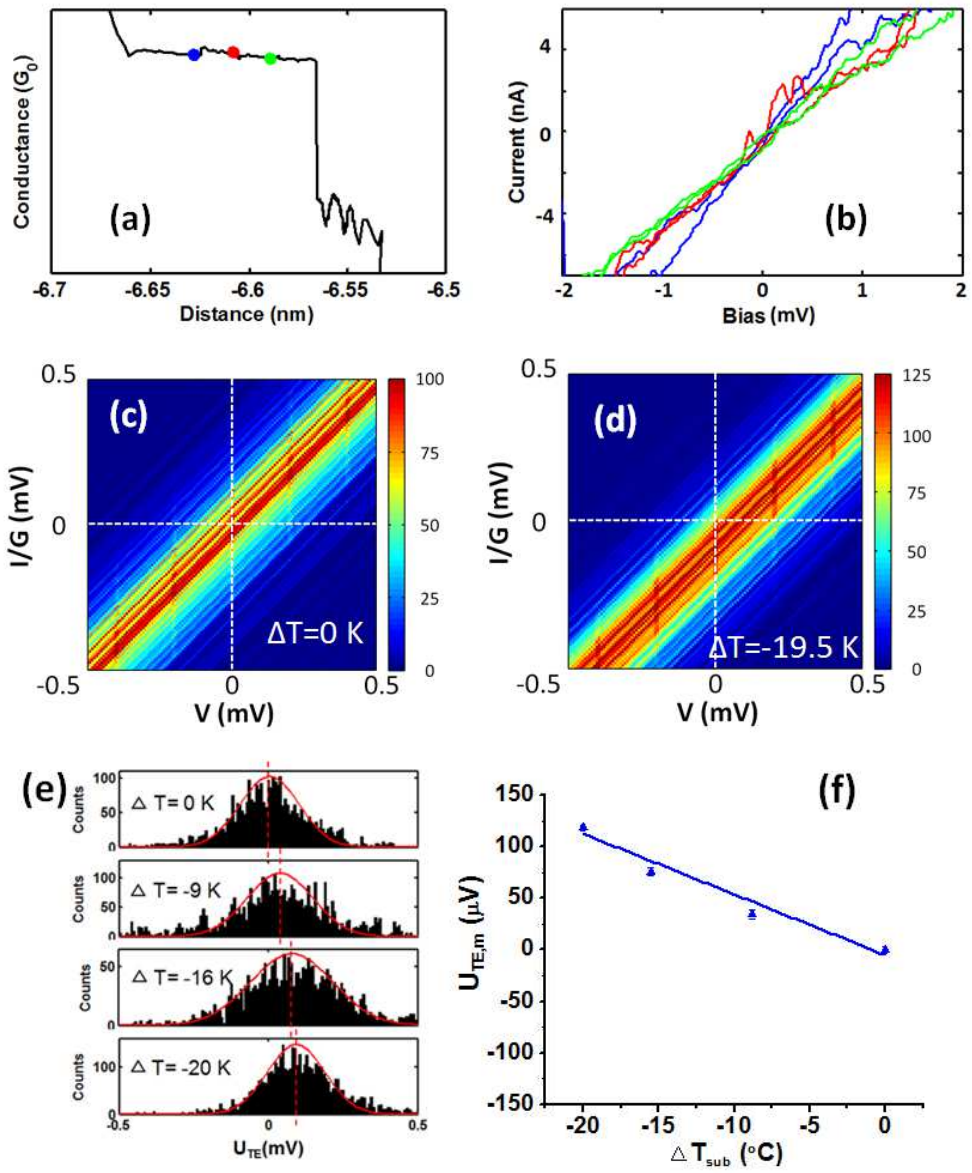
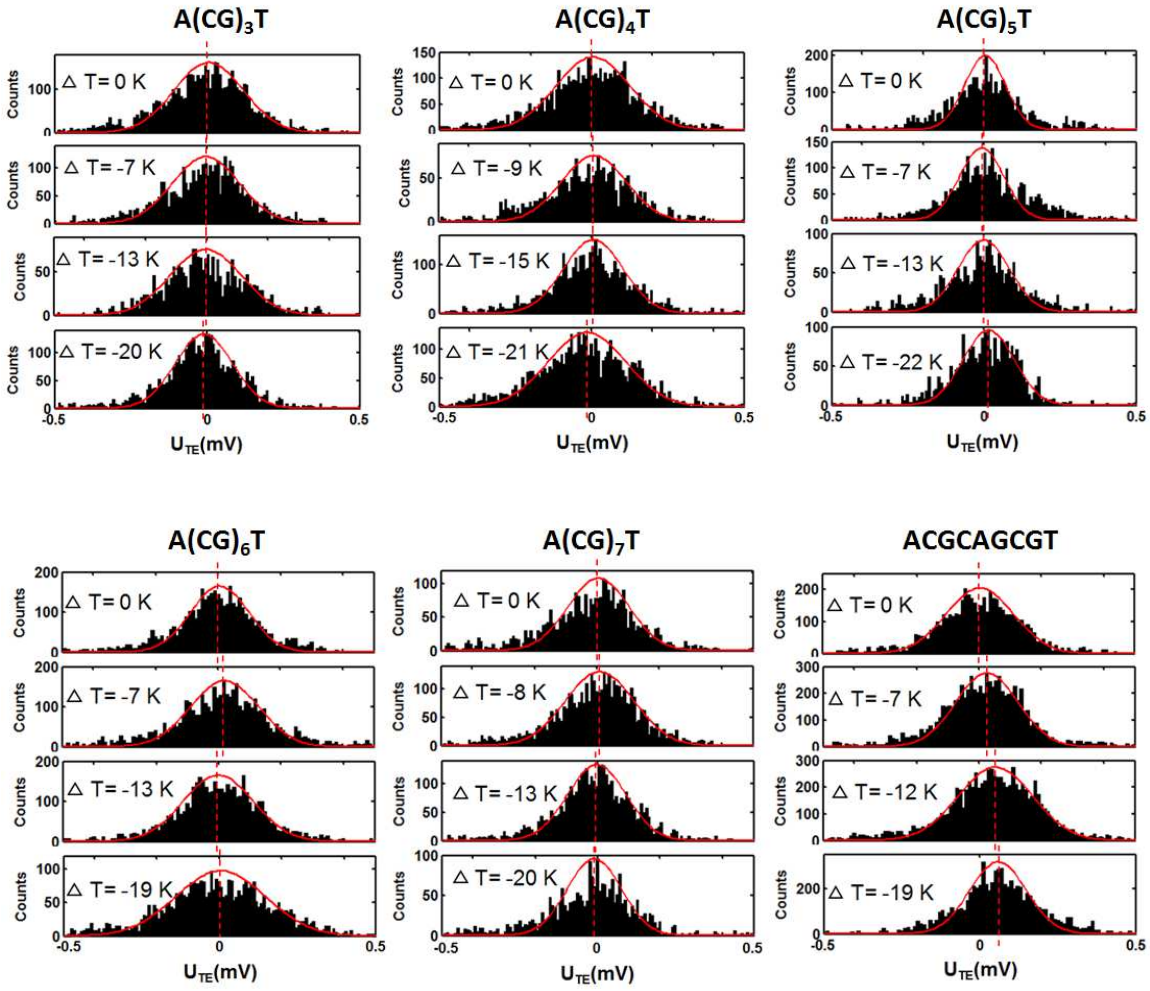


Figure 2.4 Thermoelectric measurement of DNA. (a) Semi-logarithmic plot of conductance-distance trace (the colored dots mark where *I-V* curves are measured). (b) Individual *I-V* curves measured at the locations marked with corresponding color in a. (c) *I/G-V* histogram at ΔT=0 K. (d) *I/G-V* histogram at ΔT=19.5 K, showing an offset due to the thermoelectric effect. (e) Thermal voltage histogram, where the red curves show

Gaussian fits. (f) Thermoelectric voltage vs. ΔT, where the straight line is linear fit to the data, and error bars are fitting errors. DNA sequence: ACGC$(AT)_2$GCGT.



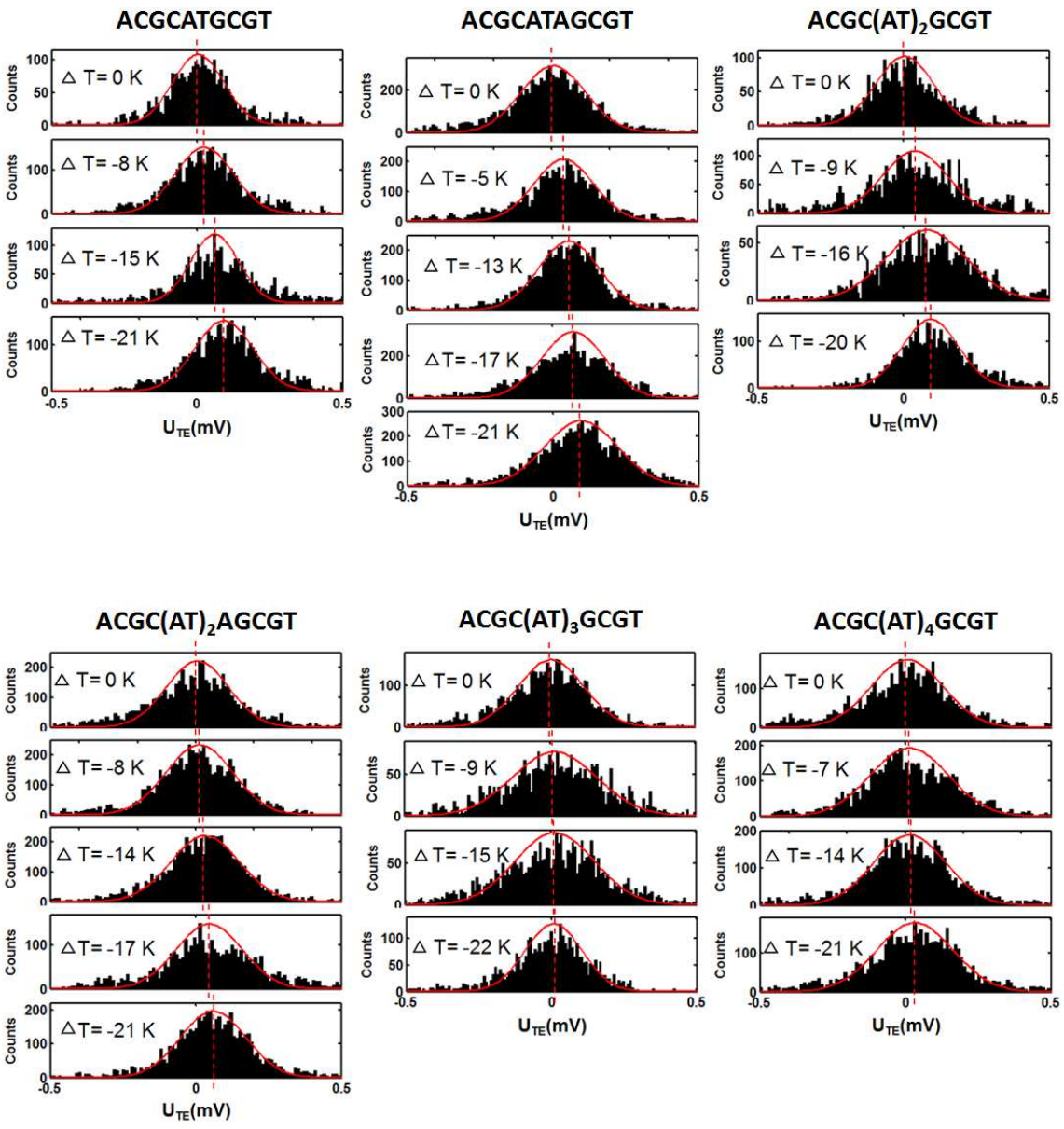


Figure 2.5 Thermal voltage histograms for double helical DNA collected at different temperature gradients. The red curves are Gaussian fitting of the voltage histogram peaks, and the dash lines indicate the peak positions.

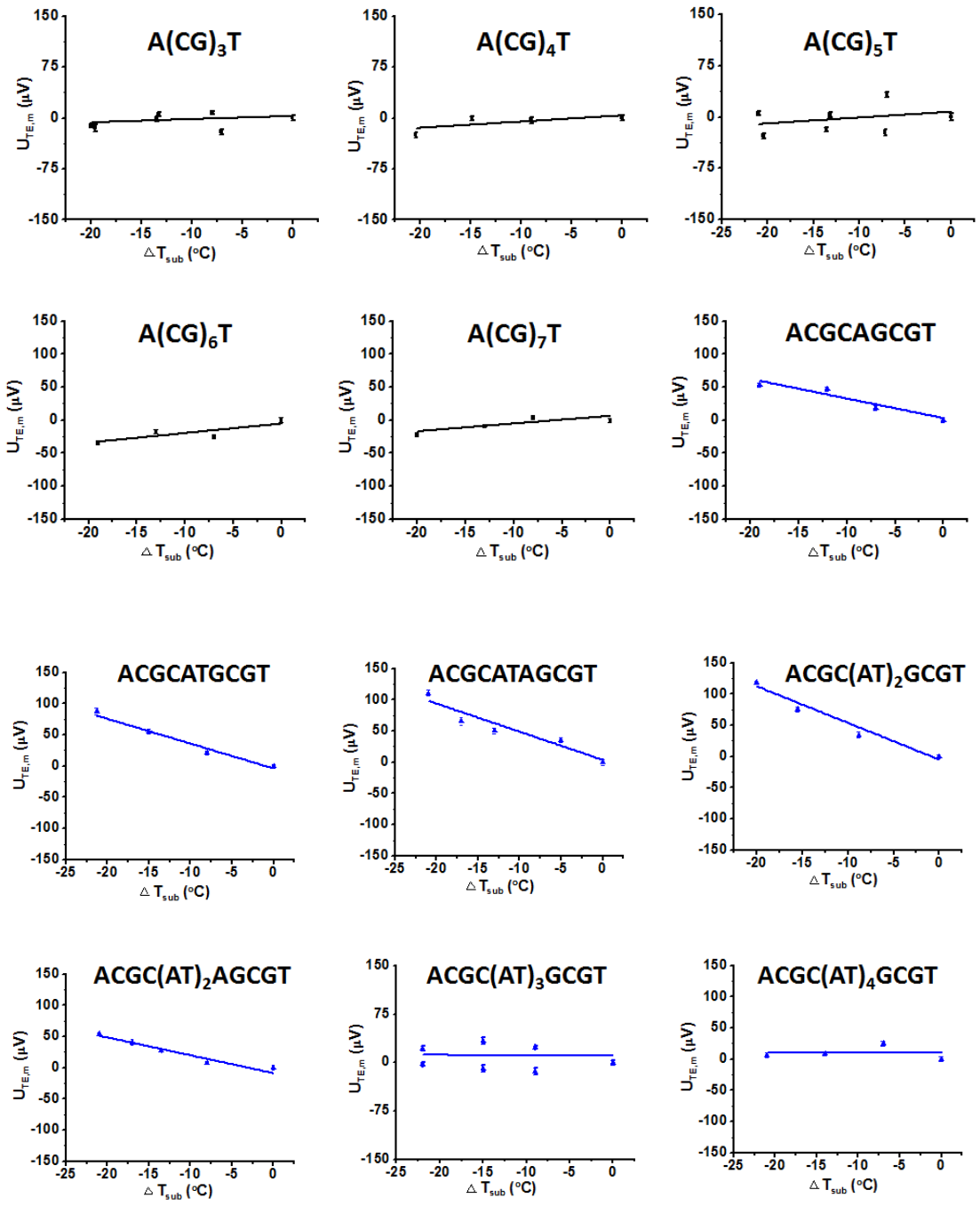


Figure 2.6 Linear fitting of the thermoelectric voltage data at different temperature gradients for $A(CG)_nT$ (n=3~7), $ACGC(AT)_mGCGT$ (m=1~4), and $ACGC(AT)_{m-1}AGCGT$ (m=1~3) sequences.

Fig. 2.7 summarizes the Seebeck coefficients of DNA with different lengths and sequences, from which several important conclusions can be drawn. First, the Seebeck coefficients are positive for all the DNA studied here. It has been explained in section 1.6 that a positive Seebeck coefficient corresponds to hole-dominated charge transport, and a negative Seebeck coefficient signals electron-dominated charge transport[28]. The observation of positive Seebeck coefficients here shows that holes dominate charge transport in DNA. This is as expected because DNA HOMO level is close to the electrode Fermi level compared to its LUMO level, and is also consistent with previous experiments[112, 114, 116, 117, 130]. Nevertheless, the prediction of the Seebeck coefficient sign is based on a coherent tunneling model, which is not necessarily applicable to hopping transport. The data indicate that this prediction appears to be valid also in the hopping regime. Second, the Seebeck coefficients of DNA in the hopping regime (in $A(CG)_nT$) are small, and weakly depend on the molecular length compared to other organic molecules[131, 132]. Last, inserting a short AT block (shorter than 5 AT base pairs) into the middle of $A(CG)_nT$ leads to a much greater Seebeck coefficient, and it increases with the AT block length. However, when the AT block is longer than 5 AT base pairs, the Seebeck coefficient drops to the level of $A(CG)_nT$, and become insensitive to the AT length. This transition coincides with the tunneling-hopping transition near 4-5 AT base pairs observed from the conductance measurement, which strongly suggests that the thermoelectric effect is large in the tunneling regime and small in the hopping regime.

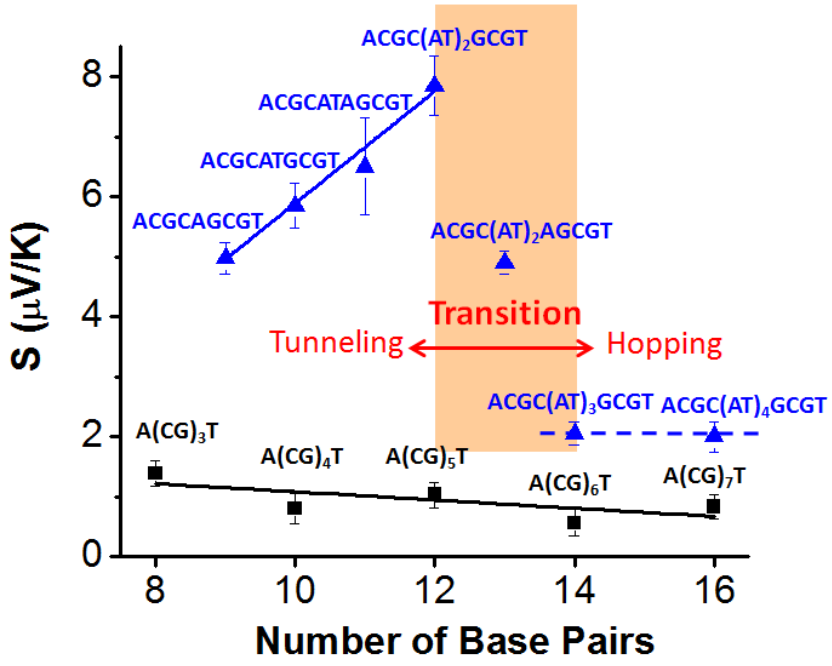


Figure 2.7 Seebeck coefficients of DNA with different molecular lengths and sequences. The black squares are the Seebeck coefficients of $A(CG)_nT$ (n=1, 2, 3). The blue triangles are the Seebeck coefficients of $ACGC(AT)_mGCGT$ (m=1~4) and $ACGC(AT)_{m-1}AGCGT$ (m=1~3) sequences, showing a transition when the AT block length is longer than 4 base pairs. The solid and dashed lines are guides to eye.

2.6 Theoretical Analysis

The Seebeck coefficient for bulk materials can be expressed by the Mott formula[133],

$$S = \frac{\pi^2 k_B^2 T}{3e} \cdot \left(\frac{1}{R} \cdot \frac{\partial R}{\partial E} \right)_{E=E_F}, \quad (2.3)$$

where R is the energy dependent resistance function, and E is the energy of the carriers. k_B is Boltzmann constant, T is temperature and e is elementary charge. The Mott formula assumes incoherent transport, which is applicable to hopping transport in DNA. For coherent tunneling transport, the Seebeck coefficient can be obtained with Landauer's formula, which leads to a similar expression as Eq. 2.3 except that R is replaced by the energy dependent transmission probability function. [103, 134.]

Assume that the resistance function, *R(E),* can be expressed as a sum of the contact and hopping resistance functions (Eq. 2.1), which is modeled as Fig. 2.8a, the experimental thermoelectric effect in the hopping regime can be analyzed with Eq. 2,3. The resulting overall Seebeck coefficient (S) consists of contributions from the molecule-electrode contact (S_c) and hopping along the dsDNA sequences (S_h), given by

$$S[\mathrm{A(CG)_nT}] = \frac{R_c}{R} S_c + \frac{R_h}{R} S_h, \quad (2.4)$$

where R, R_c and R_h in Eq. 2.4 are the total resistance, contact resistance and DNA resistance, respectively. We discuss the validity of the assumption, and derivation of Eq. 2.4 in section 2.7.7. Both R_c and R_h are known from the linear fitting to the experimental data shown in Fig. 2.3a (See Table 2.2).

In the case of $\mathrm{ACGC(AT)_mGCGT}$ and $\mathrm{ACGC(AT)_{m-1}AGCGT}$ sequences, the total resistance R[AT] includes another contribution, R_t, arising from the inserted AT block in

the middle of the GC sequence, as shown in Fig. 2.8b. The overall Seebeck coefficient of the DNA junction should also include the contribution from the inserted AT block, described by,

$$S[\mathrm{AT}] = \frac{R_c}{R} S_c + \frac{R_h}{R} S_h + \frac{R_t}{R} S_t, \quad (2.5)$$

where S_t is Seebeck coefficient of the inserted AT part.

In Eq.2.4, although R_h is proportional to the molecular length, S_h is independent of the length in that it is proportional to the relative change in R_h (a normalized quantity). S_c is independent of the molecular length, too. Therefore, we conclude that the molecular length dependence of the overall Seebeck coefficient, S, arises from R in Eq. 2.4, which as shown in Fig. 2.3a is weakly dependent on molecular length. By fitting the measured Seebeck coefficients times R with R_h at different lengths (Fig. 2.8c), I obtained the slope, S_h=0.1±0.3 μV K^{-1}, and from the intercept we found that S_c=4.8±1.7 μV K^{-1}, showing that the contact plays a dominant role in the thermoelectric effect of $A(CG)_nT$. The above model explains the weak length dependence of the observed thermoelectric effect for $A(CG)_nT$.

For Eq. 2.5, I plotted S^*R vs. R_t (Table 2.2) in Fig. 2.8d for short AT blocks (m=1-2), which follows a linear function. According to Eq. 2.5, the slope of the linear relation is S_t, from which I found that S_t=8.9±1.4 μV K^{-1}. For longer AT blocks (m>2), I determined S_t

from Eq.2.5 (Table 2.3). Compared to the short AT blocks, these longer sequences have smaller Seebeck coefficients (~2 μV K^{-1}).

To further understand the tunneling Seebeck coefficient, S_t, from the AT block, I express the transmission function of the tunneling barrier with a Lorentzian distribution by,[131, 132, 135, 136]

$$\tau(E) = \frac{4\Gamma^2}{4\Gamma^2 + \Delta E_H{}^2}, \quad (2.6)$$

where Γ is the width of the HOMO level of the AT block and ΔE_H is the energy difference between the AT block and GC HOMO levels. Using the above transmission function, the contributions of the AT block to the resistance and Seebeck coefficient are described as

$$\frac{1}{R_t} = G_0 \frac{4\Gamma^2}{4\Gamma^2 + \Delta E_H{}^2}, \quad (2.7)$$

$$S_t = \frac{\pi^2 k_B^2 T}{3e} \cdot \frac{2\Delta E_H}{4\Gamma^2 + \Delta E_H{}^2}. \quad (2.8)$$

By fitting the experimental data with Eqs. 2.7 and 2.8, I obtained Γ and ΔE_H (Table 2.3), which shows that $\Gamma << \Delta E_H$, indicating a weak coupling between the AT block and the GC sequences and electrodes. In this weak coupling limit, S_t is proportional to $1/\Delta E_H$.[135, 137] Because the electronic coupling between alternating AT base pairs in the AT block is weak,[127] and ΔE_H is expected to be weakly dependent on the AT block length, which explains the constant slope (S_t) in Fig. 2.8d.

The expression of Seebeck coefficient of molecular junction (Eq. 2.3) suggests that Seebeck coefficient is correlated with the slope of transmission function at Fermi level of electrodes, which is determined by the molecule's HOMO and LUMO levels, the coupling between the molecule and electrodes, and the Fermi level of electrodes. Therefore, we should realize that the Seebeck coefficient of the molecular junction is more than a quantify of the thermoelectric power of the molecule itself, but an overall effect comes from the interplay between the molecule and electrodes. Each part can potentially induce a substantial difference in the measured Seebeck coefficient.

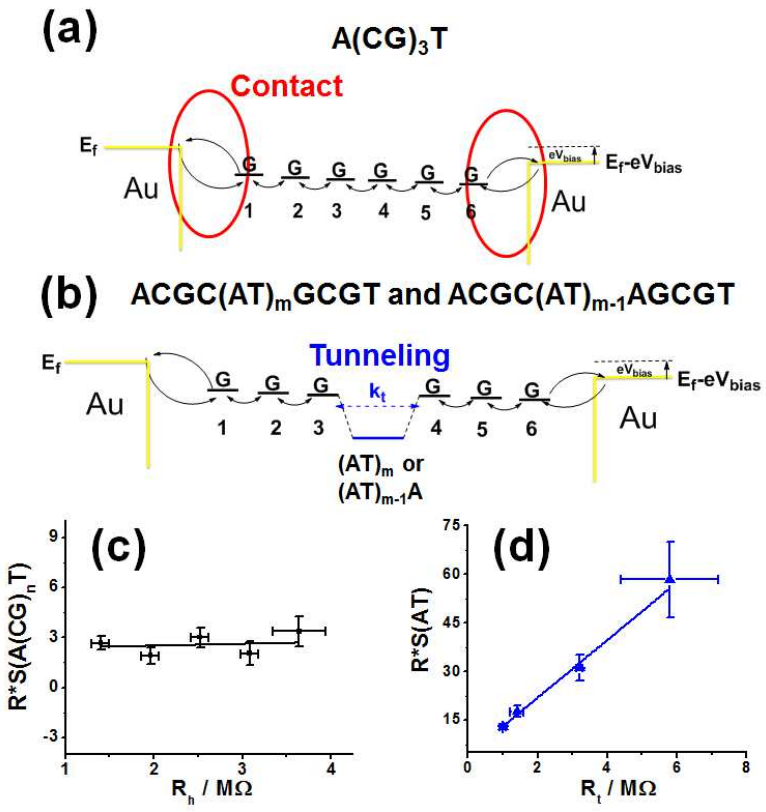


Figure 2.8 Thermoelectric effect in DNA in terms of tunneling and hopping models. (a) Charge transport in $A(CG)_nT$, where a hole is injected from left electrode into the first G,

then hops along the molecule with each G as a hopping site, and eventually reaches the right electrode. The charge transfer rates at the contacts (red part) are energy-dependent, which is a dominant contribution to the Seebeck coefficient. (b) Charge transport in $ACGC(AT)_mGCGT$ and $ACGC(AT)_{m-1}AGCGT$, where a tunneling barrier (marked blue) arises from the AT block. (c) $R*S$ vs. R_h for $A(CG)_nT$ sequences. (d) $R*S$ vs. R_t for $ACGC(AT)_mGCGT$ and $ACGC(AT)_{m-1}AGCGT$ (m=1 and 2). Solid lines in (c) and (d) are linear fits to the data.

Table 2.3 The Resistance (R_t) and the Seebeck Coefficients (S_t) of the AT Blocks.

Sequences	R_t/MΩ	S_t(μV K^{-1})	Γ/eV	ΔE_H/eV
ACGCAGCGT	1.0±0.3	8.9±1.4	0.07±0.02	1.3±0.4
ACGCATGCGT	1.4±0.4	8.9±1.4	0.06 ±0.02	1.3±0.4
ACGCATAGCGT	3.2±0.3	8.9±1.4	0.05±0.01	1.6±0.3
$ACGC(AT)_2GCGT$	5.8±1.6	8.9±1.4	0.03±0.01	1.4±0.5
$ACGC(AT)_2AGCGT$	4.5±0.8	6.1±1.3	NA	NA
$ACGC(AT)_3GCGT$	4.2±1.1	2.2±0.8	NA	NA
$ACGC(AT)_4GCGT$	6.0±1.1	2.1±0.7	NA	NA

∗ Γ is the broadening of the HOMO levels, and ΔE_H is the energy difference between the HOMO levels of AT and GC blocks.

Though the above hopping and tunneling models help understand the length dependence of the Seebeck coefficients in DNA, a model including sufficient chemical and structural details of dsDNA is needed to explain that the insertion of a short AT block

increases the Seebeck coefficient. We used an extended Su-Schrieffer-Heeger model with the Lennard-Jones potential to describe the dsDNA.

A theory that treats electron-phonon coupling in the strong coupling regime has been developed to calculate DNA conductance[138]. The theory has been recently extended to determine the Seebeck coefficient in conducting polymers[139]. While the strong coupling theory is useful in predicting qualitative trends of molecular conductance and thermoelectric effect, it cannot include chemical details in the calculations easily. In this respect, the weak coupling theory is more suitable. Previously, the weak coupling theory has been used to explain the tunneling-hopping transition in single oligomers,[140] and to determine other charge transport properties, such as the electric current noise in molecular junctions[141]. In this work, we applied the weak coupling theory to examine the length and sequence dependence of the DNA Seebeck coefficient (See section 2.7.8 for more details). The theory reproduces sequence dependence, and also the observed large increase in the Seebeck coefficient associated with the insertion of an AT block in the middle of CG sequences. The increase can be attributed to the difference in the site energies between AT and GC base pairs. However, we emphasized that the calculation was performed at 8 K, where the theory cannot provide quantitative agreement with the experimental Seebeck coefficient, and nor it predicts the transition from tunneling to hopping. Further investigation is still needed to quantitatively describe the measured Seebeck coefficients, and the tunneling-hopping transition.

2.7 Other Supporting Data and Discussions

2.7.1 Gel electrophoretic characterization of dsDNA

Nondenaturing polyacrylamide gel electrophoresis was performed to confirm the formation of double helical DNA molecules. In the electrophoretic measurement, a voltage of 200 V was applied to 50 pmol of each sample with 10% nondenaturing PAGE gels in 1×TAE Mg^{2+} buffer at 22 °C for 3 hrs. The resulting ethidium bromide (EB) stained gels were scanned in a Biorad Gel Doc XR+ system for visualization. DNA samples included 5'-A$(CG)_n$T-3' (n=3~7), 5'-ACGC$(AT)_m$GCGT-3' (m=1~4), and 5'-ACGC$(AT)_{m-1}$AGCGT-3' (m=1~3) sequences. These DNA samples were dissolved in phosphate buffer (5 mM, pH=7). The annealing program consisted of holding the temperature at 95 °C for 5 mins, cooling from 95 °C to 90 °C at the rate of 4 °C per second, cooling from 90 °C to 76 °C at a rate of 1 °C per 5 mins, further cooling from 76 °C to 26 °C at a rate of 1 °C per 15 mins, holding at 25 °C for 30 mins, then maintained at 4 °C. This stepwise annealing process helped prevent the formation of ssDNA hairpin structures. Section 2.7.1 summarizes the electrophoresis gel data for all sequences, which shows one major band for each sequence. For longer sequences, ACGC$(AT)_3$GCGT, ACGC$(AT)_2$AGCGT, and ACGC$(AT)_4$GCGT, the electrophoresis indicated a small amount of hairpin structures in the sample. These hairpin structures were formed from single DNA strands, consisting of only one amine linker in each structure, and could not form molecular junctions in the STM break junction experiments. The electrophoresis also revealed a minor band close to the major band of

ACGC(AT)$_2$AGCGT (and ACGC(AT)$_4$GCGT), which was due to the protected amine group in some DNA molecules could not be deprotected (Glen Research http://www.glenresearch.com/ProductFiles/Product.php?item=10-1037). Molecules with protected amine linkers could not form molecular junctions in the STM break junction experiments.

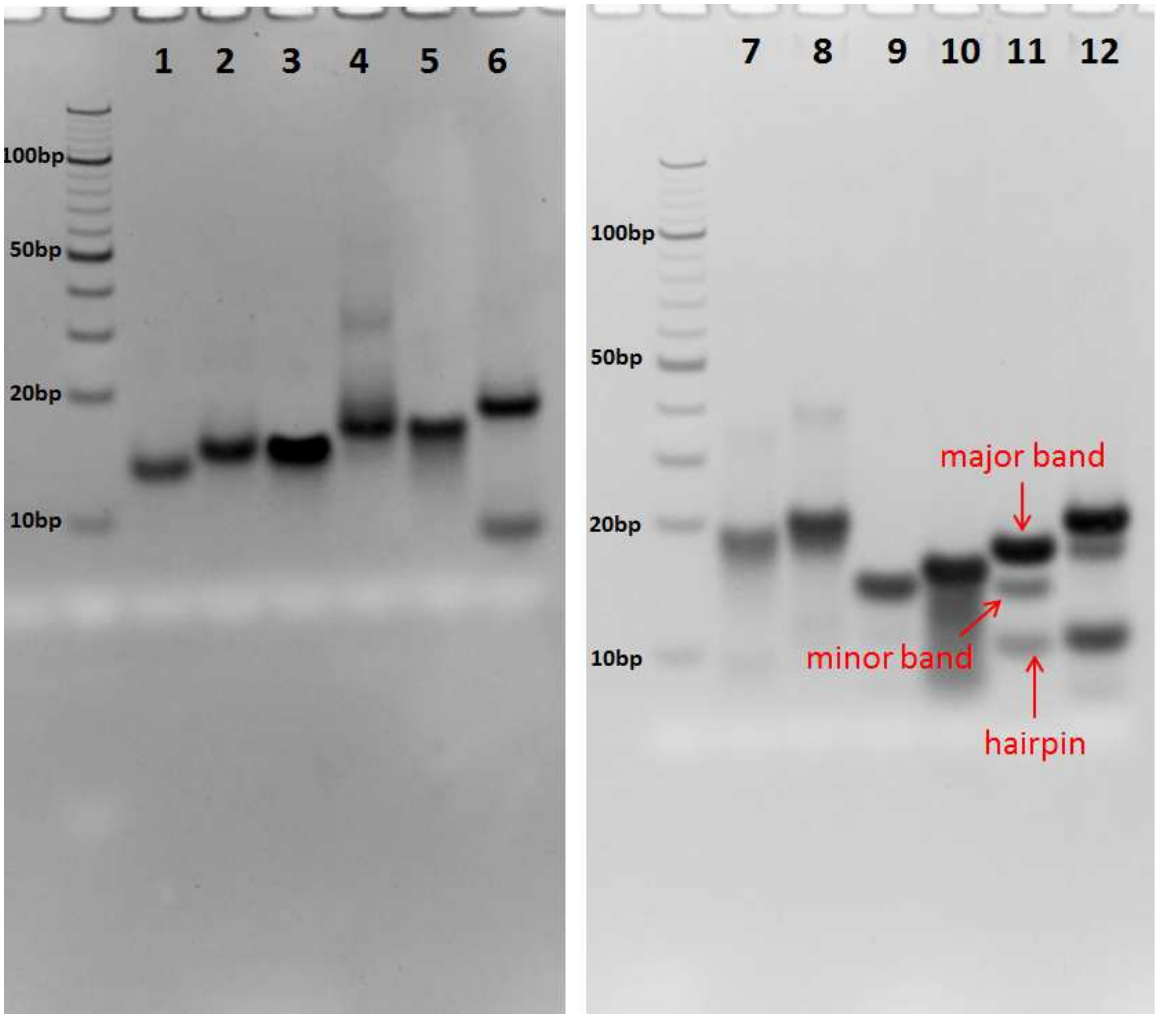


Figure 2.9 Gel electrophoresis of dsDNA samples after a programed annealing process. The samples from 1 to 12 are A(CG)$_3$T, A(CG)$_4$T, ACGCATGCGT, A(CG)$_5$T,

$ACGC(AT)_2GCGT$, $ACGC(AT)_3GCGT$, $A(CG)_6T$, $A(CG)_7T$, ACGCAGCGT, ACGCATAGCGT, $ACGC(AT)_2AGCGT$, and $ACGC(AT)_4GCGT$ with their complementary sequences, respectively. Weak bands due to hairpin formation and protected amine linker appear in $ACGC(AT)_3GCGT$, $ACGC(AT)_2AGCGT$, and $ACGC(AT)_4GCGT$.

2.7.2 Circular dichroism (CD) measurements

CD measurements were carried out on Jasco (Easton, MD) J-1710 Spectropolarimeter for 10 uM dsDNA in phosphate buffer (5 mM phosphate buffer, pH=7). Data shown in Fig. 2.10 were average over five scans, collected from 320 nm to 200 nm or 220 nm with a scanning rate of 100 nm min^{-1}. The positive band at around 275 nm and negative band at around 245 nm indicate a typical B-form structure for all the DNA sequences.

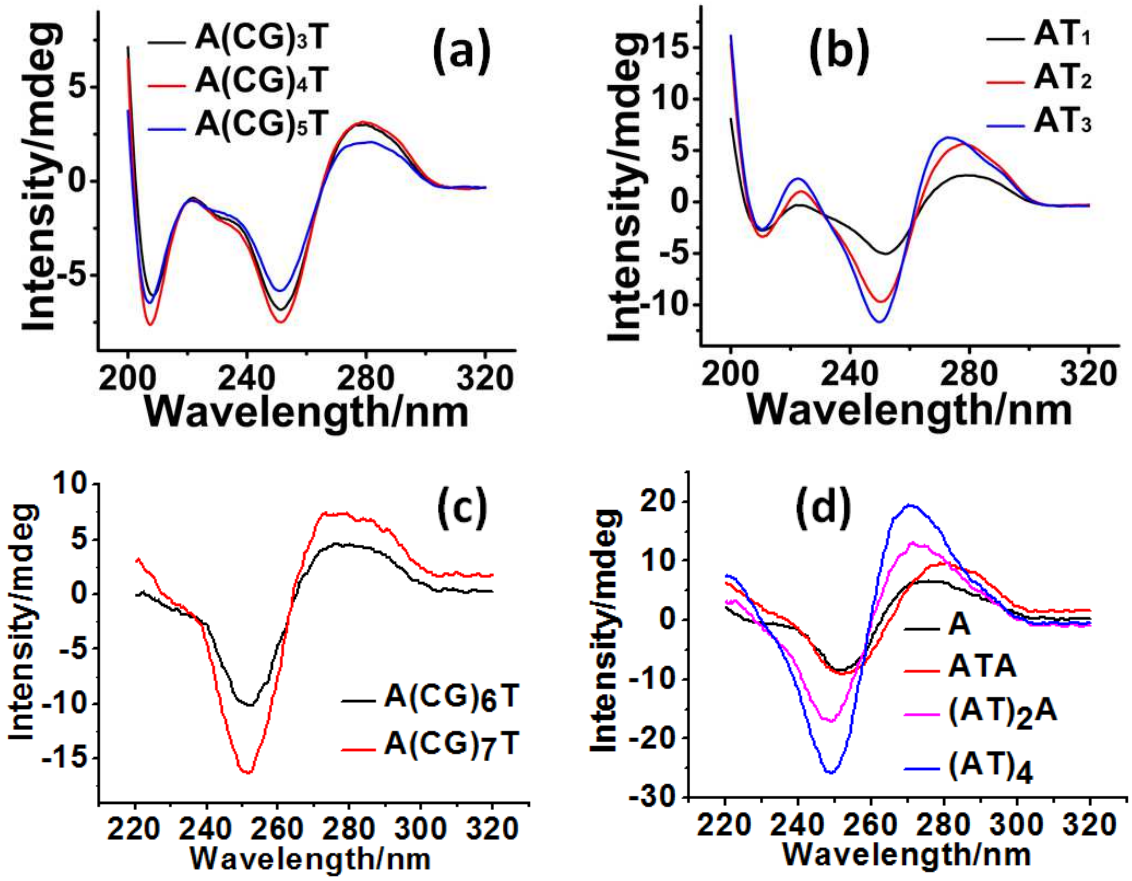


Figure 2.10 Circular dichroism data of (a) $A(CG)_nT$ (n=3~5), (b) $ACGC(AT)_mGCGT$ (m=1~3), (c) $A(CG)_nT$ (n=6,7), (d) $ACGC(AT)_{m-1}AGCGT$ (m=1~3) and $ACGC(AT)_mGCGT$ (m=4).

2.7.3 Melting temperature

Melting temperature experiment was carried out in a Varian Cary 300 Bio UV spectrophotometer with a Peltier thermal controller to determine melting temperature. 5-

μM dsDNA samples were prepared by annealing in 5 mM sodium phosphate buffer, and then heated at a rate of 0.2 K min^{-1} from 283 K (10 °C) to 353 K (80 °C) with the absorbance at 260 nm recorded in 60 s intervals. $A(CG)_3T$ (Fig. 2.11) is the shortest sequence measured in this work, which has the lowest melting temperature. The melting curve (black curve) was fitted to a two-state thermodynamic model (red curve), giving a melting temperature of 311±6 K (38 °C), well above the experimental temperature of 295 K (22 °C) for the shortest sequence.

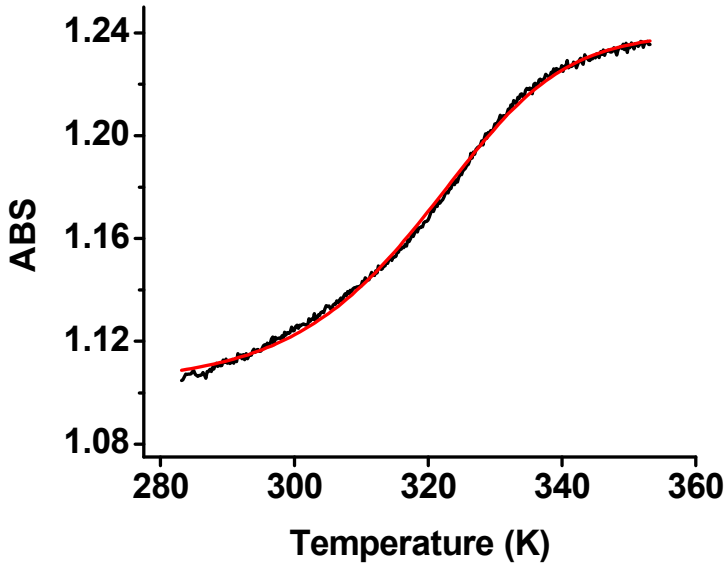


Figure 2.11 Melting temperature absorption curve for $A(CG)_3T$ (black curve), and two-state thermodynamic model fitting (red curve).

2.7.4 Conductance histograms of dsDNA measured in 20% humidified air

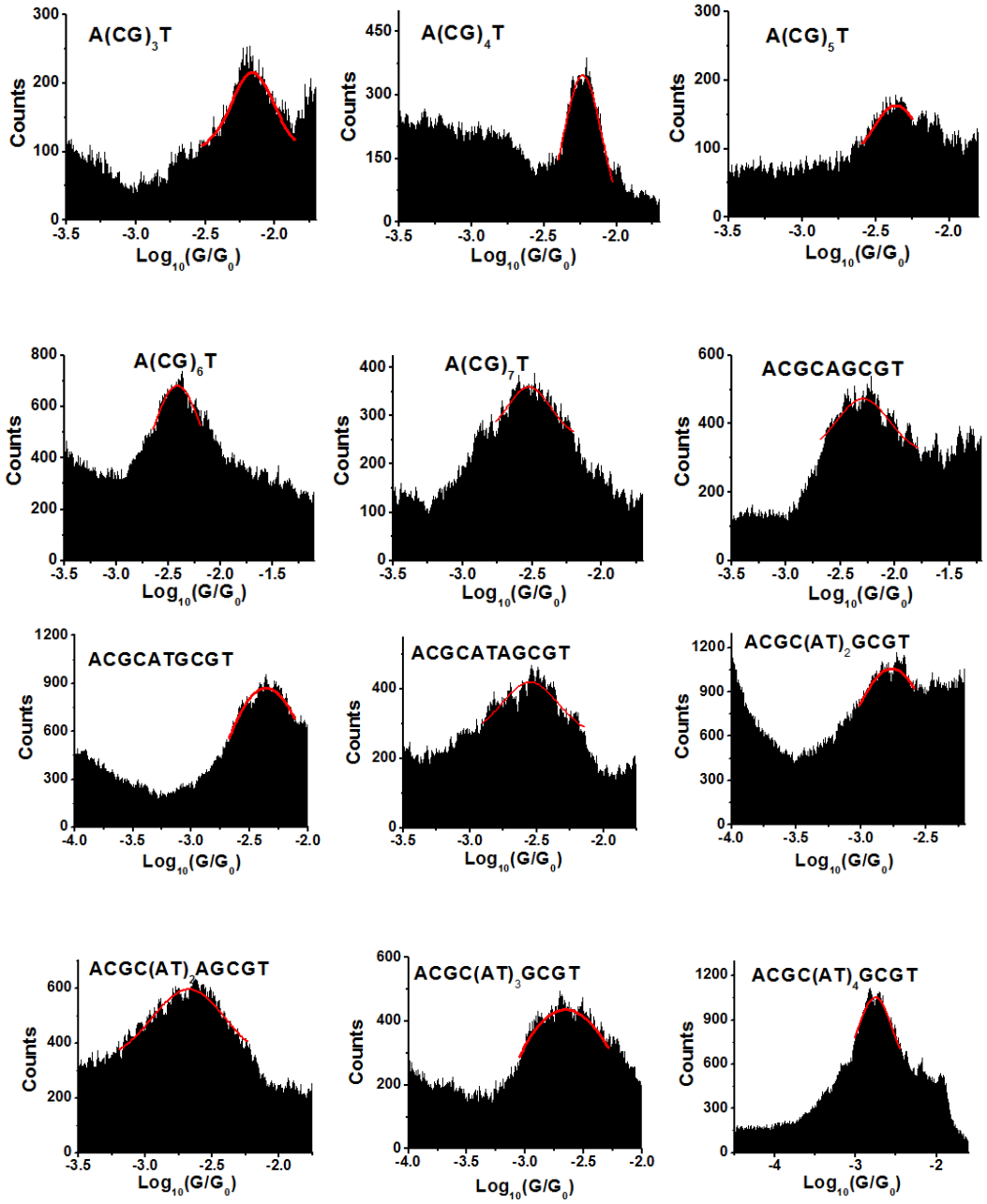


Figure 2.12 Conductance histograms of dsDNA measured in humidified air. Red curves are Gaussian fittings to the conductance peaks.

2.7.5 Conductance histograms of ds DNA in 5 mM phosphate buffer

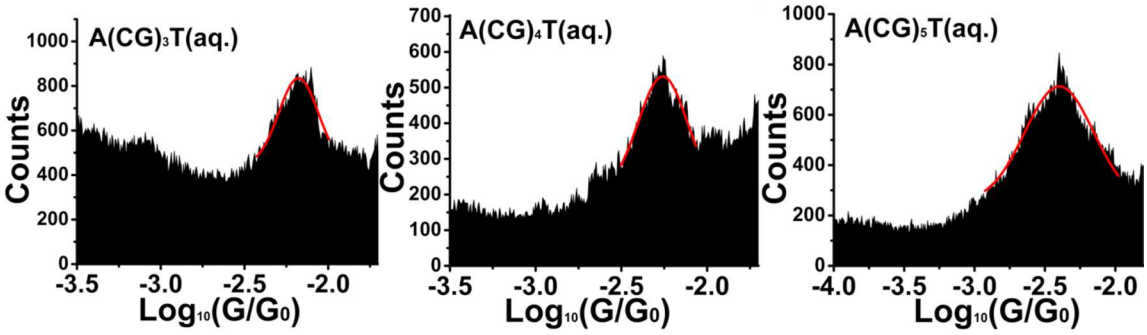


Figure 2.13 Conductance histograms of dsDNA measured in solution. Red curves are Gaussian fittings of the conductance peaks.

2.7.6 Molecular length dependence of DNA resistance

The resistance of $A(CG)_nT$ sequences is weakly length dependent, which can be fitted with a linear relation (Fig. 2.14a). Plotting the same data in a logarithmic scale shows a roughly linear behavior with the reception of the first data point (Fig. 2.14b). This is not surprising because an exponential function, $R=R_0\exp(-\beta L)$, can be expressed as linear as $R\sim R0(1-\beta L)$, for small βL. However, forcing the fit of data with the exponential function leads to $\beta=0.29\pm0.02$ nm^{-1}, which is small. This result is consistent with the previously reported STM break-junction[106] and photochemistry data[107, 112].

Compared to $A(CG)_nT$, the resistance of $ACGC(AT)_mGCGT$ and $ACGC(AT)_{m-1}AGCGT$ is more strongly length dependent (see Fig. 2.3b). The insertion of the AT blocks in the middle of the GC sequences introduce a large change in the length dependence of the DNA resistance. The resistance of the sequences in linear scale shows large deviation from the simple linear length dependence (Fig. 2.14c). Note that only the data for the AT blocks shorter than 4 base pairs are plotted here. If the resistance for the sequences with longer AT blocks were included, the deviation from the linear dependence is even larger. In contrast to the linear scale plot, the semi-logarithmic plot shows a more linear behavior (Fig. 2.14d), indicating exponential length dependence of the DNA resistance. From the slope of the semi-logarithmic plot, we determined that β=1.20±0.12 nm^{-1}, far larger than that for $A(CG)_nT$. This observation supports that the AT blocks act as tunneling barriers to give rise to exponential length dependence of the resistance.

$ACGC(AT)_mGCGT$ and $ACGC(AT)_{m-1}AGCGT$ contains GC blocks, which are expected to act as hopping sites. In other words, tunneling in these sequences arises only from the AT blocks. We thus analyzed the data by excluding the resistance contribution from the GC blocks. The linear scale plot shows large deviation from the simple linear length dependence (Fig. 2.14e). In contrast, the semi-logarithmic plot (Fig. 2.14f) shows good linear dependence, confirming the tunneling behavior, and the exponential decay constant, β, was found to be 2.03±0.12 nm^{-1}, which is similar to those in other molecular wire system[45]. This observation also agrees with the theoretical predictions[114-116] and experimental results[112, 113] reported in literature.

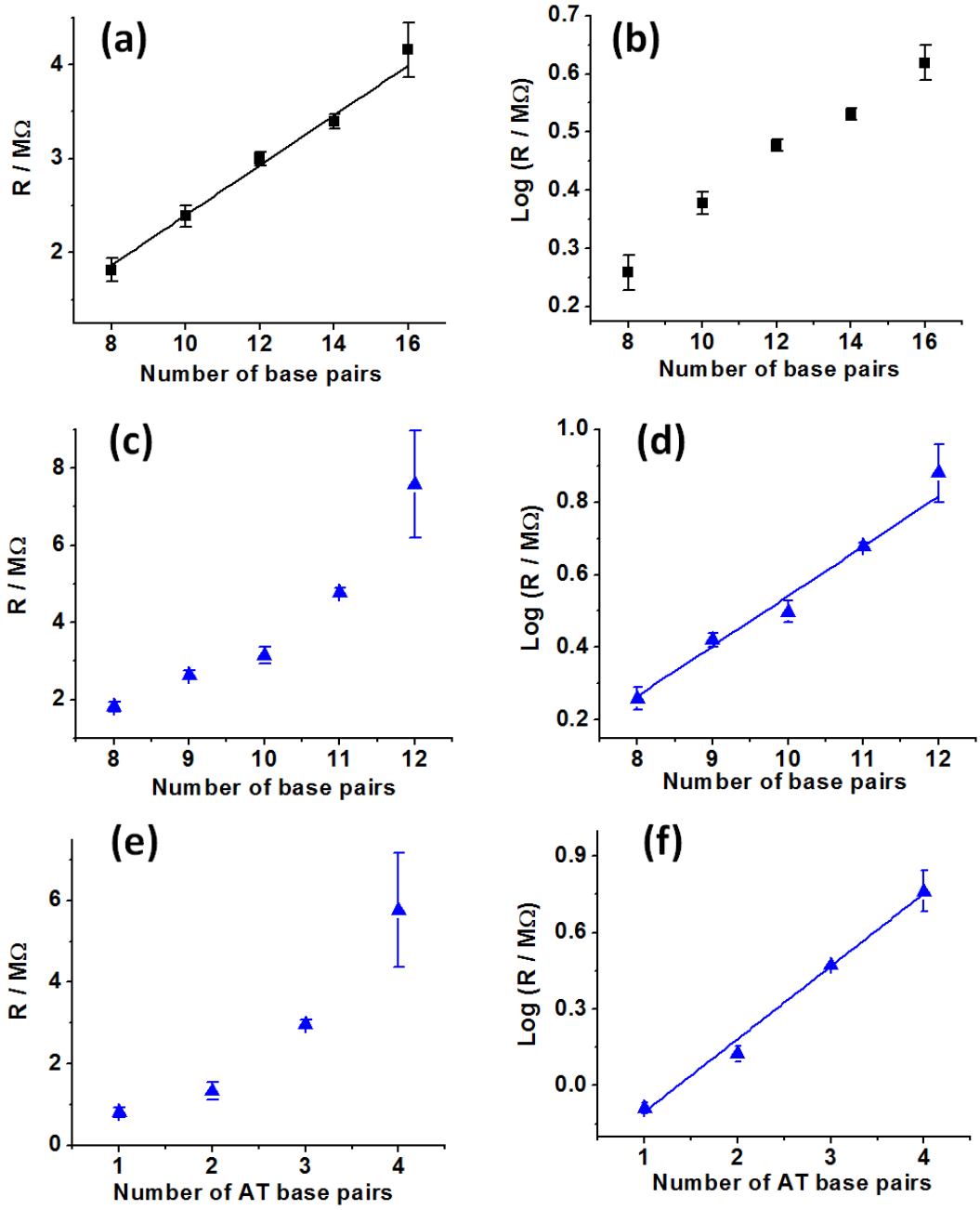


Figure 2.14 Linear and semi-logarithmic plots of resistance vs. length of different DNA sequences. Linear (a) and semi-logarithmic (b) plots of resistance vs. length for $A(CG)_nT$

(n=3~7). Linear (c) and semi-logarithmic (d) plots of resistance vs. length for ACGC(AT)$_m$GCGT (m=1~4) and ACGC(AT)$_{m-1}$AGCGT (m=1~3). Linear (e) and semi-logarithmic (f) plots of resistance vs. length for the inserted AT blocks in ACGC(AT)$_m$GCGT (m=1~4) and ACGC(AT)$_{m-1}$AGCGT (m=1~3).

2.7.7 Derivations of Eq. 2.4 and discussion of validity of the assumption

If we assume that the energy dependent resistance function, R(E), of A(CG)$_n$T, is the sum of contact (R_c) and hopping (R_h) contributions, we can express the Seebeck coefficients of A(CG)$_n$T sequences as

$$S\left[A(CG)_nT\right]=\frac{\pi^2k_B^2T}{3e}\cdot\left[\left(\frac{1}{R}\cdot\frac{\partial R_c}{\partial E}\right)_{E=E_F}+\left(\frac{1}{R}\cdot\frac{\partial R_h}{\partial E}\right)_{E=E_F}\right]. \quad (2.9)$$

Eq.2.9 can be simplified as,

$$S\left[A(CG)_nT\right]=\frac{\pi^2k_B^2T}{3e}\cdot\frac{R_c}{R}\cdot\left(\frac{1}{R_c}\cdot\frac{\partial R_c}{\partial E}\right)_{E=E_F}+\frac{\pi^2k_B^2T}{3e}\cdot\frac{R_h}{R}\cdot\left(\frac{1}{R_h}\cdot\frac{\partial R_h}{\partial E}\right)_{E=E_F} \quad (2.10)$$
$$=\frac{R_c}{R}S_c+\frac{R_h}{R}S_h$$

, leading to Eq. 2.4. Eq. 2.6 can also be derived from this.

Alternatively, we may assume that the total thermal voltage as a sum of the contact and hopping thermal voltages, given by [142]

$$\Delta V=S_c\Delta T_c+S_h\Delta T_h \quad (2.11)$$

If we further assume that total temperature difference is a sum of the contact and hopping temperature differences, or [142]

$$\Delta T=\Delta T_c+\Delta T_h \quad (2.12).$$

Finally, we assume that heat transports along from left to right electrodes along the molecule without loss sideway, or

$$\Delta T_{h,c}=(\kappa/\kappa_{h,c})\,\Delta T \quad (2.13)$$

, where κ, κ_c and κ_h are the total, contact and hopping thermal conductance. Combing Eqs. 2.11, 2.12 and 2.13, we have

$$\square S=(\kappa/\kappa_c)S_c+(\kappa/\kappa_h)S_h \quad (2.14)$$

Note that in addition to the above assumptions, Eq.2.14 consumes that we could define site temperature along a molecule. The validity of the concept is discussed in literature [143, 144].

Eq. 2.4 and Eq. 14 express the total Seebeck coefficient as resistance and thermal resistance (inverse of thermal conductance) weighted sum, respectively. According to the Wiedeman-Franz law, the electrical conductivity is proportional to the thermal conductivity, so Eq. 2.4 Eq. 2.14 are equivalent. The Wiedeman-Franz law is not yet well established in molecular junctions, but one of us[145] showed that the law holds when the energy gap between the electrode Fermi energy and molecular site energy is sufficiently large (compared to the transfer integral). This result was obtained in the tunneling regime. In the hopping region, experimental and theoretical evidence showed that the hopping

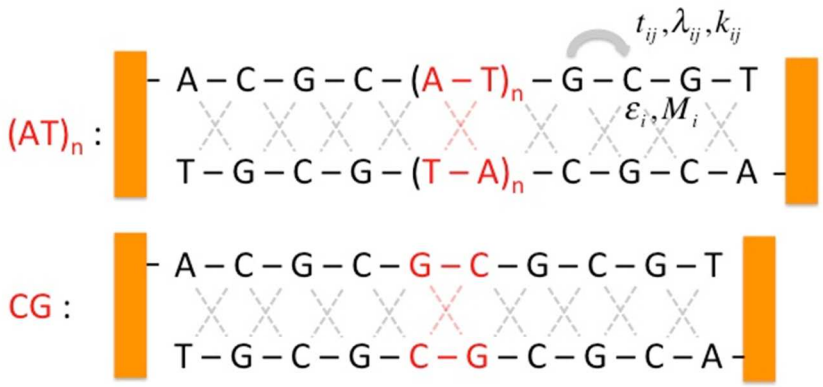
region is connected adiabatically to the tunneling region[146], indicating that the Wiedeman-Franz law might be applicable also in the hopping regime, although a complete theory is still lacking.

2.7.8 Tight binding theory of DNA thermoelectricity

A theory that treats electron-phonon coupling in the strong coupling regime has been developed to calculate DNA conductance[138]. The theory has been recently extended to determine the Seebeck coefficient in conducting polymers[139]. While the strong coupling theory is useful in predicting qualitative trends of molecular conductance and thermoelectric effect, it cannot include chemical details in the calculations easily. In this respect, the weak coupling theory is more suitable. Previously, the weak coupling theory has been used to explain the tunneling-hopping transition in single oligomers,[140] and to determine other charge transport properties, such as the electric current noise in molecular junctions[141]. In this work, we applied the weak coupling theory to examine the length and sequence dependence of the DNA Seebeck coefficient.

We adopted an extended Su-Schrieffer-Heeger model with the Lennard-Jones potential to describe dsDNA. The model considers electrons, phonons and electron-phonon coupling (See Fig. 2.15 for the Hamiltonian). To perform the calculation, we assumed each DNA base as a site with key parameters depicted in Fig. 2.15. The parameters that describe the electrons in DNA were determined from the DNA hole transfer rates measured by transient absorption spectroscopy.[147] The phonons in DNA

were treated with the nearest-neighbor interaction approximation using the Lennard-Jones potential. The force field between the nearest-neighbor bases was uniform with a force field constant, $k_{ij} = 0.25\, eV/\text{Å}^2$. The mass of each site was taken to be molecular mass of the base. The electrodes were considered by assuming their Fermi energy to be $E_F = -7.75\, eV$. The electron-phonon coupling constant, $\lambda_{ij} = -0.6$ and temperature, T= $8\, K$, were used to stabilize the self-consistent calculation. Because the inelastic contribution to the electron-phonon coupling is expected to scale with λ^2, we do not expect that the result change qualitatively for larger λ. The calculated Seebeck coefficient and its dependence on the DNA length and sequence are summarized in Fig. 2.16. The calculation shows that the insertion of AT blocks in the middle of GC sequences lead to larger Seebeck coefficients, in agreement with the experimental data. However, the calculation was performed at 8 K, which could not predict the tunneling-hopping transition observed at room temperature. Further work will be needed to fully describe both the conductance and thermoelectricity in DNA.



$$H_{SSH+LJ} = -\sum_{\langle ij\rangle,\sigma} t_{ij}\left[1-\lambda_{ij}\left(u_i-u_j\right)\right]\left(c_{i\sigma}^{\dagger}c_{j\sigma}+H.c.\right)+\sum_{i,\sigma}\varepsilon_i n_{i\sigma}$$
$$+1/2\sum_{j=1}^{N} M_j\left(du_j/dt\right)^2+1/2\sum_{ij}^{N} u_i\Phi\left(\vec{R}_i-\vec{R}_j\right)u_j$$

Figure 2.15 The Su-Schrieffer-Heeger model of dsDNA, where ε_i and M_i are the site energy and mass, respectively, t_{ij} is the transfer integral, λ_{ij} is describes the electron-phonon coupling, and k_{ij} is force field constant.

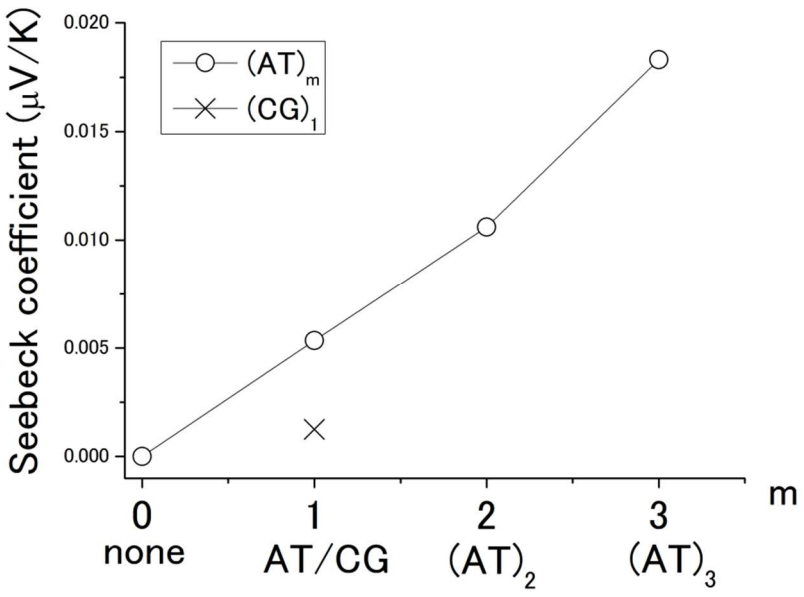


Figure 2.16 Seebeck coefficient and its dependence on DNA sequence and length. The Seebeck coefficients are for the inserted part in the middle of sequence. AT, $(AT)_2$, $(AT)_3$, CG and none means calculation for one, two, three alternating AT units, one CG alternating unit, and no molecule.

2.8 Conclusions

In this paper I have studied the charge transport and thermoelectric effect in single DNA molecules with different sequences and lengths. The transport mechanism in CG sequences (5'-$A(CG)_nT$-3', with n=3-7) is hole hopping, as indicated by linear dependence of the resistance on the molecular length. The Seebeck coefficient is small and weakly dependent on the molecular length. Inserting a block of AT base pairs in the

middle of a CG sequence (ACGC$(AT)_m$GCGT-3', m=1-4; and 5'-ACGC$(AT)_{m-1}$AGCGT-3', m=1-3) changes both the charge transport and thermoelectric effect significantly. When the inserted AT block is shorter than 4 base pairs, it acts as a tunneling barrier with resistance increases exponentially with the block length, and its Seebeck coefficient is large compared to the -A$(CG)_n$T sequences. However, when the inserted AT block is longer than 4 base pairs, the charge transport mechanism undergoes transition from tunneling to hopping, and the resistance becomes weakly length dependent, and the Seebeck coefficient drops to smaller values. The experimental results have been analyzed by tunneling and hopping models, and compared with an extended Su-Schrieffer-Heeger model with the Lennard-Jones potential. The work demonstrates that the DNA thermoelectricity can be tuned by its length and sequence, and investigating the thermoelectric effect provides new insights into charge transport in DNA.

3 FORCE-INDUCED ELECTRON TRANSFER REACTIONS AND CONDUCTANCE SWITCHING IN SINGLE MOLECULES

3.1 Introduction

Electron transfer reactions play a key role in many basic chemical and biological processes, including photosynthesis, electrochemical reactions, organic photovoltaic cells, and metabolic processes in living systems.[148] It is assumed by modern electron transfer reaction theory[149, 150] that there is a coupling between the electronic and structural degrees of freedom, and that thermal fluctuations create a structurally favorable situation to bring the electronic energy of the reactant to the level of the product prior to electron transfer. Here direct evidence is provided that a mechanical force can help create the structurally favorable situation, and induce electron reactions with single molecule measurement. I measure electron transfer in a single redox molecule covalently connected to two electrodes while stretching the molecule with the electrodes, detect force-induced switching of the molecule between reduced and oxidized states, and determine the redox potential shift due to the force. My theoretical modeling reveals that the force-induced distortion in the molecular structure changes the ionization potential, and thus the redox potential. My work points to a way to examine the interplay between electronic and structural properties of molecules in electron transfer reactions, and switch the conductance of a single molecule via mechanically changing its redox state, which is relevant to electromechanical functions of redox molecules.

Controlling chemical reactions is of great importance to the creation of new matter, and to the understanding of nature. In additional to temperature, pH, concentrations, light and electrical field, mechanical forces can also induce chemical reactions[151, 152]. Experimental studies of mechanochemistry include ball milling/grinding[82, 83], and ultrasound bath[153, 154] techniques, but atomic force microscopy (AFM) allows the study of chemical bond rupture in single molecule (e.g., proteins and DNA[84]). An important study is about the force-induced rupture of the sulfur-sulfur bond in biopolymers[88-90].

Here I investigated the electron transfer reactions in a ferrocene compound covalently connected between two gold electrodes by mechanically stretching the molecule in an electrolyte under electrochemical control[155]. Ferrocene is one of the most well studied redox molecules, and the moiety can reversibly accept an electron (become reduced) from an electrode, and give away the electron (re-oxidized) to the electrode without bond rupture[79]. The ferrocene compound (1,1'-Ferrocenyl diester) studied here (Fig. 3.1a) consists of a ferrocene redox center and two linker groups that can covalently bind to the gold electrodes. For simplicity, the ferrocene compound in this work is referred as Fc-Lip. As a control experiment, I also studied 1,4-Phenylene bis(5-(1,2-dithiolan-3-yl) pentanoate), which is similar to 1,1'-Ferrocenyl diester but lacks the ferrocene redox center (referred to as Lip-ctr). I measure the redox states of single Fc-Lip molecules from the characteristic single molecule conductance with the scanning tunneling microscope (STM) break junction technique[11] (described in methods section), where the gold tip and gold substrate electrodes serve as the two electrodes to apply a

stretching force to the molecule, and determine its conductance. During the measurement, I control the potential of the molecules with respect to a reference electrode (in Fig. 3.1b).

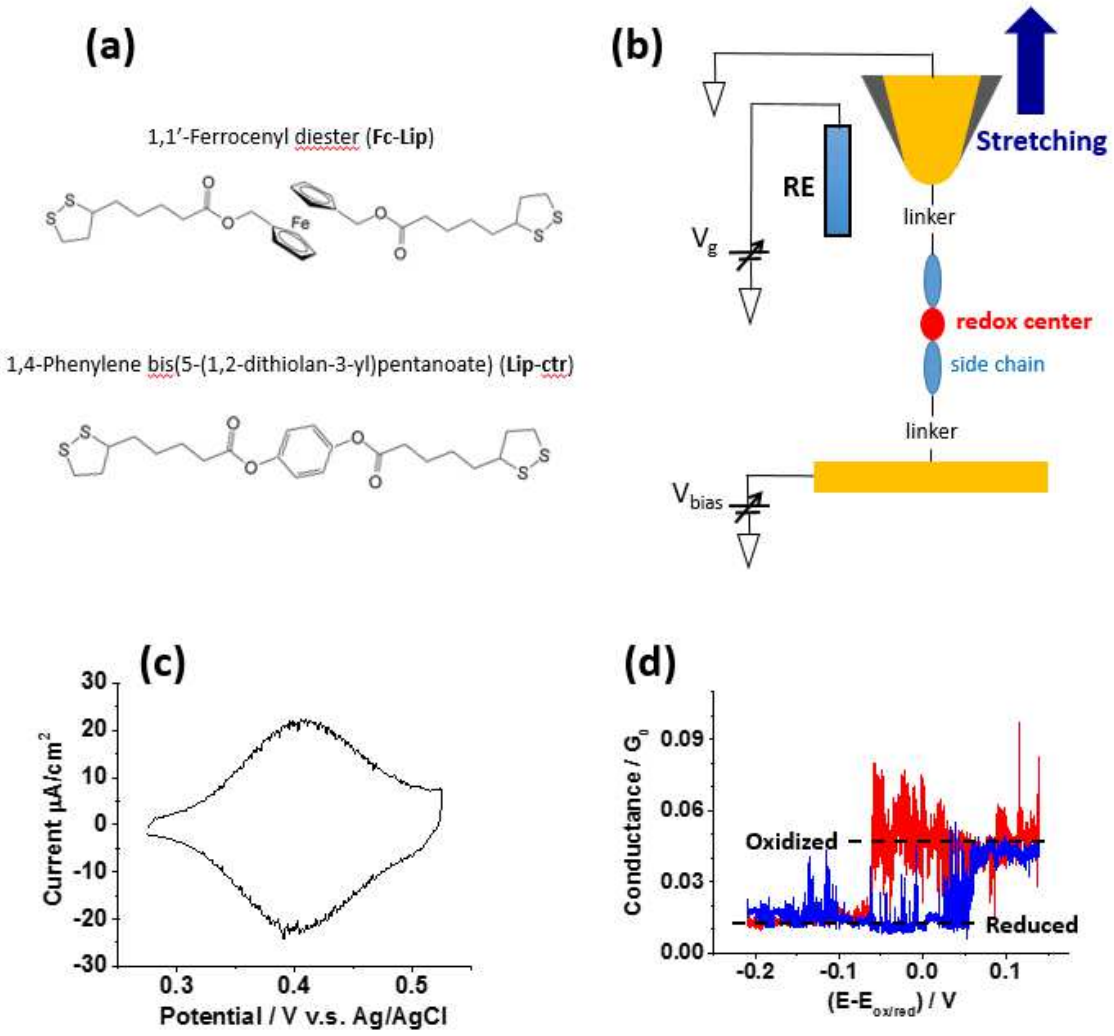


Figure 3.1 Structure and electrochemical study of 1,1'-Ferrocenyl diester. (a) Chemical structure of 1,1'-Ferrocenyl diester (Fc-Lip) and 1,4-Phenylene bis(5-(1,2-dithiolan-3-yl)pentanoate) (Lip-ctr). (b) Illustration of the STM experiment. The the STM substrate and tip are working electrode 1(WE1) and working electrode 2 (WE2), the reference electrode is a silver wire, and the counter electrode is a platinium wire. The

redox molecule is bridged between the tip and substrate via the double thiol linker groups.A small bias (~30 mV) is applied between WE1and WE2. (c) Cyclic voltammetry of the SAM on a gold surface in 0.1 M NaClO4 aqueous solution with Ag wire as quasi-reference electrode and Pt wire as counter electrode(sweeping rate 100 mV/s). (d) Two representative curves of the conductance two-state feature V.S. (E-Eox/red) in sweeps of gate voltage. Different colors represent different sweeps. Black dashed lines are guide to eyes emphasizing the reduced and oxidized conductance levels. (sweeping rate 1 V/s)

3.2 Methods

3.2.1 Preparation of Fc-Lip SAM, Lip-ctr SAM, and Ferrocene dicarboxylic acid SAM

The double sulfur groups on the ends of Fc-Lip molecule allows covalent binding to gold electrodes for electrical measurements[156-159]. Based on this binding behavior, I immobilized a self-assembled monolayer of Fc-Lip or Lip-ctr on the gold surface (gold thickness about 160nm), which was vapor deposited on mica under ultra-high vacuum. Before each experiment, the gold surface was annealed with hydrogen flame briefly, then immersed in chloroform containing 100 μM Fc-Lip or 100 μM Lip-ctr. After 2 hours' incubation, the substrate was rinsed with chloroform and dried by nitrogen flow. Then I attached the coated substrate to the sample holder of the STM, then covered by 0.2 mL of 100 mM $NaClO_4$ (≥99%, Fluka Analytical) aqueous solution.

The carboxylic groups on Ferrocene dicarboxylic acid is able to bind with gold electrodes for electrical measurements[18], thus the SAM of Ferrocene dicarboxylic acid can be formed on STM gold substrate. The only difference with the preparation of the SAM of Ferrocene or Lip-ctr is that the gold surface was immersed in 100 μM Ferrocene dicarboxylic acid ethanol solution and rinsed by ethanol after incubation, instead of chloroform.

3.2.2 Cyclic voltammetry

To characterize the redox properties of Fc-Lip, I performed cyclic voltammetry on its SAM on a gold surface with Ag/AgCl electrode (in 1M KCl solution) as reference electrode and platinum coil as counter electrode, using an Autolab potentiostat. In addition to characterizing the SAM of Fc-Lip, I also performed cyclic voltammetry before and after each STM experiment to check the stability of Ag quasi-reference electrode (Fig. 3.2).

In the gate controlled STM measurements, the use of silver quasi reference electrode introduced variations in the actual applied gate voltages. To characterize the variations, I performed cyclic voltammograms for 1,1'-Ferrocenyl diester every 20 minutes for 4 hours (all the gate controlled measurements were finished within 4 hours), and recorded the redox potential. Fig. 3.2 shows that the redox potential of 1,1'-Ferrocenyl diester shifted positively with time, which means that the reference potential shifted negatively. The positive shift in redox potential (negative shift in reference potential) is robust in all

the gate controlled STM measurements. I used the difference in redox potential before and after each experiment as the errors in the gate voltages.

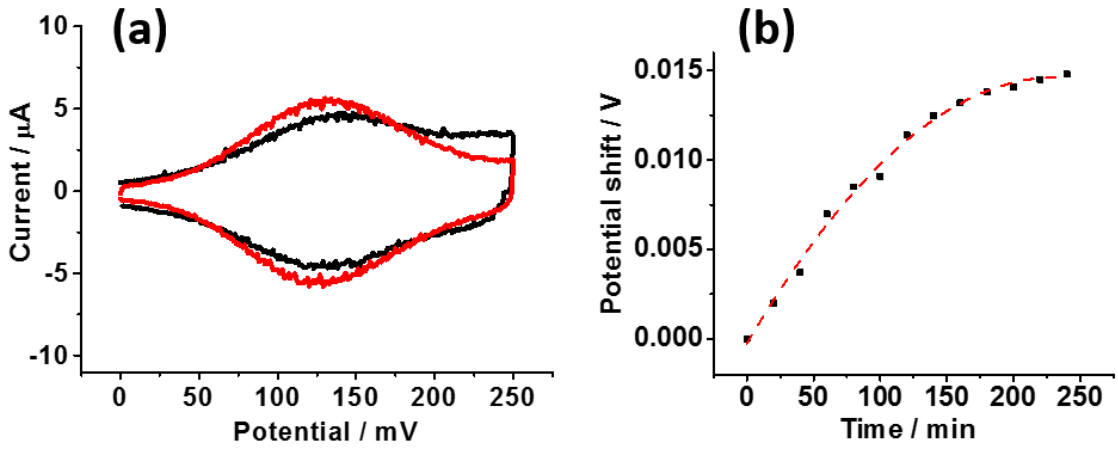


Figure 3.2 Cyclic voltammetry study of 1,1'-Ferroceny diester SAM on Au substrate. (a) the Cyclic voltammograms of the 1,1'-Ferrocenyl diester on an STM gold surface in 100 mM $NaClO_4$ aqueous solution with Ag quasi-reference electrode and Pt counter electrode (sweeping rate 100mV/s). Red and black curves were recorded before and after the same STM experiment, respectively. The same cyclic voltammetry was performed before and after each STM experiment to determine the average redox potential of 1,1'-Ferrocenyl diester and to evaluate the shift of reference potential. (b) Plot of redox potential changes with time due to the shift of Ag quasi-reference electrode. Red dash line is a guide to eyes.

3.2.3 STM setup

I carried out the measurement of force induced change in redox potential with the STM consisting of a controller (Nanoscope IIIA, Digital Instruments Inc.) and a STM scanner (Molecular Imaging). The STM tip was freshly cut from a gold wire (0.25 mm diameter, 99.95%, Alfa Aesar) and coated with Apiezon wax to reduce the leakage current directly through the conducting aqueous solution. A bipotentiostat (Agilent) was used to control gate voltage. I used a silver wire and a platinum coil as quasi-reference electrode and counter electrode, respectively. Fig. 3.1b shows a scheme of the STM setup with gate control. All measurements were carried out in 100 mM $NaClO_4$ aqueous solution.

3.2.4 STM break junction measurement

In each set of experiment, I performed the STM break junction technique[11] at a small bias (~30 mV) and a specific fixed gate voltage (see Table 3.1 for the applied bias and gate voltages). Briefly, the STM tip was first brought into contact with the Fc-Lip molecules on the gold substrate, allowing the double sulfur bond to bind with the gold tip. The tip was then retracted from the substrate, during which a conductance-distance trace was recorded (Figs. 3.3b, e, and h). I repeated the process was repeated thousands of times. A conductance histogram (Figs. 3.3c, 2f, and 2i) was constructed from thousands of the individual conductance traces, and the peak position in the conductance histogram gave the average conductance of the studied molecule.

Table 3.1 Measured Redox Potential and Applied Overpotential for Each Experiment

Experiment	$E_{1/2}$ (mV)	Bias (mV)	Vg (mV)	Overpotential (mV)
1	134±7	40	70±7	-64±7
2	110±9	20	50±9	-60±9
3	100±4	22	49±4	-51±4
4	91±8	38	121±8	-30±8
5	100±5	26	87±5	-13±5
6	137±10	36	122±10	-15±10
7	166±8	22	159±8	-7±8
8	83±6	24	98±6	15±6
9	104±11	32	134±11	30±11
10	131±5	28	186±5	55±5

3.2.5 Sweeps of STM gate voltage

I carried out the STM break junction technique at a small bias (10 mV) and a fixed gate voltage (-0.1 V) on the SAM of studied molecule. Once a plateau was detected by the program, the tip was halted and the gate voltage was swept from -0.1 V to 0.2 V, at a speed of 1 V/s. The current V.S. gate voltage curves were recorded.

3.3 Electrochemical Potential Sweep on Single Molecular Junctions

As shown by cyclic voltammetry (Fig. 3.1c), the redox reaction of the Fc-Lip attached to gold electrodes is reversible with redox potential at ~405 mV vs. Ag/AgCl

reference electrode. This redox potential agrees with the previously reported redox potential of 1,1'-methyl substituted ferrocene on gold electrodes[160, 161]. From the areas of the redox peaks in the cyclic voltammogram, the surface coverage is measured to be 187 $\pm$1.6 pmol cm^{-2}, which is within the reasonable range of thiolated molecule monolayer modified on gold surface[57].

To study the redox reaction of single Fc-Lip molecules, I bridge a Fc-Lip molecule between the tip and substrate electrodes, and then swept the electrochemical potential while monitoring the conductance of the redox molecule (details described in methods section). A typical record of the conductance of Fc-Lip vs. potential is shown in Fig. 3.1d. At low potentials, the redox molecule is in the reduced state, showing a relatively low conductance (~0.01 G_0, where $G_0 = 7.748 \times 10^{-5}$ S is the conductance quantum). However, at high potentials, Fc-Lip becomes oxidized, which is observed as a sudden jump of conductance to a higher level (~0.05 G_0). The increase in conductance is consistent with the previous reports[79], and further validated by performing a large number of measurements and statistical analysis discussed below (Fig. 3.3). The discrete low and high conductance levels of a single Fc-Lip molecule measured by the STM break junction method enables us to determine if the molecule is in the reduced (low conductance) or oxidized (high-conductance) states, and the switching between the low and high conductance levels measures the redox reaction events. This discrete conductance switching is different from the gradual conductance changing with potential in other systems[57, 162, 163] (see further discussions in section 3.6.1).

3.4 Mechanical Force-induced Redox Reactions

To examine mechanical force-induced redox reactions, I stretch the molecule by separating the tip and substrate electrodes during STM break junction measurement, and monitor the redox state of Fc-Lip from the conductance switching (See experimental details in Methods section). The measurement was performed by holding the potential at different values, below, at and above the redox potential of unstretched Fc-Lip (marked on Fig. 3.3a). At potentials well below the redox potential (e.g., -88 mV), Fc-Lip is in the reduced state with a probability of 97% according to the Nernst equation. The individual conductance traces (Fig. 3.3b) reveal plateaus (marked by arrows) corresponding to the formation of single Fc-Lip molecules bridged between the two electrodes, followed by abrupt conductance drops as the bonds at the molecule-electrode contact break[164]. The conductance plateaus are located close to ~0.01 G_0, at the low conductance level as the molecule is in the reduced state. The lack of the large conductance switching in the conductance traces as shown in Fig. 3.3d indicates no force-induced electron transfer reaction takes place at the low potentials. The corresponding conductance histogram constructed from about 1000 of the individual conductance traces displays a single pronounced peak near 0.01 G_0 (Fig. 3.3c), which further confirms that the molecules are in the reduced low conductance state at -88 mV. These results show that at the low potentials, the mechanical force is not sufficient to cause switching of the redox state of Fc-Lip (Fig. 3.3d).

At potentials well above the redox potential, Fc-Lip is expected to be in its oxidized state. For instance, at +78 mV, the molecule has a probability of 95% in the oxidized state according to the Nernst equation. The individual conductance traces of the molecule at +78 mV display plateaus at the high conductance level (Fig. 3.3e), confirming that the molecule is in the oxidized state. Conductance histogram determined form the individual conductance traces shows a single well-defined peak at ~0.05 G_0 (Fig. 3.3f). Like the case of holding the potential well below the redox potential, I do not observe large conductance switching during stretching of the molecule, suggesting no detectable force-induced switching in the redox state at high potentials (Fig. 3.3g).

At ~ -7 mV, close to the redox potential, both reduced and oxidized states are possible. This is reflected by the presence of plateaus at both the low and high conductance levels, corresponding to the reduce and oxidized states of the molecule, in the conductance traces (Fig. 3.3h). At this potential, I also noticed that the conductance often switches abruptly from low to high conductance levels during stretching of the molecule (curves 2 and 3), indicating the switching of the molecule from the reduced to the oxidized states under the stretching force. The corresponding conductance histogram reveals two peaks, at 0.01 G_0 and 0.05 G_0, respectively, suggesting coexistence of both the reduced and oxidized states of the redox molecule (Fig. 3.3i). These observations indicate that unlike the cases where the potential is held either well below (e.g., -88 mV, Fig. 3.3b, and -121 mV, Fig. 3.11), or well above the redox potential (+78 mV, Fig. 3.3j), when the electrodes are held near the redox potential, force induces significant switching of the electron transfer reaction in Fc-Lip. As a characterization of the stability of the

junction, the average plateau length in conductance decay curves before the broken of molecular junctions was similar for measurements at -88 mV, -7 mV and +78 mV (Fig. 3.4).

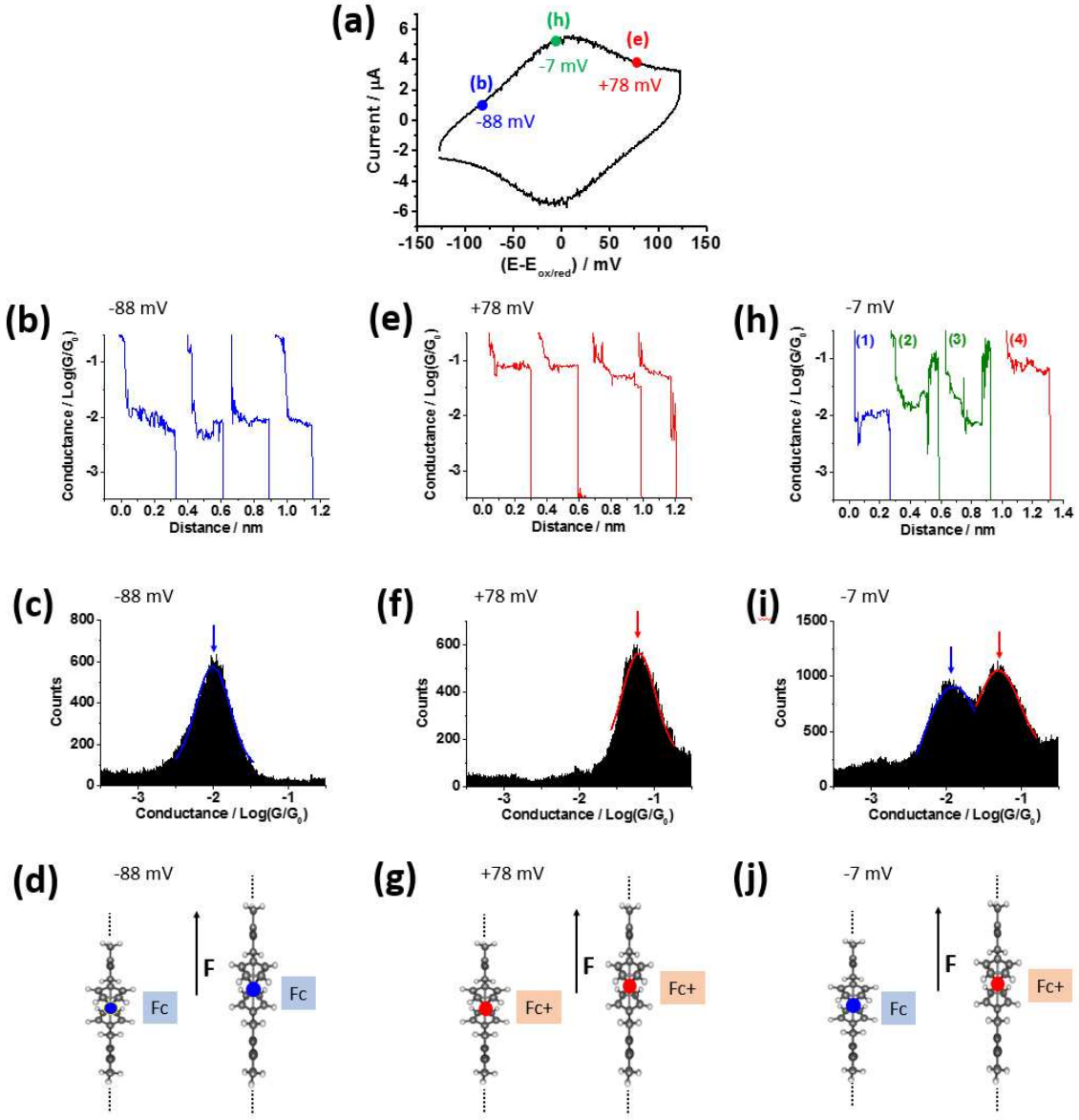


Figure 3.3 Stretching and measurement of 1,1'-Ferrocenyl diester under different gate voltages. (a) Cyclic voltammetry of 1,1'-Ferrocenyl diester (Fc-Lip). The marked dots shows (E-Eox/red) of STM measurements discussed in below.

Collected at -88 mV, (b) the conductance decay curves show plateaus at lower conductance. (c) The conductance histogram shows only one peak at lower conductance range. (d) Stretching doesn't result in oxidation of the Fc center.

Collected at +78 mV, (e) The conductance decay curves show plateaus at higher conductance. (f) The conductance histogram shows only one peak at higher conductance range. (g) Stretching doesn't influence the redox state of the Fc+ center.

Collected at -7 mV, (h) the conductance decay curves show plateaus at both lower(curve 1) and higher conductance(curve 4), indicating both Fc and Fc+ appears in the measurement. Especially some curves show switching from lower conductance to higher conductance (curves 2 and 3), suggesting oxidation from Fc to Fc+ during the stretching process. (i) The conductance histogram shows two peaks at both lower and higher conductance range. (j) Stretching can result in oxidation from Fc to Fc+.

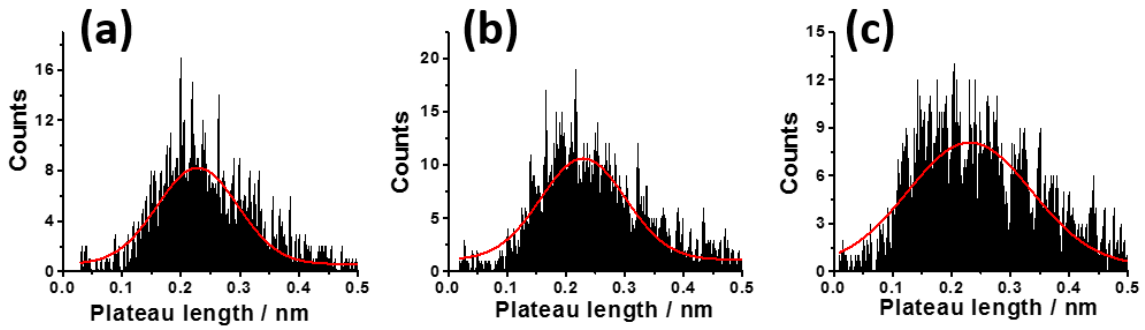


Figure 3.4 Plateau length statistics of conductance decay curves of Fc-Lip at overpotential of (a) -122mV, (b) -7 mV and (c) +78 mV. Each of the statistics show plateau length of 0.23 nm.

Force dependence of conductance has been reported in other systems, but in those works the dependence arises from the force-induced change in the molecule-electrode coupling, and observed changes are continuous,[31, 32, 165] which is contrast to the abrupt and potential sensitive switching observed here. To further examine the roles electrode-molecule contact and the side chain of Fc-Lip, I performed the same measurement on the Lip-ctr. In this control molecule, a phenyl ring replaces the ferrocene redox center (See chemical structure in Fig. 3.5a). Unlike the Fc-Lip, I do not observe force-induced conductance swithcing at different potentials (Figs. 3.5b and c), and the conductance histograms reveals only a single peak (Figs. 3.5d and e). This control experiment demonstrates that the conductance change in Fc-Lip is origined from the ferrocene redox center.

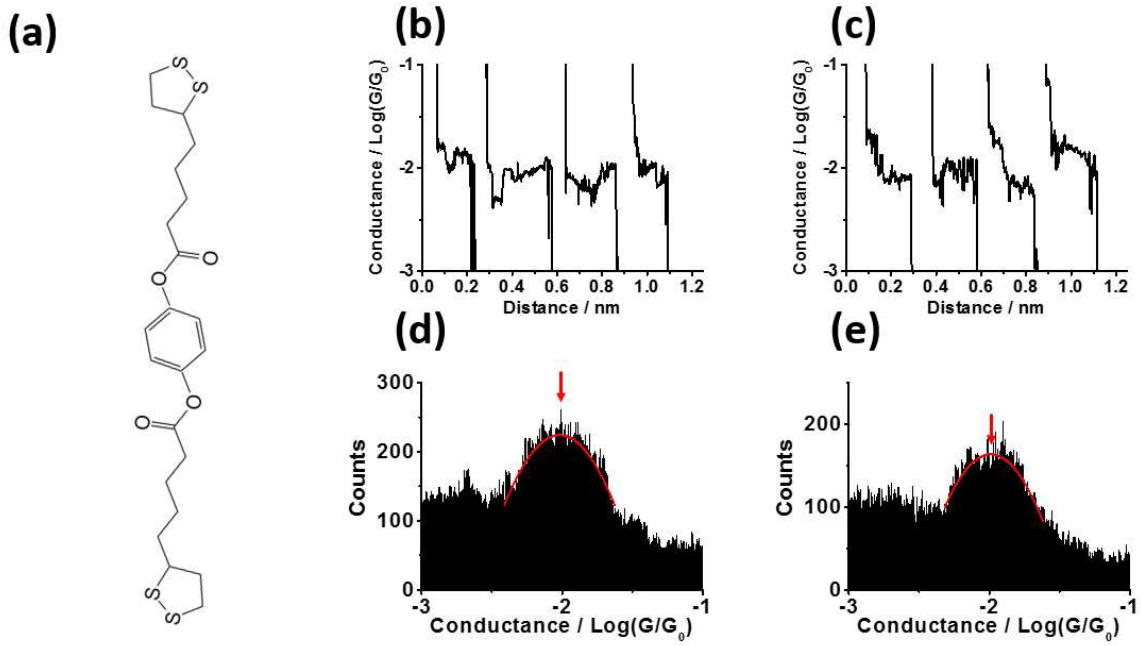


Figure 3.5 Structure and electrochemical calibration of 1,4-Phenylene bis(5-(1,2-dithiolan-3-yl)pentanoate) (Lip-ctr). (a) Chemical structure of Lip-ctr. (b) Individual conductance decay curves recorded at Vg=0 mV. (c) Individual conductance decay curves recorded at Vg=200 mV. (d) Conductance histograms constructed from conductance decay curves recorded at Vg=0 mV. (e) Conductance histograms constructed from conductance decay curves recorded at Vg=200 mV.

To more clearly show the mechanical force-induced electron transfer, I construct a 2D histogram of conductance vs. stretching distance by counting all the traces that show conductane switching at $E\text{-}E_{ox/red}$ = +30 mV (Fig. 3.6a). The 2D histogram revelas two regions, corresponding to the low conductance reduced state, and high conductance oxidized state, respectively. It also indicates that mechanically stretcing of the molecule

can cause swithcing of the molecule from the reduced state to the oxidized state. To examine the relative distributions of the reduced and oxidized states, I plot 1D conductance histograms at difference strecthing distances (marked by red dash lines in Fig. 3.6a). As shown in Figs. 3.6b-e, because of force-induced oxidation of the molecule, the relative peak area of the higher conductance (oxidized) state increases with stretching distance. I construct similar 2D conductance vs. distance histogram and 1D conductance histograms of both stretched and unstretched Fc-Lip for all the conductance traces collected at +30 mV (See section 3.6.3).

I determine the areas of the low and high conductance peaks in each 1D histogram at differenet stretching distances. The peak areas should be proportional to the numbers of Fc-Lip in the reduced and oxidized states, respectively[76,78] (see more in section 3.6.4). Then from the histogram peak areas, I determine the probabilities of the molecule in the reduced and oxidized states, and also the change of the probability in each state with stretching distance at a given potential. The logarithemic ratio of the high and low conductance peak areas are plotted in Fig. 3.6f, indicating that the probability of the molecule in the oxidized state increases with stretching distance. By analyzing data collected at vairous potentials with the same procedure, the same conclusion were reached that molecules under stretch have a greater probability to be in the oxidized state. (Fig. 3.7)

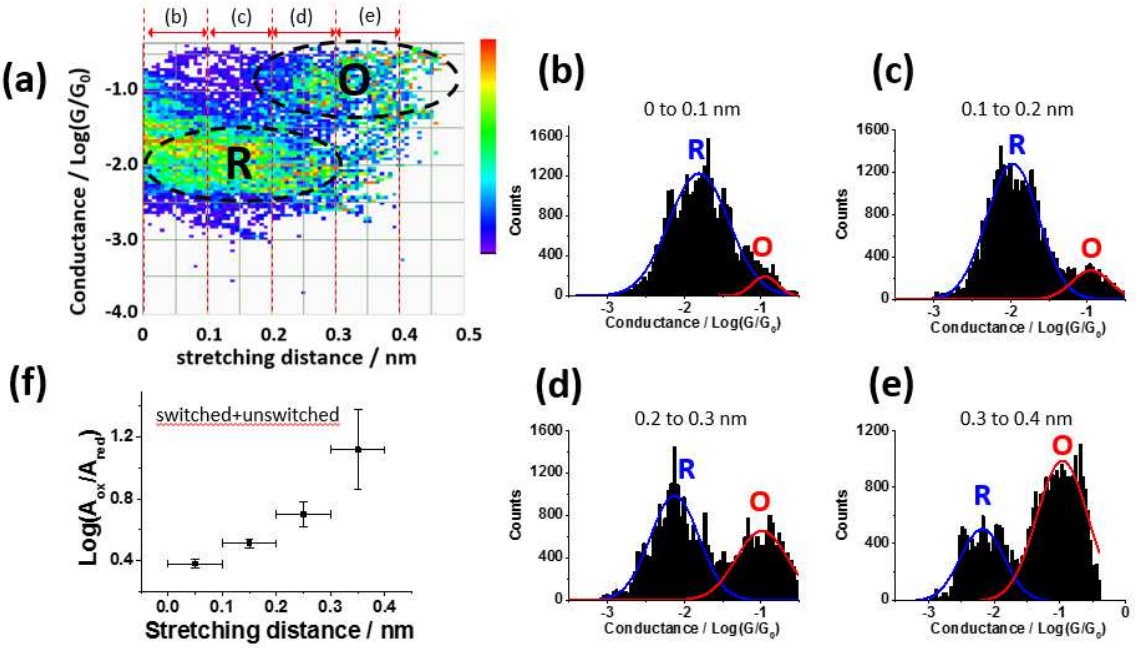


Figure 3.6 Conductance(plateau part) at different stretching distance for switched curves at E-Eox/red = +30 mV. (a) The conductance V.S. stretching distance 2D histogram of switched curves curves at +30 mV (236 curves, counts are normalized for each distance. The part before the detection of the plateau and after the plateau breaks are removed from each individual curve). In the 2D histogram, between red dashed lines are slices with a width of 0.1 nm to build conductance histograms at (b) 0-0.1 nm, (c) 0.1-0.2 nm, (d) 0.2-0.3 nm and (e) 0.3-0.4 nm. Red and blue curves show Gaussian fittings of the higher and lower conductance peaks. (f) For all curves(switched and non-switched) at +30 mV, the logarithm ratio of the peak area of oxidized and reduced conductance peaks at different distance.

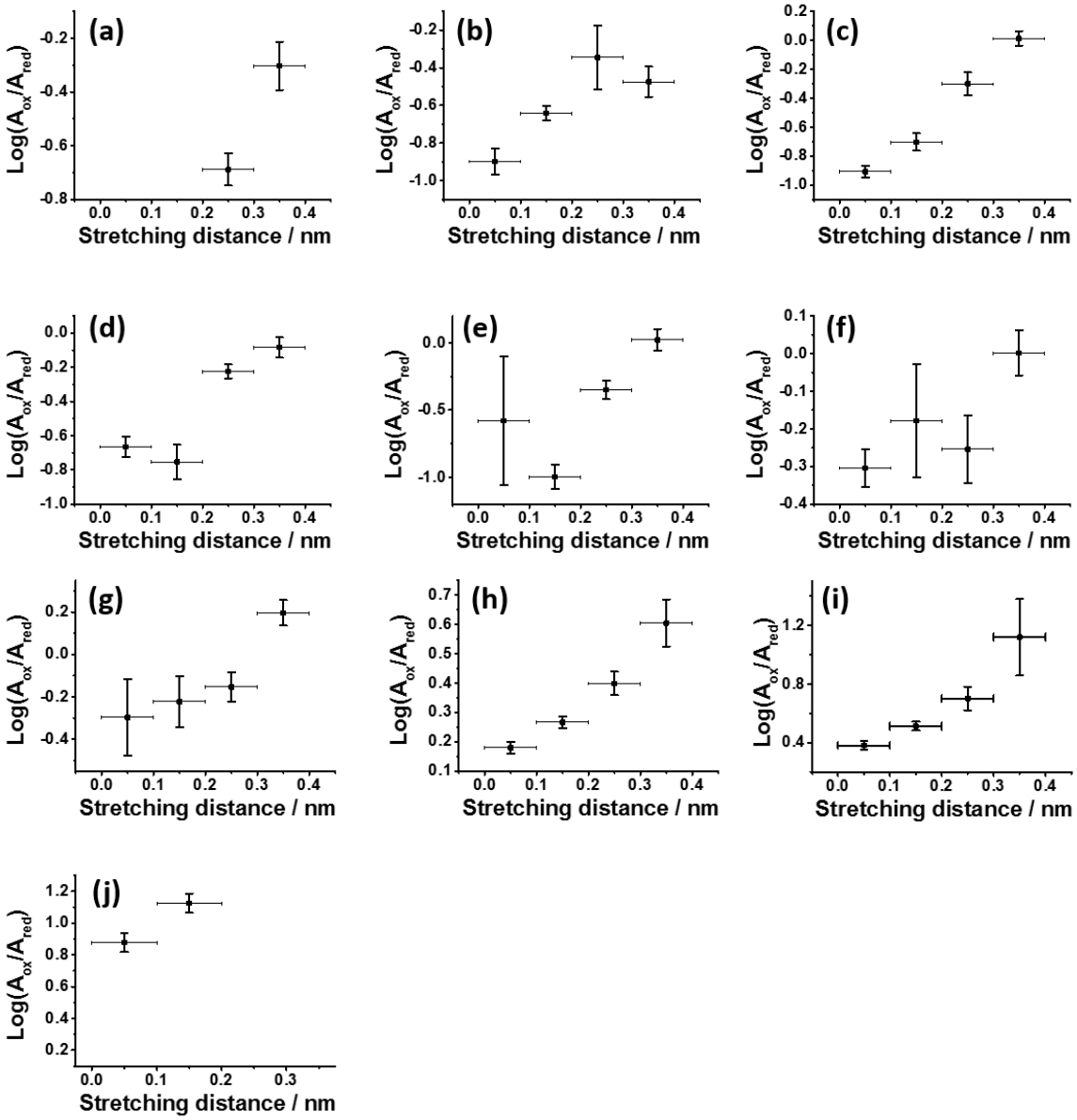


Figure 3.7 Logarithm ratio of the peak area of oxidized and reduced conductance peaks changing with distance at different over potential. (a) -64mV. (b) -60 mV. (c) -51 mV. (d) -30 mV. (e) -15 mV. (f) -13 mV. (g) -7 mV. (h) +15 mV. (i) +30 mV. (j) +55 mV. (x errors represent the range of distance included, y errors are from the error of peak area fitting)

By studying the probabilites of the molecule in the reduced and oxidized states at different potentials and at different strechting distances, it becomes possible to determine the relation between force and redox potential. Fig. 3.8 plots the logarithmic ratio of the probability of the molecule in the oxidized state to that in the reduced state in the beginning and end of stretching with respect to the applied electrochemical potentials. The former refers to data collected during the initial stage of the stretching process with a stretching distance between 0 and 0.1 nm. The latter corresponds the fully stretched molecule (0.3-0.4 nm), beyond which the molecule bridged between the tip and subsrate electrodes breaks down. The breakdown takes place at the Au-Au bond, which has an average breakdown force of ~1.5 nN as shown previously[96, 164, 166]. For unstretched redox molecules, the relative probabilities in the oxidized and reduced states at thermal equilibrium are expected to follow the Nernst equation,

$$E = E_{\text{ox/red}} + 2.303\frac{RT}{nF}\log\left(\frac{\Gamma_{\text{ox}}}{\Gamma_{\text{red}}}\right) \qquad (3.1)$$

, where E is the potential, $E_{\text{ox/red}}$ is the equilibrium redox potential, n is the number of charges transferred per molecule (n=1 for Fc-Lip), R is the universal gas constant, T is temperature and F is the Farady constant, Γ_{ox} and Γ_{red} are the surface concentrations of the redox molecule in its oxidized and reduced states, respectively, which are proportional to the probabilities of the molecule in the oxidized and reduced states.

From the probabilities determined from the areas of oxidation and reduction peaks in the conductance histograms, I plotted $\log(\Gamma_{ox}/\Gamma_{red})$ vs. E for the unstretched (black filled squares) and fully stretched (red filled circles) molecules in Fig. 3.8. The data for the unstretched molecule can be fitted with the Nernst equation given by Eq. 3.1 (black line) with n=1, which is expected for the redox reaction of the Fc-Lip. For comparison, the Nernst equation (n=1) is plotted in Fig. 3.8 (black dashed line). The agreement provides additional evidence that the unstretched Fc-Lip molecule follows the equilibrium thermodynamics of redox reactions. The data for the stretched molecule also follows the Nernst equation relation (red line, in Fig. 3.8) with a slope of 2.3nF/RT (n=1), however, the redox potential is shifted negatively by ~34 mV. The negative shift in the redox potential indicates that the reaction is driven towards oxidation under stretching, which is consistent with the observations described in Figs. 3.3 and 3.6.

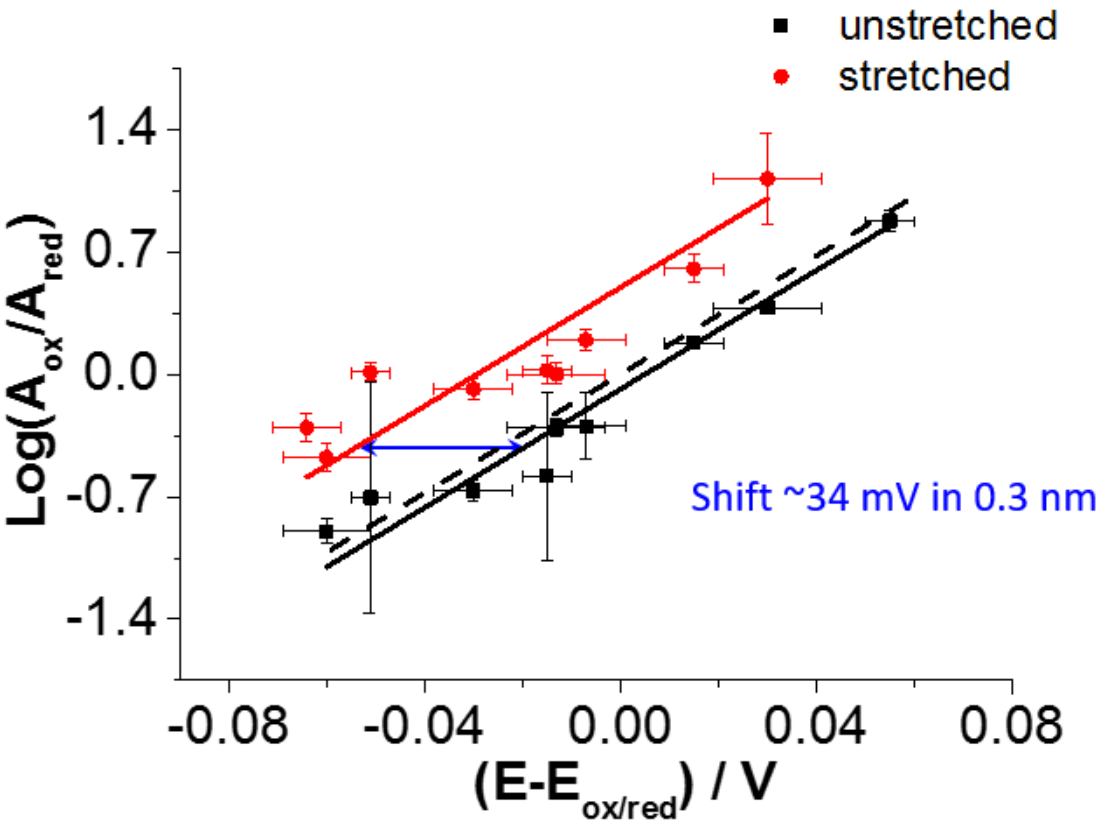


Figure 3.8 Logarithm ratio of the peak area of oxidized and reduced conductance peaks at different potential when the stretching distance is 0 to 0.1 nm(unstreched, black dots), and 0.3 to 0.4 nm(stretched, red dots). x errors are shifts in gate voltage during experiment, y errors are standard errors of the ratio. The black dash line is the relationship obeying Nernst Eq. when n=1. The red and black solid lines are linear fittings of data with a fixed slope of 2.303nF/RT (n=1). The blue arrow shows the shift in redox potential caused by 0.3 nm stretching.

3.5 Theoretical Analysis

According to X-ray crystallography[167, 168], upon oxidation of ferrocene the distance of cyclopentadienyl (Cp)-Fe-Cp increases by 0.006 nm. One can therefore expect that mechanically stretching of Fc-Lip drives the electron transfer reaction towards oxidation, thus giving a more negative value of redox potential. The shift in the redox potential can be understood with a single reaction coordinate model (Cp-Fe-Cp bond) in the spirit of the Marcus electron transfer reaction theory[149, 150], which assumes parabolic energy profiles for the reduced and oxidized states (Fig. 3.9a). When there is no external stretching force, electron transfer reaction occurs when thermal fluctuations bring the molecule to the favorable geometry, corresponding to the interception of the potential profiles of the reduced and oxidized states. When the molecule is stretched, there is an additional term, -Fq, where F is the force and q is the reaction coordinate, in the energy profiles, leading to the parabolic energies for the reduced and oxidized described as Eq.3.2 and Eq.3.3, respectively.

$$U_{red}(q) = \frac{1}{2}k_{red}q^2 - Fq = \frac{1}{2}k_{red}(q - \frac{F}{k_{red}})^2 - \frac{F^2}{2k_{red}} \quad (3.2)$$

$$U_{ox}(q) = \frac{1}{2}k_{ox}(q - q_0)^2 - Fq + \Delta = \frac{1}{2}k_{ox}(q - q_0 - \frac{F}{k_{\mathrm{ox}}})^2 - \frac{F^2}{2k_{ox}} - Fq_0 + \Delta \quad (3.3)$$

, where kred and kox are spring constant of Ferrocene and Ferrocenium moieties, q is reaction coordinate, q_0 is approximately the difference in the Fe-Cp distance between oxidized and reduced forms, F is the stretching force, and Δ is the energy difference

between the oxidized and reduced states. Assuming the force-induced changes in q_t (at which reaction takes place) and reorganization energy to be higher order corrections, the difference of Eq.3.3 and Eq.3.2 leads to force induced shift in the redox potential given by

$$\Delta G_0 = \frac{F^2}{2}\left(\frac{1}{k_{red}} - \frac{1}{k_{ox}}\right) - Fq_0 \quad , \qquad (2)$$

where F is the force, k_{red} and k_{ox} are the effective spring constants of Cp-Fe-Cp in the reduced and oxidized states, respectively, and q_0 is the increase in the distance of Cp-Fe-Cp associated with the oxidation of Fc-Lip. Using F=1.5 nN for the breakdown force of the molecular junction[96, 164, 166], q_0=0.006 nm[167, 168], and spring constants determined by the vibrational frequencies from IR spectroscopy[169] and DFT calculation (Table 3.2), the simple model predicts about -51 mV shift in the redox potential, which is in reasonable agreement with the observation.

Since the above model considers only one coordinate, a more precise model was built to include other degrees of freedoms in the molecule that may change under stretching. To consider all possible degrees of freedom, density functional theory (DFT) calculations were performed on the force-induced redox reactions in Fc-Lip (Fig. 3.9b). Under an increasing stretching force, the molecule undergoes various conformational changes (Fig. 3.9c). The associated energies in the reduced and oxidized states as functions of the stretching distance between the two linker groups of the molecule can be estimated as parabolic shape (Fig. 3.9d and Supplementary Fig. 6). Initially, the added strain is easily accommodated by a slighter curvature of the side chains. As the stretching

increases, the Cp rings begin to twist with respect to each other, until the dihedral angle reaches 180°; beyond this point the strain can only be accommodated by changing bond lengths and angles. The corresponding changes in the critical bond lengths, bond angles and the dihedral angle for relative torsion of the rings and surface energy profiles are presented in part 3.6.5 as supplementary information. The calculation reveals that stretching take places at multiple bonds, but Fe-C1 (C9) bond is a predominant one, which is stretched by 0.01 nm under a maximum stretching force of 1.5 nN. The corresponding adiabatic ionization potential drops by ~65 mV compared with an un-stretched molecule (Fig. 3.9e, and part 3.6.5 for details). Based on the assumption that the thermal and entropic contributions to the free energy of the system are not affected by the stretching, this corresponds to a decrease in the redox potential by 65 mV, which is in good agreement with both the analytical model calculation and experimental data.

The above study demonstrates that a mechanical force induces redox reactions in single molecules as the force changes the bond length and drives the reaction towards the final state that favors the bond length change. This observation supports the thesis that electronic-nuclear coupling is responsible for redox reactions in electron transfer theories. The phenomenon that a mechanical force can control redox states of a single molecule also provides a way to mechanically switch the electronic properties of a single molecule, which supports the vision of molecular machines with electromechanical functions[170].

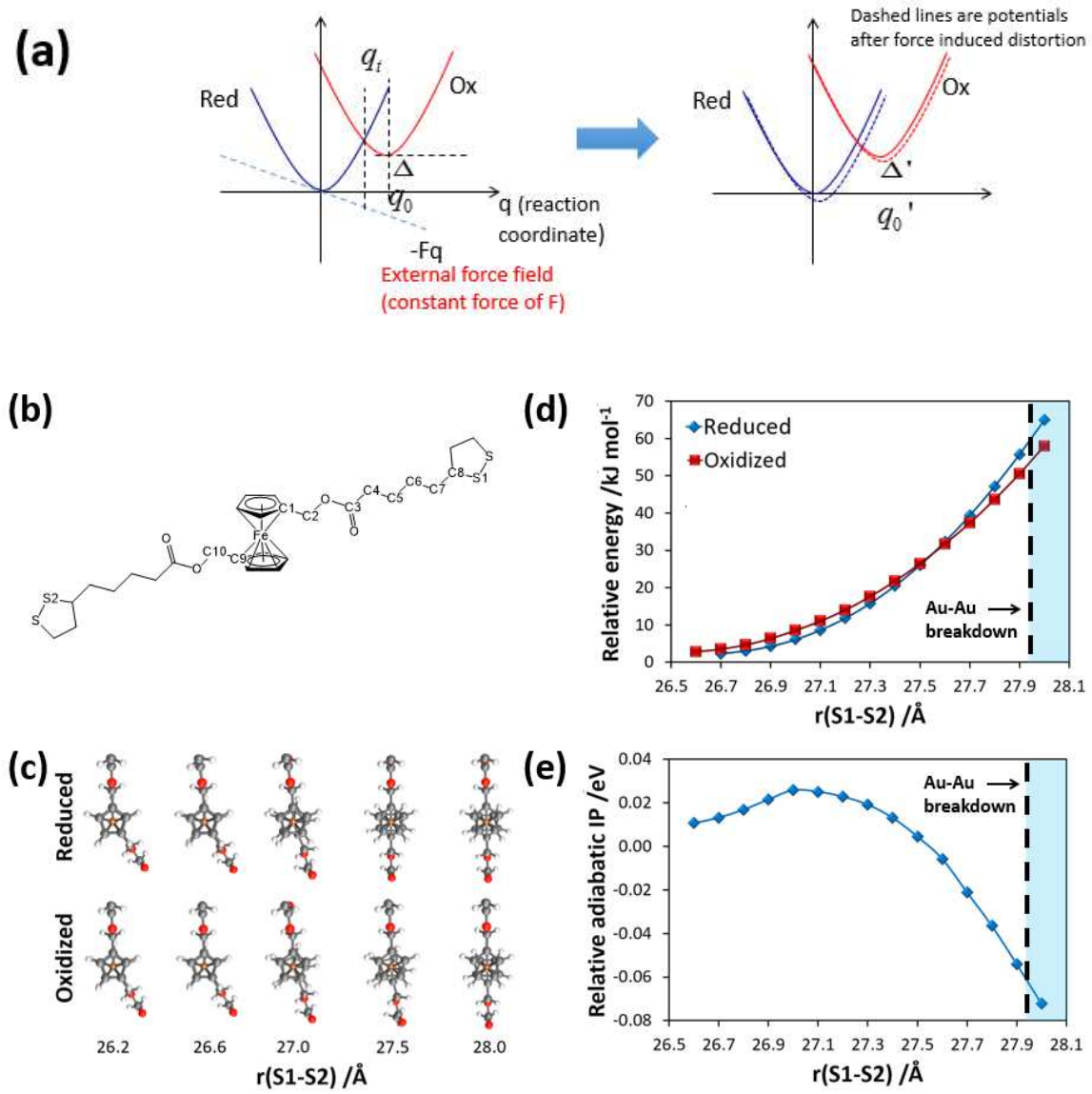


Figure 3.9 Theoretical model and computational results. (a) The theoretical model showing an idealised depiction of the changes in (free) energy of the reduced (blue) and oxidised (red) species as the molecule is stretched, and how this impacts the redox potential. (b) The molecular system used for the computational studies, including atom labels (c) The structural distortion of reduced and oxidized Fc-Lip as the system is stretched. Note, only the central portion of the system is shown for clarity. (d) Potential

energy surfaces showing the actual changes in energy of reduced (blue) and oxidised (red) Fc-Lip for stretching between atoms S1 and S2. Energies are given relative to the global minimum (ring substituents at ~72˚) for each oxidation state. Equations for quadratic fits to the data are shown. (e) Changes in the adiabatic ionization potential (aIP) of Fc-Lip as the S1-S2 distance is increased. Values are given relative to the aIP for the system when no structural constraints are applied. In (d) and (e), a stretching distance of 27.93 Å corresponds to an applied force sufficient to cleave an Au-Au bond in the reduced form (black dash line), and hence break the junction. Stretching distances beyond this are shaded blue shaded to indicate that they are inaccessible.

Table 3.2 Spring Constants and Shifts in Gibbs Free Energy Calculated from the Vibrational Frequencies of Dimethyl Ferrocene Obtained by IR Spectroscopy and DFT Calculations, Using Reduced Mass Values Obtained from DFT Calculation. Both Cp-Fe-Cp Symmetric Stretching Mode and Symmetric Tilting Mode are Discussed.

	ν_{red} (cm^{-1})	ν_{ox} (cm^{-1})	μ_{red} (amu)	μ_{ox} (amu)	k_{red} (N/m)	k_{ox} (N/m)	ΔG_0 (mV)
Stretching(IR)	309	304	4.2	4.8	23.3	26.0	-25
Tilting(IR)	402	406	4.0	4.1	38.5	39.5	-51
Stretching(DFT)	325	296	4.2	4.8	25.8	24.7	-69
Tilting(DFT)	392	385	4.0	4.1	36.6	35.5	-62

3.6 Other Supporting Data and Discussions

3.6.1 The discrete levels of conductance at different gate potential

It is noticeable that two discrete conductance levels were observed in the present work, corresponding to the reduced and oxidized states, respectively. In some redox molecules, there is a gradual change in the conductance as one sweeps the potential from the reduced to the oxidized states[57, 162, 163]. We've also observed a gradual change in Ferrocene dicarboxylic acid (Fig. 3.10). One possible explanation for the two-state switching case in this paper is that it's a fast redox reaction[161] happening at a sterically stable ferrocene center, which is fixed by its relatively long, rigid side chains. Therefore, the abrupt change in redox center can be neatly captured by tunneling current as a two-state process.

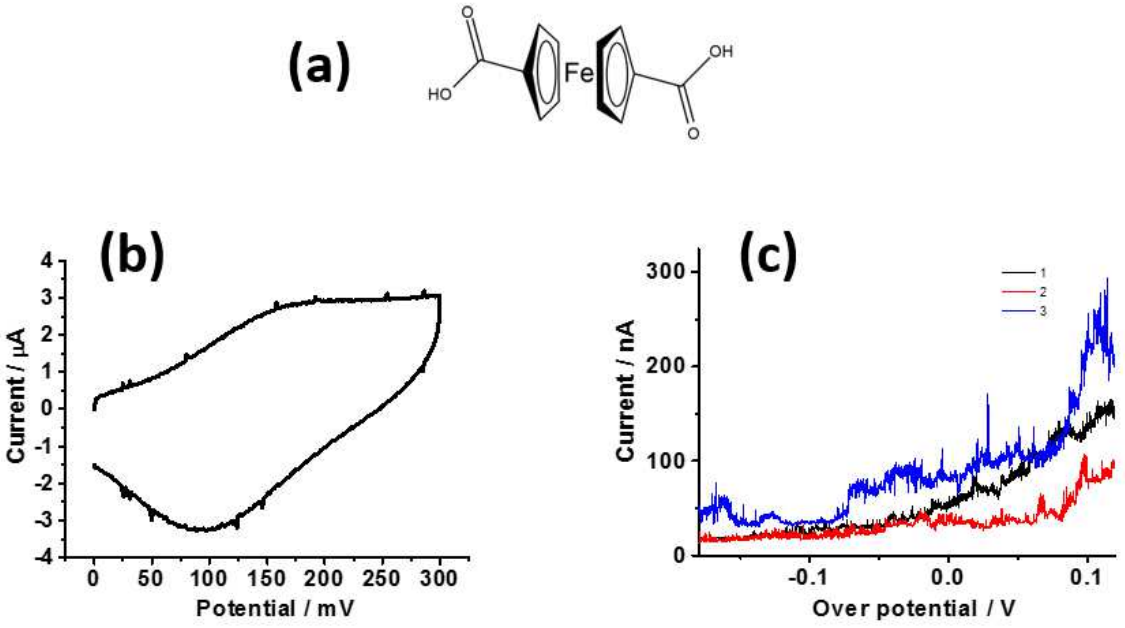


Figure 3.10 Structure and electrochemical calibration of Ferrocene dicarboxylic acid. (a) Chemical structure of Fc dicarboxylic acid. (b) Cyclic voltammetry of the SAM on a gold surface in 100 mM NaClO4 aqueous solution with Ag quasi-reference electrode and Pt counter electrode (sweeping rate 100mV/s). (c) Continuous feature of current V.S. electrochemical over potential in sweeps of gate voltage. Different colors represent different sweeps.

3.6.2 Conductance measurement of 1,1'-Ferrocenyl diester measured at -121 mV

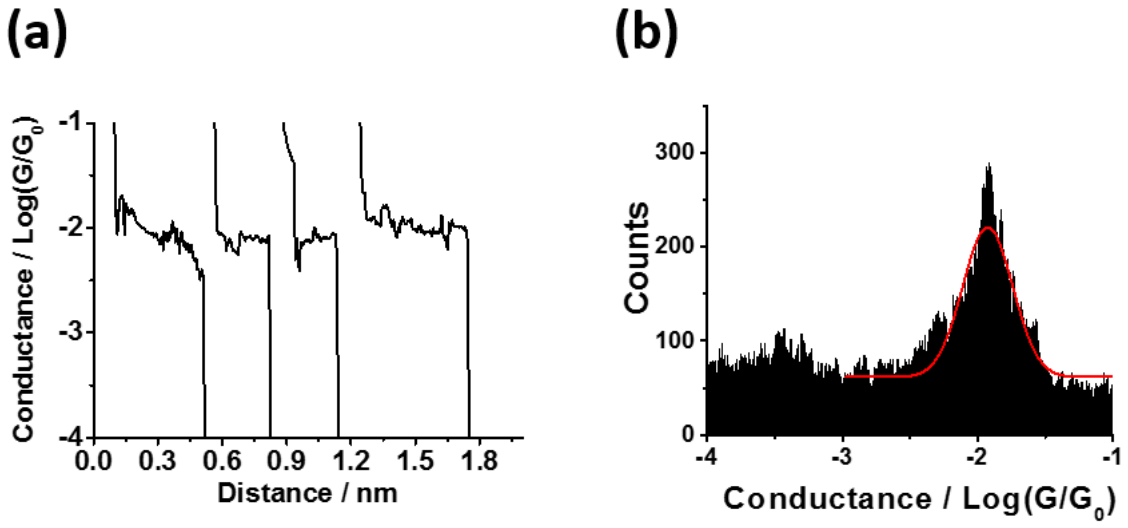


Figure 3.11 Conductance measurement of 1,1'-Ferrocenyl diester measured at overpotential of -121 mV. (a) Individual decay curves. (b) Conductance histogram. Red curve is Gaussian fitting of the conductance peak.

3.6.3 Conductance at different stretching distance for all curves at overpotential of +30 mV

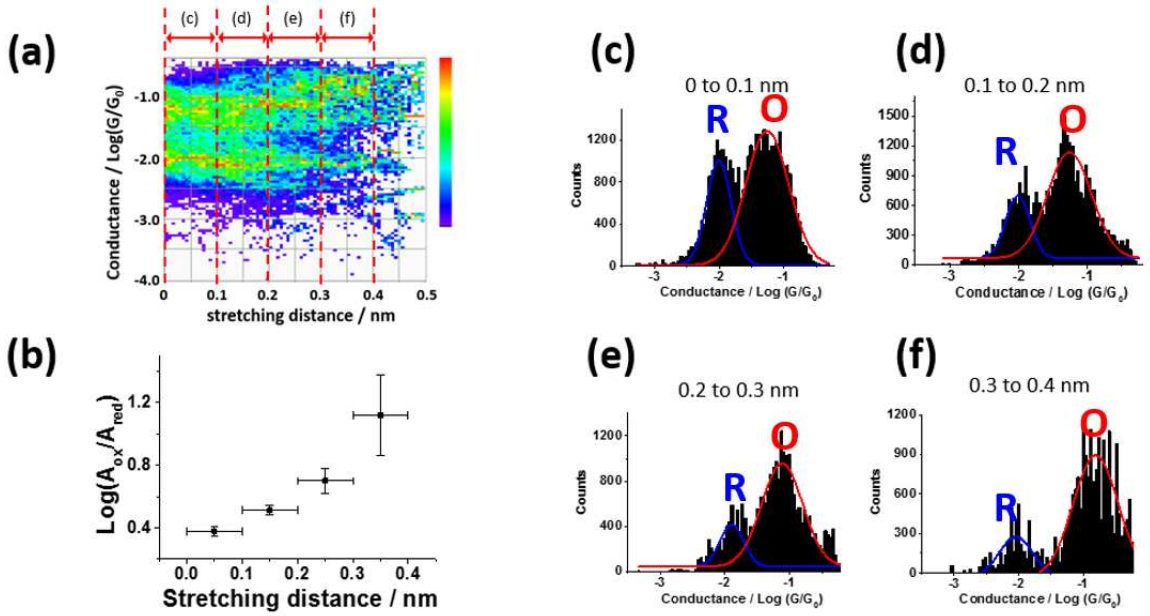


Figure 3.12 Conductance at different stretching distance for all curves at overpotential of +30 mV. (a) The conductance V.S. stretching distance 2D histograms of all curves (normalized at each distance). Between red dashed lines are slices with a width of 0.1 nm to build conductance histograms. (b) Logarithm ratio of the peak area of oxidized and reduced conductance peaks at different distance (x errors represent the range of distance included, y errors are from the error of peak area fitting), which comes from the conductance histograms of slices in the 2D histogram at (c) 0-0.1 nm, (d) 0.1-0.2 nm, (e) 0.2-0.3 nm and (f) 0.3-0.4 nm. Red and blue curves show Gaussian fittings of the higher and lower conductance peaks.

3.6.4 Relationship between conductance peak area and surface coverage of redox species.

In a conductance histogram, *S*, the area of the conductance peak for single molecular junction can be expressed by[78],

$$S = n_j \cdot \frac{Lf}{vU}, \qquad (3.5)$$

where n_j is the number of molecular junctions (traces with plateau), L is the plateau length of the plateau, f is the sampling frequency, v is the pulling rate in nm/s and U is the number of bins in the conductance histogram. For the non-switched curves, the plateau length L for the two conductance states are the same (Fig. 3.4), and the f, v, and U are kept the same for each experiment. Thus the peak area S is proportional to the number of molecular junctions, n_j. Because the oxidized state and reduced state of 1,1'-Ferrocenyl diester are measured under exactly the same circumstances, and their structures are only differed by the Ferrocene moiety, I believe that their yield of forming molecular junctions are proportional to the surface coverage of the species. For the switched curves, the average plateau length L at either redox state is assumed to be proportional to the probability of that state. Therefore, ideally the peak area, S is proportional to the surface coverage of species.

3.6.5 Theoretical description of the stretching process

Fig. 3.13 shows the potential energy surface (PES) for both species from DFT calculation. Fitting the curve with quadratic functions allows the force constant for the reduced species to be estimated as 11.6 N/m. For the stretching process, the start point is determined by the minimum in the fitted curve, which is 2.67 nm for reduced species. Therefore, at the breakdown force of 1.5 nN, d(S1-S2) is stretched by 0.13 nm, and the corresponding stretching distance of the Ferrocene moiety (C1-C9) is stretched by 0.019 nm according to the bond length profile in Fig. 3.14. At this critical point, the theory predicts that the adiabatic ionisation potential of the reduced species drops by 0.06 eV compared with an un-stretched molecule.

For the reduced species, the conformation with the two substituents at 64° was found to be the most stable. We find another conformation with the two substituents at 138° being a local minimum with only 1.4 kJ mol^{-1} higher in energy. For oxidized species, the conformations for the global minimum and local minimum are with the two substituents at 66° and 141°, respectively, with 2.1 kJ mol^{-1} energy difference. The energies of the most stable conformation for each species were used as the reference values for the stretching potential energy surfaces (PESs) and their relative energy (the fully adiabatic ionisation potential) as the reference value for Figure 3.9d.

The difference in aIP between the conformations corresponding to the global minimum and local minimum was only 0.007 eV. This indicates that relative twisting of Cp rings between these two dihedral angle values is not contributing to the experimentally

observed redox potential changes. Therefore, for simplicity, the scan of the aIP changes with stretching was started from the 138° local minimum structure.

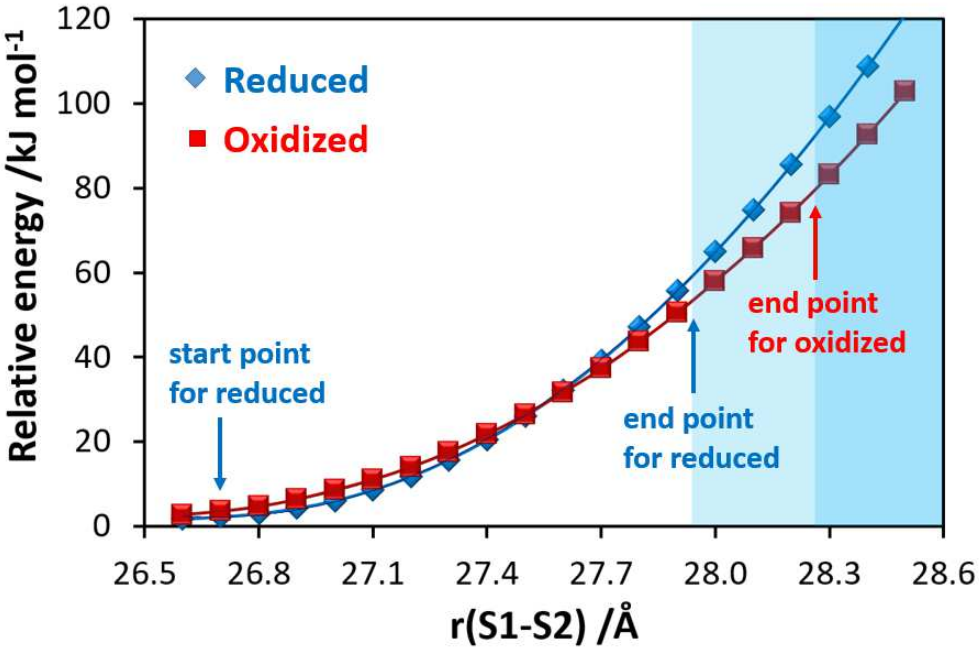
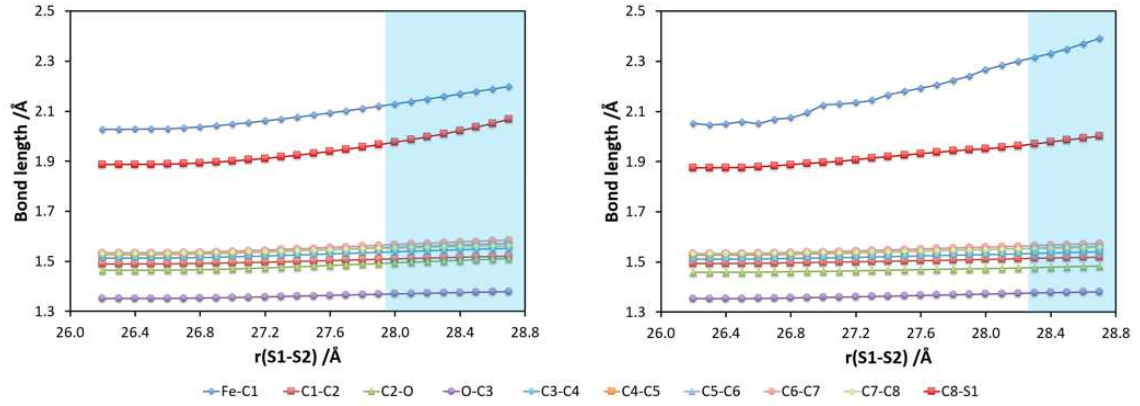
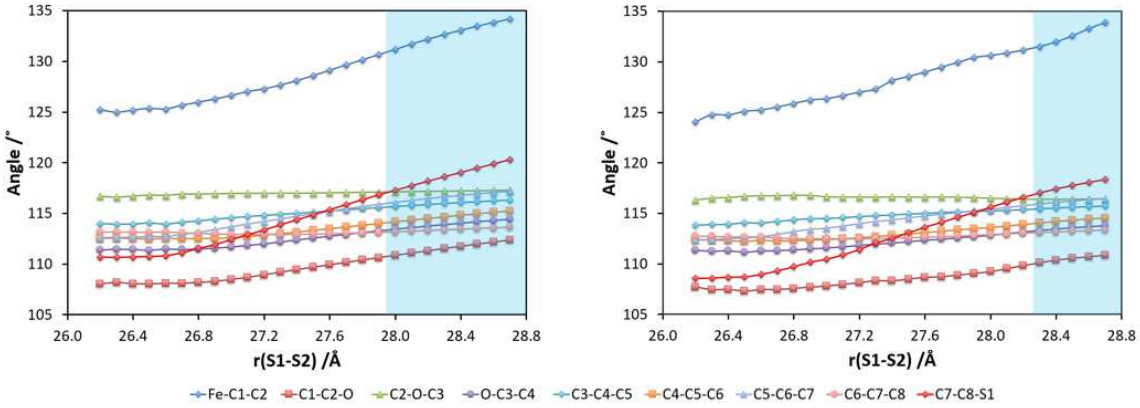


Figure 3.13 Potential energy surfaces for stretching between atoms S1 and S2 in the reduced(blue) and oxidised(red) species. Energies are given relative to the global minimum (ring substituents at ~72˚) for each oxidation state. Equations for quadratic fits to the data are shown. The blue shaded regions correspond to stretching distances where the force applied would be sufficient to cleave an Au-Au bond and hence break the junction. Light blue corresponds to the reduced species and darker blue to both oxidation states.

Reduced Oxidized





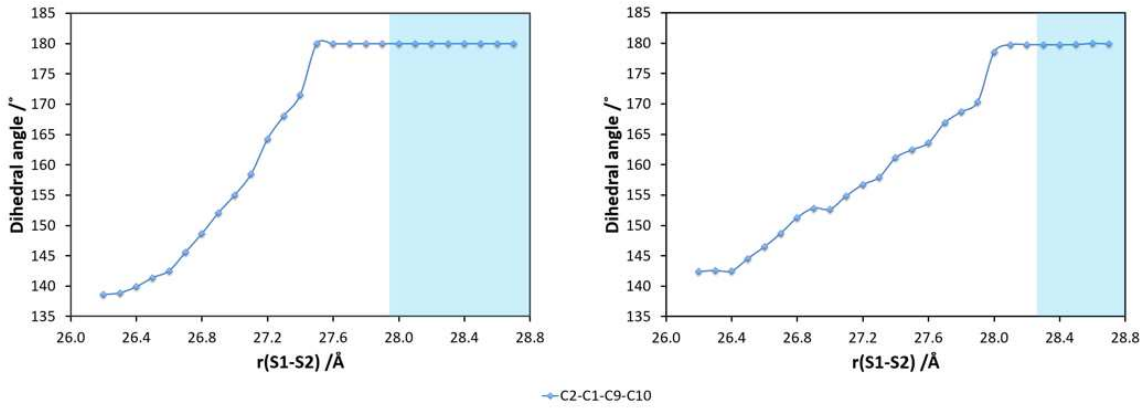


Figure 3.14 Changes in significant structural parameters of the reduced and oxidized species as the S1-S2 distance is increased. See Figure 3.9a for atom labels. Shaded regions corresponds to stretching distances where the force applied would be sufficient to cleave an Au-Au bond and hence break the junction for the relevant species.

3.7 Conclusions

Our study demonstrates that a mechanical force can induce redox reactions in single molecules. The force changes the bond length and drives the reaction towards the final state that favors the bond length change. That observation supports that structural-electronic coupling is responsible for redox reactions. The phenomenon that a mechanical force can control redox states of a single molecule also provides a way to mechanically switching the electronic properties of a single molecule, which supports the vision of molecular machines with electromechanical functions[170].

4 CONCLUSIONS AND PERSPECTIVES

In the past two decades, single molecular devices have been built with various methods and proved to have enourmous new and interesting functionalities. Although there's still a long way from application for real-world problems, molecular electronics has already displayed its potential in understanding the charge transport mechanism in basic chemical reactions and biological systems. This thesis has demonstrated two examples of how the charge transport in single molecule can be tuned by temperature gradient and mechanical force, for which the understanding and utilization of these uique properties are equally important.

First, the thermoelectric effect in single DNA molecules was reported. From the conductance measurements, it is determined that for DNA sequences with repeating CG base pair units, represented by $A(CG)_nT$, the charge transport happens via thermally activated sequential hopping, while for sequences with repeating AT base pair units, i.e. $ACGC(AT)_mGCGT$ and $ACGC(AT)_{m-1}AGCGT$, the charge transport is mediated by tunneling for shorter AT blocks ($m \leq 2$) and hopping for longer AT blocks ($m>2$). Then the thermoelectric measurement carried out by rapid I-V method reveals that low thermoelectric effect is displayed for all sequences with hopping charge transport mechanism, and relatively high Seebeck coefficient is found for sequences with an AT tunneling barrier in the middle. Further theoretical studies confirmed the conclusion that different charge transport mechanism is the reason for the gap in thermoelectricity. This phenomenon should potentially impact the basic understanding of the thermoelectric

effect in mesoscopic scale, and also provide critical information for the future programable DNA devices. However at the same time, I have to realize and admit that the understanding of the energy interplay in this phenomenon is far from enough. It is concluded that hopping shows much lower Seebeck coefficient than tunneling, but no clear explanation is proposed. Actually it would be an interesting and important project to find out in which process of the charge hopping that the thermoelectric effect vanishes. A wider study of similar systems and deeper investigation into the decisive reason will definitely enables the wide application of this unique property.

Then, the force induced electron transfer reaction featured with conductance switching in redox molecules was demonstrated. In the gate sweeping and basic conductance measurement at static gate potentials, two discrete conductance levels are revealed for the two redox states, lower conductance for reduced states and higher conductance for oxidiazed states. Particularlly, the conductance decay curves measured at about redox potential frequently swithch up from lower to higher conductance level, suggesting that the stretching force from the tip retraction causes oxidation of Fc-Lip. The logarithm ratio of the reduced and oxidized conductance peak areas at different distances confirms the assumption that mechanical force can change the redox potential, thus oxidizing the Fc-Lip at a more negative potential. A negative shift by 34 mV of redox potential is shown for 0.3 nm stretching of the molecular junction. The redox potential shift was explained by the change in Gibb's free energy for both redox states resulting from the force tilted energy landscape. And the difference in the force induced change in Gibb's free energy for reduced and oxidized states comes from the difference

of 0.003 nm in the distance between Fe atom and the Cp ring of reduced and oxidized Fc-Lip. In this way, the force induced change in redox potential is shown to be origined from the inherent structural difference between the redox states of the bridged molecule. The above phenomenon demonstrates a powerful way of doing single molecule mechanochemistry, and provides insights into the interplay between mechanical force and redox reaction. Inspired by this work, many different redox systems can be measured to test for how the redox potential is changing in react with mechanical force, and how the change is related with the structural difference between the redox states. Another unique feature from the described experiment is the discrete levels of conductance for the redox states, which is distinct from other systems with a gradual changing conductance from one redox state to the other. This phenomenon, as well, can be further studied in terms of length dependence, electrolyte dependence and temperature dependence, which may unravel new, important charge transport properties in the future.

REFERENCES

1. Aviram A, Ratner MA. Molecular rectifiers. *Chemical Physics Letters* 1974, **29**(2)**:** 277-283.

2. Smit RHM, Noat Y, Untiedt C, Lang ND, van Hemert MC, van Ruitenbeek JM. Measurement of the conductance of a hydrogen molecule. *Nature* 2002, **419**(6910)**:** 906-909.

3. Reed MA, Zhou C, Muller CJ, Burgin TP, Tour JM. Conductance of a Molecular Junction. *Science* 1997, **278**(5336)**:** 252.

4. Reed MA, Zhou C, Deshpande MR, Muller CJ, Burgin TP, Jones L*, et al.* The Electrical Measurement of Molecular Junctions. *Annals of the New York Academy of Sciences* 1998, **852**(1)**:** 133-144.

5. Blum AS, Kushmerick JG, Long DP, Patterson CH, Yang JC, Henderson JC*, et al.* Molecularly inherent voltage-controlled conductance switching. *Nat Mater* 2005, **4**(2)**:** 167-172.

6. Kushmerick JG, Holt DB, Pollack SK, Ratner MA, Yang JC, Schull TL*, et al.* Effect of Bond-Length Alternation in Molecular Wires. *Journal of the American Chemical Society* 2002, **124**(36)**:** 10654-10655.

7. Kim, Beebe JM, Olivier C, Rigaut S, Touchard D, Kushmerick JG*, et al.* Temperature and Length Dependence of Charge Transport in Redox-Active Molecular Wires Incorporating Ruthenium(II) Bis(σ-arylacetylide) Complexes. *The Journal of Physical Chemistry C* 2007, **111**(20)**:** 7521-7526.

8. Anariba F, McCreery RL. Electronic Conductance Behavior of Carbon-Based Molecular Junctions with Conjugated Structures. *The Journal of Physical Chemistry B* 2002, **106**(40)**:** 10355-10362.

9. Slowinski K, Fong HKY, Majda M. Mercury−Mercury Tunneling Junctions. 1. Electron Tunneling Across Symmetric and Asymmetric Alkanethiolate Bilayers. *Journal of the American Chemical Society* 1999, **121**(31)**:** 7257-7261.

10. Holmlin RE, Haag R, Chabinyc ML, Ismagilov RF, Cohen AE, Terfort A*, et al.* Electron Transport through Thin Organic Films in Metal−Insulator−Metal Junctions Based on Self-Assembled Monolayers [J. Am. Chem. Soc. 2001, 123, 5075−5085]. *Journal of the American Chemical Society* 2002, **124**(29)**:** 8762-8762.

11. Xu B, Tao NJ. Measurement of Single-Molecule Resistance by Repeated Formation of Molecular Junctions. *Science* 2003, **301**(5637)**:** 1221-1223.

12. Venkataraman L, Klare JE, Nuckolls C, Hybertsen MS, Steigerwald ML. Dependence of single-molecule junction conductance on molecular conformation. *Nature* 2006, **442**(7105)**:** 904-907.

13. Haiss W, van Zalinge H, Higgins SJ, Bethell D, Höbenreich H, Schiffrin DJ*, et al.* Redox State Dependence of Single Molecule Conductivity. *Journal of the American Chemical Society* 2003, **125**(50)**:** 15294-15295.

14. Leatherman G, Durantini EN, Gust D, Moore TA, Moore AL, Stone S*, et al.* Carotene as a Molecular Wire: Conducting Atomic Force Microscopy. *The Journal of Physical Chemistry B* 1999, **103**(20)**:** 4006-4010.

15. Cui XD, Primak A, Zarate X, Tomfohr J, Sankey OF, Moore AL*, et al.* Reproducible Measurement of Single-Molecule Conductivity. *Science* 2001, **294**(5542)**:** 571.

16. Kelley TW, Granstrom E, Frisbie CD. Conducting Probe Atomic Force Microscopy: A Characterization Tool for Molecular Electronics. *Advanced Materials* 1999, **11**(3)**:** 261-264.

17. Li X, He J, Hihath J, Xu B, Lindsay SM, Tao N. Conductance of Single Alkanedithiols: Conduction Mechanism and Effect of Molecule−Electrode Contacts. *Journal of the American Chemical Society* 2006, **128**(6)**:** 2135-2141.

18. Chen F, Li X, Hihath J, Huang Z, Tao N. Effect of Anchoring Groups on Single-Molecule Conductance: Comparative Study of Thiol-, Amine-, and Carboxylic-Acid-Terminated Molecules. *Journal of the American Chemical Society* 2006, **128**(49)**:** 15874-15881.

19. Díez-Pérez I, Hihath J, Lee Y, Yu L, Adamska L, Kozhushner MA*, et al.* Rectification and stability of a single molecular diode with controlled orientation. *Nat Chem* 2009, **1**(8)**:** 635-641.

20. Capozzi B, Xia J, Adak O, Dell EJ, Liu Z-F, Taylor JC*, et al.* Single-molecule diodes with high rectification ratios through environmental control. *Nat Nano* 2015, **10**(6)**:** 522-527.

21. Elbing M, Ochs R, Koentopp M, Fischer M, von Hänisch C, Weigend F*, et al.* A single-molecule diode. *Proceedings of the National Academy of Sciences of the United States of America* 2005, **102**(25)**:** 8815-8820.

22. Gittins DI, Bethell D, Schiffrin DJ, Nichols RJ. A nanometre-scale electronic switch consisting of a metal cluster and redox-addressable groups. *Nature* 2000, **408**(6808)**:** 67-69.

23. Donhauser ZJ, Mantooth BA, Kelly KF, Bumm LA, Monnell JD, Stapleton JJ*, et al.* Conductance Switching in Single Molecules Through Conformational Changes. *Science* 2001, **292**(5525)**:** 2303.

24. Moreno-García P, La Rosa A, Kolivoška V, Bermejo D, Hong W, Yoshida K*, et al.* Charge Transport in C60-Based Dumbbell-type Molecules: Mechanically Induced Switching between Two Distinct Conductance States. *Journal of the American Chemical Society* 2015, **137**(6)**:** 2318-2327.

25. Park H, Park J, Lim AKL, Anderson EH, Alivisatos AP, McEuen PL. Nanomechanical oscillations in a single-C60 transistor. *Nature* 2000, **407**(6800)**:** 57-60.

26. Diez-Perez I, Li Z, Hihath J, Li J, Zhang C, Yang X*, et al.* Gate-controlled electron transport in coronenes as a bottom-up approach towards graphene transistors. *Nature Communications* 2010, **1:** 31.

27. Osorio HM, Catarelli S, Cea P, Gluyas JBG, Hartl F, Higgins SJ*, et al.* Electrochemical Single-Molecule Transistors with Optimized Gate Coupling. *Journal of the American Chemical Society* 2015, **137**(45)**:** 14319-14328.

28. Reddy P, Jang S-Y, Segalman RA, Majumdar A. Thermoelectricity in Molecular Junctions. *Science* 2007, **315**(5818)**:** 1568-1571.

29. Widawsky JR, Darancet P, Neaton JB, Venkataraman L. Simultaneous Determination of Conductance and Thermopower of Single Molecule Junctions. *Nano Letters* 2012, **12**(1)**:** 354-358.

30. Guo S, Zhou G, Tao N. Single Molecule Conductance, Thermopower, and Transition Voltage. *Nano Letters* 2013, **13**(9)**:** 4326-4332.

31. Bruot C, Hihath J, Tao N. Mechanically controlled molecular orbital alignment in single molecule junctions. *Nat Nano* 2012, **7**(1)**:** 35-40.

32. Rascón-Ramos H, Artés JM, Li Y, Hihath J. Binding configurations and intramolecular strain in single-molecule devices. *Nat Mater* 2015, **14**(5)**:** 517-522.

33. Xiang L, Palma JL, Bruot C, Mujica V, Ratner MA, Tao N. Intermediate tunnelling–hopping regime in DNA charge transport. *Nat Chem* 2015, **7**(3)**:** 221-226.

34. Bruot C, Xiang L, Palma JL, Li Y, Tao N. Tuning the Electromechanical Properties of Single DNA Molecular Junctions. *Journal of the American Chemical Society* 2015, **137**(43)**:** 13933-13937.

35. Li Y, Xiang L, Palma JL, Asai Y, Tao N. Thermoelectric effect and its dependence on molecular length and sequence in single DNA molecules. *Nature Communications* 2016, **7:** 11294.

36. Bruot C, Palma JL, Xiang L, Mujica V, Ratner MA, Tao N. Piezoresistivity in single DNA molecules. *Nature Communications* 2015, **6:** 8032.

37. Bruot C, Xiang L, Palma JL, Tao N. Effect of Mechanical Stretching on DNA Conductance. *ACS Nano* 2015, **9**(1)**:** 88-94.

38. Li Y, Artés JM, Hihath J. Long-Range Charge Transport in Adenine-Stacked RNA:DNA Hybrids. *Small* 2016, **12**(4)**:** 432-437.

39. Li Y, Artés JM, Qi J, Morelan IA, Feldstein P, Anantram MP*, et al.* Comparing Charge Transport in Oligonucleotides: RNA:DNA Hybrids and DNA Duplexes. *The Journal of Physical Chemistry Letters* 2016, **7**(10)**:** 1888-1894.

40. Artés JM, Díez-Pérez I, Gorostiza P. Transistor-like Behavior of Single Metalloprotein Junctions. *Nano Letters* 2012, **12**(6)**:** 2679-2684.

41. Artés JM, López-Martínez M, Giraudet A, Díez-Pérez I, Sanz F, Gorostiza P. Current–Voltage Characteristics and Transition Voltage Spectroscopy of Individual Redox Proteins. *Journal of the American Chemical Society* 2012, **134**(50)**:** 20218-20221.

42. Landauer R. Spatial Variation of Currents and Fields Due to Localized Scatterers in Metallic Conduction. *IBM Journal of Research and Development* 1957, **1**(3)**:** 223-231.

43. Büttiker M, Imry Y, Landauer R, Pinhas S. Generalized many-channel conductance formula with application to small rings. *Physical Review B* 1985, **31**(10)**:** 6207-6215.

44. Joachim C, Ratner MA. Molecular electronics: Some views on transport junctions and beyond. *Proceedings of the National Academy of Sciences of the United States of America* 2005, **102**(25)**:** 8801-8808.

45. Metzger RM. Unimolecular Electronics. *Chemical Reviews* 2015, **115**(11)**:** 5056-5115.

46. Sedghi G, Esdaile LJ, Anderson HL, Martin S, Bethell D, Higgins SJ*, et al.* Comparison of the Conductance of Three Types of Porphyrin-Based Molecular Wires: β,meso,β-Fused Tapes, meso-Butadiyne-Linked and Twisted meso-meso Linked Oligomers. *Advanced Materials* 2012, **24**(5)**:** 653-657.

47. Ho Choi S, Kim B, Frisbie CD. Electrical Resistance of Long Conjugated Molecular Wires. *Science* 2008, **320**(5882)**:** 1482.

48. Haiss W, Martin S, Scullion LE, Bouffier L, Higgins SJ, Nichols RJ. Anomalous length and voltage dependence of single molecule conductance. *Physical Chemistry Chemical Physics* 2009, **11**(46)**:** 10831-10838.

49. Luo L, Choi SH, Frisbie CD. Probing Hopping Conduction in Conjugated Molecular Wires Connected to Metal Electrodes. *Chemistry of Materials* 2011, **23**(3)**:** 631-645.

50. Nitzan A. The relationship between electron transfer rate and molecular conduction 2. The sequential hopping case. *Israel Journal of Chemistry* 2002, **42**(2-3)**:** 163-166.

51. Trouwborst ML, Martin CA, Smit RHM, Guédon CM, Baart TA, van der Molen SJ*, et al.* Transition Voltage Spectroscopy and the Nature of Vacuum Tunneling. *Nano Letters* 2011, **11**(2)**:** 614-617.

52. Generalized Formula for the Electric Tunnel Effect between Similar Electrodes Separated by a Thin Insulating Film. *Journal of Applied Physics* 1963, **34**(6)**:** 1793-1803.

53. Porath D, Bezryadin A, de Vries S, Dekker C. Direct measurement of electrical transport through DNA molecules. *Nature* 2000, **403**(6770)**:** 635-638.

54. Shimazaki T, Asai Y. Bias voltage dependence on the vibronic electric current. *Physical Review B* 2008, **77**(7)**:** 075110.

55. Jaklevic RC, Lambe J. Molecular Vibration Spectra by Electron Tunneling. *Physical Review Letters* 1966, **17**(22)**:** 1139-1140.

56. Beebe JM, Moore HJ, Lee TR, Kushmerick JG. Vibronic Coupling in Semifluorinated Alkanethiol Junctions: Implications for Selection Rules in Inelastic Electron Tunneling Spectroscopy. *Nano Letters* 2007, **7**(5)**:** 1364-1368.

57. Zhihai L, Ilya P, Bo H, Thomas W, Alfred B, Marcel M. Conductance of redox-active single molecular junctions: an electrochemical approach. *Nanotechnology* 2007, **18**(4)**:** 044018.

58. Giese B, Amaudrut J, Kohler A-K, Spormann M, Wessely S. Direct observation of hole transfer through DNA by hopping between adenine bases and by tunnelling. *Nature* 2001, **412**(6844)**:** 318-320.

59. Lewis FD, Wu T, Zhang Y, Letsinger RL, Greenfield SR, Wasielewski MR. Distance-Dependent Electron Transfer in DNA Hairpins. *Science* 1997, **277**(5326)**:** 673.

60. Lewis FD, Letsinger RL, Wasielewski MR. Dynamics of Photoinduced Charge Transfer and Hole Transport in Synthetic DNA Hairpins. *Accounts of Chemical Research* 2001, **34**(2)**:** 159-170.

61. Lewis FD, Zhu H, Daublain P, Cohen B, Wasielewski MR. Hole Mobility in DNA A Tracts. *Angewandte Chemie International Edition* 2006, **45**(47)**:** 7982-7985.

62. Kelley SO, Jackson NM, Hill MG, Barton JK. Long-Range Electron Transfer through DNA Films. *Angewandte Chemie International Edition* 1999, **38**(7)**:** 941-945.

63. Arnold Anna R, Grodick Michael A, Barton Jacqueline K. DNA Charge Transport: from Chemical Principles to the Cell. *Cell Chemical Biology*, **23**(1)**:** 183-197.

64. Pheeney CG, Barton JK. DNA Electrochemistry with Tethered Methylene Blue. *Langmuir* 2012, **28**(17)**:** 7063-7070.

65. Laviron E. General expression of the linear potential sweep voltammogram in the case of diffusionless electrochemical systems. *Journal of Electroanalytical Chemistry and Interfacial Electrochemistry* 1979, **101**(1)**:** 19-28.

66. Cohen H, Nogues C, Naaman R, Porath D. Direct measurement of electrical transport through single DNA molecules of complex sequence. *Proceedings of the National Academy of Sciences of the United States of America* 2005, **102**(33)**:** 11589-11593.

67. Xu, Zhang, Li, Tao. Direct Conductance Measurement of Single DNA Molecules in Aqueous Solution. *Nano Letters* 2004, **4**(6)**:** 1105-1108.

68. Risser SM, Beratan DN, Meade TJ. Electron transfer in DNA: predictions of exponential growth and decay of coupling with donor-acceptor distance. *Journal of the American Chemical Society* 1993, **115**(6)**:** 2508-2510.

69. Jortner J, Bixon M, Langenbacher T, Michel-Beyerle ME. Charge transfer and transport in DNA. *Proceedings of the National Academy of Sciences* 1998, **95**(22)**:** 12759-12765.

70. Conwell EM. Charge transport in DNA in solution: The role of polarons. *Proceedings of the National Academy of Sciences of the United States of America* 2005, **102**(25)**:** 8795-8799.

71. Renaud N, Berlin YA, Lewis FD, Ratner MA. Between Superexchange and Hopping: An Intermediate Charge-Transfer Mechanism in Poly(A)-Poly(T) DNA Hairpins. *Journal of the American Chemical Society* 2013, **135**(10)**:** 3953-3963.

72. Roche S. Sequence Dependent DNA-Mediated Conduction. *Physical Review Letters* 2003, **91**(10)**:** 108101.

73. Wang XF, Chakraborty T. Charge Transfer via a Two-Strand Superexchange Bridge in DNA. *Physical Review Letters* 2006, **97**(10)**:** 106602.

74. Park J, Pasupathy AN, Goldsmith JI, Chang C, Yaish Y, Petta JR*, et al.* Coulomb blockade and the Kondo effect in single-atom transistors. *Nature* 2002, **417**(6890)**:** 722-725.

75. Kasibhatla BST, Labonté AP, Zahid F, Reifenberger RG, Datta S, Kubiak CP. Reversibly Altering Electronic Conduction through a Single Molecule by a Chemical Binding Event. *The Journal of Physical Chemistry B* 2003, **107**(45)**:** 12378-12382.

76. Artés JM, López-Martínez M, Díez-Pérez I, Sanz F, Gorostiza P. Conductance Switching in Single Wired Redox Proteins. *Small* 2014, **10**(13)**:** 2537-2541.

77. Baghernejad M, Zhao X, Baruël Ørnsø K, Füeg M, Moreno-García P, Rudnev AV*, et al.* Electrochemical Control of Single-Molecule Conductance by Fermi-Level

Tuning and Conjugation Switching. *Journal of the American Chemical Society* 2014, **136**(52)**:** 17922-17925.

78. Arielly R, Vadai M, Kardash D, Noy G, Selzer Y. Real-Time Detection of Redox Events in Molecular Junctions. *Journal of the American Chemical Society* 2014, **136**(6)**:** 2674-2680.

79. Xiao X, Brune D, He J, Lindsay S, Gorman CB, Tao N. Redox-gated electron transport in electrically wired ferrocene molecules. *Chemical Physics* 2006, **326**(1)**:** 138-143.

80. Migliore A, Nitzan A. Irreversibility in redox molecular conduction: single versus double metal-molecule interfaces. *Electrochimica Acta* 2015, **160:** 363-375.

81. A. D. McNaught AW. *IUPAC Compendium of Chemical Technology, (the "Gold Book")*, 2nd edn. Blackwell Scientific Publications: Oxford, 1997.

82. Boldyrev V. Experimental Methods in the Mechanochemistry of Inorganic Solids. In: Herbert H (ed). *Treatise on Materials Science & Technology*, vol. Volume 19, Part B. Elsevier, 1983, pp 185-223.

83. Balaz P, Achimovicova M, Balaz M, Billik P, Cherkezova-Zheleva Z, Criado JM*, et al.* Hallmarks of mechanochemistry: from nanoparticles to technology. *Chemical Society Reviews* 2013, **42**(18)**:** 7571-7637.

84. Rief M, Gautel M, Oesterhelt F, Fernandez JM, Gaub HE. Reversible Unfolding of Individual Titin Immunoglobulin Domains by AFM. *Science* 1997, **276**(5315)**:** 1109.

85. Ashkin A, Dziedzic JM, Bjorkholm JE, Chu S. Observation of a single-beam gradient force optical trap for dielectric particles. *Opt Lett* 1986, **11**(5)**:** 288-290.

86. Lundbæk JA, Collingwood SA, Ingólfsson HI, Kapoor R, Andersen OS. Lipid bilayer regulation of membrane protein function: gramicidin channels as molecular force probes. *Journal of the Royal Society Interface* 2010, **7**(44)**:** 373-395.

87. Wiggins KM, Brantley JN, Bielawski CW. Polymer Mechanochemistry: Force Enabled Transformations. *ACS Macro Letters* 2012, **1**(5)**:** 623-626.

88. Wiita AP, Perez-Jimenez R, Walther KA, Grater F, Berne BJ, Holmgren A*, et al.* Probing the chemistry of thioredoxin catalysis with force. *Nature* 2007, **450**(7166)**:** 124-127.

89. Baldus Ilona B, Gräter F. Mechanical Force Can Fine-Tune Redox Potentials of Disulfide Bonds. *Biophysical Journal* 2012, **102**(3)**:** 622-629.

90. Dopieralski P, Ribas-Arino J, Anjukandi P, Krupicka M, Kiss J, Marx D. The Janus-faced role of external forces in mechanochemical disulfide bond cleavage. *Nat Chem* 2013, **5**(8)**:** 685-691.

91. Lu H, Isralewitz B, Krammer A, Vogel V, Schulten K. Unfolding of titin immunoglobulin domains by steered molecular dynamics simulation. *Biophysical Journal* 1998, **75**(2)**:** 662-671.

92. Wang MD, Yin H, Landick R, Gelles J, Block SM. Stretching DNA with optical tweezers. *Biophysical Journal* 1997, **72**(3)**:** 1335-1346.

93. Kauzmann W, Eyring H. The Viscous Flow of Large Molecules. *Journal of the American Chemical Society* 1940, **62**(11)**:** 3113-3125.

94. Kochhar GS, Heverly-Coulson GS, Mosey NJ. Theoretical Approaches for Understanding the Interplay Between Stress and Chemical Reactivity. In: Boulatov R (ed). *Polymer Mechanochemistry*. Springer International Publishing: Cham, 2015, pp 37-96.

95. Bell GI. Models for the specific adhesion of cells to cells. *Science* 1978, **200**(4342)**:** 618.

96. Xu B, Xiao X, Tao NJ. Measurements of Single-Molecule Electromechanical Properties. *Journal of the American Chemical Society* 2003, **125**(52)**:** 16164-16165.

97. Frei M, Aradhya SV, Hybertsen MS, Venkataraman L. Linker Dependent Bond Rupture Force Measurements in Single-Molecule Junctions. *Journal of the American Chemical Society* 2012, **134**(9)**:** 4003-4006.

98. Aradhya SV, Frei M, Hybertsen MS, Venkataraman L. Van der Waals interactions at metal/organic interfaces at the single-molecule level. *Nat Mater* 2012, **11**(10)**:** 872-876.

99. Frei M, Aradhya SV, Koentopp M, Hybertsen MS, Venkataraman L. Mechanics and Chemistry: Single Molecule Bond Rupture Forces Correlate with Molecular Backbone Structure. *Nano Letters* 2011, **11**(4)**:** 1518-1523.

100. Mahan GD, Sofo JO. The best thermoelectric. *Proc Natl Acad Sci U S A* 1996, **93**(15)**:** 7436-7439.

101. Dubi Y, Di Ventra M. Thermoelectric effects in nanoscale junctions. *Nano Lett* 2009, **9:** 97-101.

102. Bergfield JP, Stafford CA. Thermoelectric signatures of coherent transport in single-molecule heterojunctions. *Nano Lett* 2009, **9:** 3072-3076.

103. Ke SH, Yang M, Curtarolo S, Baranger HU. Thermopower of molecular junctions: an ab initio study. *Nano Lett* 2009, **9:** 1011-1014.

104. Liu Y, Chen Y, Chen Y. Thermoelectric efficiency in nanojunctions: a comparison between atomic junctions and molecular junctions. *ACS Nano* 2009, **3:** 3497-3504.

105. Seeman NC. Nanomaterials Based on DNA. *Annu Rev Biochem* 2010, **79**(1)**:** 65-87.

106. Xiang L, Palma JL, Bruot C, Mujica V, Ratner MA, Tao N. Intermediate tunnelling–hopping regime in DNA charge transport. *Nat Chem* 2015, **7**(3)**:** 221-226.

107. Fukui K, Tanaka K. Distance dependence of photoinduced electron transfer in DNA. *Angew Chem, Int Ed Engl* 1998, **37**(1-2)**:** 158-161.

108. Kelley SO, Barton JK. Electron transfer between bases in double helical DNA. *Science (New York, NY)* 1999, **283**(5400)**:** 375-381.

109. Meade T, J, Katten J, F. Electron-transfer through DNA-site-specific modification of duplex DNA with Ruthenium donors and accepters. *Angew Chem, Int Ed Engl* 1995, **34**(3)**:** 352-354.

110. Meggers E, Kusch D, Spichty M, Wille U. Electron transfer through DNA in the course of radical-induced strand cleavage. *Angew Chem, Int Ed Engl* 1998, **37**(4)**:** 460-462.

111. Brun AM, Harriman A. Dynamics of electron transfer between intercalated polycyclic molecules: effect of interspersed bases. *J Am Chem Soc* 1992, **114**(10)**:** 3656-3660.

112. Giese B, Amaudrut J, Koehler A-K, Spormann M, Wessely S. Direct observation of hole transfer through DNA by hopping between adenine bases and by tunnelling. *Nature* 2001, **412**(6844)**:** 318-320.

113. Xu, Zhang, Li, Tao. Direct conductance measurement of sngle DNA molecules in aqueous solution. *Nano Lett* 2004, **4**(6)**:** 1105-1108.

114. Lewis FD, Zhu H, Daublain P, Cohen B, Wasielewski MR. Hole mobility in DNA a tracts. *Angew Chem, Int Ed Engl* 2006, **45**(47)**:** 7982-7985.

115. Jortner J, Bixon M, Voityuk AA, Rösch N. Superexchange mediated charge hopping in DNA. *J Phys Chem A* 2002, **106**(33)**:** 7599-7606.

116. Renaud N, Berlin YA, Lewis FD, Ratner MA. Between superexchange and hopping: an intermediate charge-transfer mechanism in Poly(A)-Poly(T) DNA hairpins. *J Am Chem Soc* 2013, **135**(10)**:** 3953-3963.

117. Troisi A, Orlandi G. The hole transfer in DNA: calculation of electron coupling between close bases. *Chem Phys Lett* 2001, **344**(5–6)**:** 509-518.

118. Williams PD, Reuter MG. Level Alignments and Coupling Strengths in Conductance Histograms: The Information Content of a Single Channel Peak. *J Phys Chem C* 2013, **117**(11)**:** 5937-5942.

119. Uchihashi T, Tanigawa M, Ashino M, Sugawara Y, Yokoyama K, Morita S*, et al.* Identification of B-Form DNA in an Ultrahigh Vacuum by Noncontact-Mode Atomic Force Microscopy. *Langmuir* 1999, **16**(3)**:** 1349-1353.

120. Tanaka H, Tanaka H, Kawai T. Partial sequencing of a single DNA molecule with a scanning tunnelling microscope. *Nat Nano* 2009, **4**(8)**:** 518-522.

121. Kang N. Electrical characterization of DNA in mechanically controlled break-junctions. *New J Phys* 2008, **10**(2)**:** 023030.

122. Brewer SH, Anthireya SJ, Lappi SE, Drapcho DL, Franzen S. Detection of DNA Hybridization on Gold Surfaces by Polarization Modulation Infrared Reflection Absorption Spectroscopy. *Langmuir* 2002, **18**(11)**:** 4460-4464.

123. McCreery RL. Molecular electronic junctions. *Chem Mater* 2004, **16**(23)**:** 4477-4496.

124. Luo L, Choi SH, Frisbie CD. Probing hopping conduction in conjugated molecular wires connected to metal electrodes. *Chem Mater* 2010, **23**(3)**:** 631-645.

125. Segal D, Nitzan A, Ratner M, Davis WB. Activated conduction in microscopic molecular junctions. *J Phys Chem B* 2000, **104**(13)**:** 2790-2793.

126. Nitzan A. The relationship between electron transfer rate and molecular conduction 2. The sequential hopping case. *Isr J Chem* 2002, **42**(2-3)**:** 163-166.

127. Voityuk AA, Jortner J, Bixon M, Rösch N. Electronic coupling between Watson–Crick pairs for hole transfer and transport in desoxyribonucleic acid. *J Chem Phys* 2001, **114**(13)**:** 5614-5620.

128. Blatt FJ, Schroeder PA, Foiles CL, Greig D. *Thermoelectric Power of Metals*. *Plenum Press: New York* 1976, **ppxv:** 264.

129. Joshua H, Fang C, Peiming Z, Nongjian T. Thermal and electrochemical gate effects on DNA conductance. *Journal of Physics: Condensed Matter* 2007, **19**(21)**:** 215202.

130. Di Felice R, Calzolari A, Molinari E, Garbesi A. *Ab initio* study of model guanine assemblies: The role of pi-pi coupling and band transport. *Phys Rev B* 2001, **65**(4)**:** 045104.

131. Malen JA, Doak P, Baheti K, Tilley TD, Segalman RA, Majumdar A. Identifying the length dependence of orbital alignment and contact coupling in molecular heterojunctions. *Nano Lett* 2009, **9**(3)**:** 1164-1169.

132. Widawsky JR, Chen W, Vázquez H, Kim T, Breslow R, Hybertsen MS*, et al.* Length-dependent thermopower of highly conducting Au–C bonded single molecule junctions. *Nano Lett* 2013, **13**(6)**:** 2889-2894.

133. Mott NF, Davis EA. *Electronic Processes in Non-Crystalline Materials*. *Oxford: Clarendon Press* 1979.

134. Paulsson M, Datta S. Thermoelectric effect in molecular electronics. *Phys Rev B* 2003, **67**(24)**:** 241403.

135. Guo S, Zhou G, Tao N. Single molecule conductance, Thermopower, and Transition Voltage. *Nano Lett* 2013, **13**(9)**:** 4326-4332.

136. Kim Y, Jeong W, Kim K, Lee W, Reddy P. Electrostatic control of thermoelectricity in molecular junctions. *Nat Nano* 2014, **9**(11)**:** 881-885.

137. Bâldea I. Interpretation of Stochastic Events in Single-Molecule Measurements of Conductance and Transition Voltage Spectroscopy. *J Am Chem Soc* 2012, **134**(18)**:** 7958-7962.

138. Asai Y. Theory of Electric Conductance of DNA Molecule. *The Journal of Physical Chemistry B* 2003, **107**(19)**:** 4647-4652.

139. Wang Y, Zhou J, Yang R. Thermoelectric Properties of Molecular Nanowires. *The Journal of Physical Chemistry C* 2011, **115**(49)**:** 24418-24428.

140. Asai Y. Nonequilibrium phonon effects on transport properties through atomic and molecular bridge junctions. *Physical Review B* 2008, **78**(4)**:** 045434.

141. Asai Y. Vibronic spectroscopy using current noise. *Physical Review B* 2015, **91**(16)**:** 161402.

142. Apertet Y, Ouerdane H, Goupil C, Lecoeur P. Equivalent parameters for series thermoelectrics. *Energy Conversion and Management* 2015, **93:** 160-165.

143. Galperin M, Nitzan A, Ratner MA. Heat conduction in molecular transport junctions. *Physical Review B* 2007, **75**(15)**:** 155312.

144. Asai Y. Theory of local heating in single molecular bridge junctions. *Physical Review B* 2011, **84**(8)**:** 085436.

145. Yoshihiro A. Length and energy gap dependences of thermoelectricity in nanostructured junctions. *Journal of Physics: Condensed Matter* 2013, **25**(15)**:** 155305.

146. Lee SK, Yamada R, Tanaka S, Chang GS, Asai Y, Tada H. Universal Temperature Crossover Behavior of Electrical Conductance in a Single Oligothiophene Molecular Wire. *ACS Nano* 2012, **6**(6)**:** 5078-5082.

147. Senthilkumar K, Grozema FC, Guerra CF, Bickelhaupt FM, Lewis FD, Berlin YA*, et al.* Absolute Rates of Hole Transfer in DNA. *Journal of the American Chemical Society* 2005, **127**(42)**:** 14894-14903.

148. Kuznetsov AM, Ulstrup J. *Electron transfer in chemistry and biology. An introduction to the theory*. Wiley: Chichester, 1999.

149. Marcus RA. Chemical and Electrochemical Electron-Transfer Theory. *Annual Review of Physical Chemistry* 1964, **15**(1)**:** 155-196.

150. Marcus RA. On the Theory of Electron□Transfer Reactions. VI. Unified Treatment for Homogeneous and Electrode Reactions. *The Journal of Chemical Physics* 1965, **43**(2)**:** 679-701.

151. James SL, Adams CJ, Bolm C, Braga D, Collier P, Friscic T*, et al.* Mechanochemistry: opportunities for new and cleaner synthesis. *Chemical Society Reviews* 2012, **41**(1)**:** 413-447.

152. Stauch T, Dreuw A. Advances in Quantum Mechanochemistry: Electronic Structure Methods and Force Analysis. *Chemical Reviews* 2016, **116**(22)**:** 14137-14180.

153. Basedow AM, Ebert KH. Ultrasonic degradation of polymers in solution. *Physical Chemistry*. Springer Berlin Heidelberg: Berlin, Heidelberg, 1977, pp 83-148.

154. Hickenboth CR, Moore JS, White SR, Sottos NR, Baudry J, Wilson SR. Biasing reaction pathways with mechanical force. *Nature* 2007, **446**(7134)**:** 423-427.

155. Xiao X, Nagahara LA, Rawlett AM, Tao N. Electrochemical Gate-Controlled Conductance of Single Oligo(phenylene ethynylene)s. *Journal of the American Chemical Society* 2005, **127**(25)**:** 9235-9240.

156. Albers W, Milani R, Tappura K, Munter T, Resnati G, Metrangolo P. Self-Assembly of Pyridine-Modified Lipoic Acid Derivatives on Gold and Their Interaction with Thyroxine (T4). *International Journal of Molecular Sciences* 2013, **14**(2)**:** 3500.

157. Algar WR, Krull UJ. Luminescence and Stability of Aqueous Thioalkyl Acid Capped CdSe/ZnS Quantum Dots Correlated to Ligand Ionization. *ChemPhysChem* 2007, **8**(4)**:** 561-568.

158. Abad JM, Mertens SFL, Pita M, Fernández VM, Schiffrin DJ. Functionalization of Thioctic Acid-Capped Gold Nanoparticles for Specific Immobilization of Histidine-Tagged Proteins. *Journal of the American Chemical Society* 2005, **127**(15)**:** 5689-5694.

159. Mattoussi H, Mauro JM, Goldman ER, Anderson GP, Sundar VC, Mikulec FV*, et al.* Self-Assembly of CdSe−ZnS Quantum Dot Bioconjugates Using an Engineered Recombinant Protein. *Journal of the American Chemical Society* 2000, **122**(49)**:** 12142-12150.

160. Zanello P. *Inorganic Electrochemistry, Theory, Practice and Application*. The Royal Society of Chemistry: UK, 2003.

161. Eckermann AL, Feld DJ, Shaw JA, Meade TJ. Electrochemistry of redox-active self-assembled monolayers. *Coordination chemistry reviews* 2010, **254**(15-16)**:** 1769-1802.

162. Li, Hihath J, Chen F, Masuda T, Zang L, Tao. Thermally Activated Electron Transport in Single Redox Molecules. *Journal of the American Chemical Society* 2007, **129**(37)**:** 11535-11542.

163. Haiss W, Albrecht T, van Zalinge H, Higgins SJ, Bethell D, Höbenreich H*, et al.* Single-Molecule Conductance of Redox Molecules in Electrochemical Scanning Tunneling Microscopy. *The Journal of Physical Chemistry B* 2007, **111**(24)**:** 6703-6712.

164. Huang, Chen F, Bennett PA, Tao. Single Molecule Junctions Formed via Au−Thiol Contact: Stability and Breakdown Mechanism. *Journal of the American Chemical Society* 2007, **129**(43)**:** 13225-13231.

165. Diez-Perez I, Hihath J, Hines T, Wang Z-S, Zhou G, Mullen K*, et al.* Controlling single-molecule conductance through lateral coupling of [pi] orbitals. *Nat Nano* 2011, **6**(4)**:** 226-231.

166. Rubio G, Agraït N, Vieira S. Atomic-Sized Metallic Contacts: Mechanical Properties and Electronic Transport. *Physical Review Letters* 1996, **76**(13)**:** 2302-2305.

167. Dunitz JD, Orgel LE, Rich A. The crystal structure of ferrocene. *Acta Crystallographica* 1956, **9**(4)**:** 373-375.

168. Martinez R, Tiripicchio A. Structure of ferrocenium hexafluorophosphate. *Acta Crystallographica Section C* 1990, **46**(2)**:** 202-205.

169. Duggan DM, Hendrickson DN. Electronic structure of various ferricenium systems as inferred from Raman, infrared, low-temperature electronic absorption, and electron paramagnetic resonance measurements. *Inorganic Chemistry* 1975, **14**(5)**:** 955-970.

170. Browne WR, Feringa BL. Making molecular machines work. *Nat Nano* 2006, **1**(1)**:** 25-35.